

# Jagiellonian University

THE FACULTY OF PHYSICS, ASTRONOMY,  
AND APPLIED COMPUTER SCIENCE  
MARIAN SMOLUCHOWSKI INSTITUTE OF PHYSICS



Light and intermediate mass fragment  
emission from proton - nucleus collisions

Mariusz Wojciechowski

PhD dissertation  
performed in Nuclear Physics Department  
Thesis supervisor: Prof. dr hab. Bogusław Kamys

Cracow 2016



*Pracę dedykuję pamięci mojej Mamy.*

*Pragnę serdecznie podziękować Panu Profesorowi Bogusławowi Kamysowi  
za zaufanie, jakim mnie obdarzył zgadzając się zostać opiekunem mojej pracy,  
za przekazaną wiedzę, za otrzymaną pomoc, za troskę, wsparcie i wyrozumiałość.  
Gdyby nie Pana niezachwiany optymizm, wiara w sens dalszej pracy,  
niniejszy dokument nigdy by nie powstał.  
Dziękuję.*

*Dziękuję Panu Profesorowi Lucjanowi Jarczykowi  
za cenne rady, życzliwość. Za rozmowy pełne pomysłów,  
które miały znaczący wpływ na mnie i na moją pracę.*

*I wish to express my sincere thanks to Dr Frank Goldenbaum  
for his time and valuable comments from reading the manuscript.*

*Chciałbym podziękować mojej kochanej żonie Annie,  
za wiarę we mnie, za uczucie i zaufanie.  
Bez Ciebie nie było by tej pracy.*

*Dziękuję też moim synom, Jankowi i Pawłowi.  
Obiecuję, że teraz będę miał dla Was jeszcze więcej czasu.*



# Contents

<b>Chapter 1. Introduction</b> . . . . .	9
<b>Chapter 2. Review on the current status of knowledge on reaction mechanism in p-nucleus collisions at GeV energies</b> . . . . .	13
<b>Chapter 3. Description of the experiment</b> . . . . .	19
3.1. Characteristic of internal beam experiments . . . . .	19
3.2. The scattering chamber and the detecting system . . . . .	22
3.2.1. Cooled silicon telescopes . . . . .	23
3.2.2. The scintillator CsI detectors . . . . .	25
3.3. Normalization of the data . . . . .	28
<b>Chapter 4. The experimental results</b> . . . . .	31
4.1. The comparison of present data with those from the literature . . . . .	31
4.2. Light charged particles (LCP) . . . . .	33
4.3. Intermediate mass fragments – IMF . . . . .	39
<b>Chapter 5. The microscopic models of the reaction mechanism</b> . . . . .	43
5.1. The intranuclear cascade model - INCL . . . . .	43
5.2. The theoretical models of the second reaction stage . . . . .	46
5.2.1. Generalized Evaporation Model - GEM2 . . . . .	46
5.2.2. Statistical Multifragmentation Model - SMM . . . . .	47
5.3. The comparison of the theoretical calculations with the experimental data . . . . .	48
5.3.1. Angular dependence of light charged particle data . . . . .	48
5.3.2. Beam energy dependence of light charged particle data . . . . .	50
5.3.3. Angular dependence of intermediate mass fragments emission . . . . .	54
5.3.4. Beam energy dependence of intermediate mass fragment emission . . . . .	58
<b>Chapter 6. The phenomenological model</b> . . . . .	63
<b>Chapter 7. Comparison of present results with those for Ni and Au targets</b> . . . . .	75
7.1. Properties of the slow source . . . . .	75
7.2. Properties of the fast source . . . . .	77
7.2.1. Apparent temperature parameter $T$ . . . . .	77
7.2.2. Velocity parameter $\beta$ . . . . .	83
7.2.3. Absolute yield parameter $\sigma$ . . . . .	88
<b>Chapter 8. Summary and conclusions</b> . . . . .	93
<b>Appendix A. Two moving source model</b> . . . . .	97
<b>Appendix B. Determination of the mass <math>A_{source}</math> and the temperature <math>T_{source}</math> from the tangent to the T(A) function</b> . . . . .	101
<b>Appendix C. List of the papers on p+Ag reactions at GeV proton beam energies</b> . . . . .	103
<b>Appendix D. Description of format of attached experimental data</b> . . . . .	107

D.1. The structure of files and directories . . . . .	107
D.2. File format . . . . .	108
<b>Appendix E. Experimental data . . . . .</b>	<b>109</b>
<b>Bibliography . . . . .</b>	<b>117</b>

## Abstract

The double differential spectra  $d^2\sigma/d\Omega dE$  of protons, deuterons, tritons,  ${}^3,4\text{He}$ ,  ${}^{6,7,8,9}\text{Li}$ ,  ${}^{7,9,10}\text{Be}$ , and  ${}^{10,11,12}\text{B}$  were measured at 7 scattering angles: 15.6, 20, 35, 50, 65, 80 and 100 degree in the laboratory system for proton induced reactions on a silver target. Measurements were done for three proton energies: 1.2, 1.9, and 2.5 GeV. The experimental data were compared to calculations performed by means of two-step theoretical microscopic models. The first step of the reaction was described by the intranuclear cascade model INCL4.3 which allows for emission of nucleons and pions but also for emission of light charged particles (d, t,  ${}^3\text{He}$  and  ${}^4\text{He}$ ) created by coalescence of the nucleons escaping from the target nucleus. The second stage of the reaction was described by the Generalized Evaporation Model - GEM2 and by the Statistical Multifragmentation Model - SMM. Systematic deviations of the data from predictions of the models were observed. The deviations were especially large for the forward scattering angles and for the kinetic energy of emitted particles in the range from about 50 MeV to 150 MeV. It was found that adding a source moving along the beam direction and emitting isotropically the ejectiles significantly improves the description of the data. Moreover it was shown that the parameters of the source vary smoothly with the mass of the ejectiles and are almost independent of the proton beam energy. The presence of such a source with almost the same values of its parameters has been observed for p+Ni and p+Au collisions in the previous studies performed for the same beam energy range. This suggests that the same important mechanism is lacking in the present day microscopic models for all target nuclei in the studied beam energy range.

## Streszczenie

Podwójnie różniczkowe widma  $d^2\sigma/d\Omega dE$  protonów, deuteronów, trytonów,  ${}^3,4,6\text{He}$ ,  ${}^6,7,8,9\text{Li}$ ,  ${}^7,9,10\text{Be}$  i  ${}^{10,11,12}\text{B}$  zostały zmierzone pod 7 kątami: 15.6, 20, 35, 50, 65, 80 i 100 stopni w układzie laboratoryjnym dla reakcji wywołanych protonami na srebrnej tarczy. Pomiary wykonano dla trzech energii protonów: 1.2, 1.9 i 2.5 GeV. Dane doświadczalne porównano z obliczeniami wykonanymi przy pomocy dwustopniowych, mikroskopowych modeli teoretycznych. Pierwszy krok reakcji był opisywany przez model wewnątrzjądrowej kaskady INCL4.3, który pozwala na emisję nukleonów i pionów a także na emisję lekkich naładowanych cząstek (d, t,  ${}^3\text{He}$  i  ${}^4\text{He}$ ) tworzonych przez koalescencję nukleonów uciekających z jądra tarczy. Drugi etap reakcji był opisywany przez Uogólniony Model Wyparowania - GEM2 i przez Model Statystyczny Multifragmentacji - SMM. Zaobserwowano systematyczne odchylenia danych od przewidywań modeli. Odchylenia były szczególnie duże dla przednich kątów emisji i dla energii emitowanych cząstek w zakresie od ok. 50 MeV do 150 MeV. Stwierdzono, że dodanie źródła poruszającego się wzdłuż kierunku wiązki, emitującego izotropowo cząstki znacznie poprawia opis danych. Co więcej pokazano, że parametry źródła zmieniają się gładko wraz z masą emitowanych cząstek i są prawie niezależne od energii protonowej wiązki. Obecność takiego źródła z prawie identycznymi parametrami zaobserwowano dla zderzeń p+Ni i p+Au w poprzednich badaniach przeprowadzonych w tym samym zakresie energii wiązki. To sugeruje, że identyczny, ważny mechanizm jest pomijany w aktualnie istniejących modelach mikroskopowych dla wszystkich jąder tarczy w badanym zakresie energii wiązki protonów.

## Chapter 1

# Introduction

Reactions induced by protons of GeV energies impinging onto atomic nuclei are very important for many various purposes.

They are very abundant in the cosmic space due to the fact that energetic protons form the main content of the cosmic rays. Their interaction with the interstellar matter leads to change of the content of the interstellar matter and the cosmic rays themselves. The best known example of such an effect is strongly increased abundance (even 6 orders of magnitude) of lithium, beryllium and boron isotopes in cosmic rays in comparison to that in the Solar system, cf. fig. 1.1.

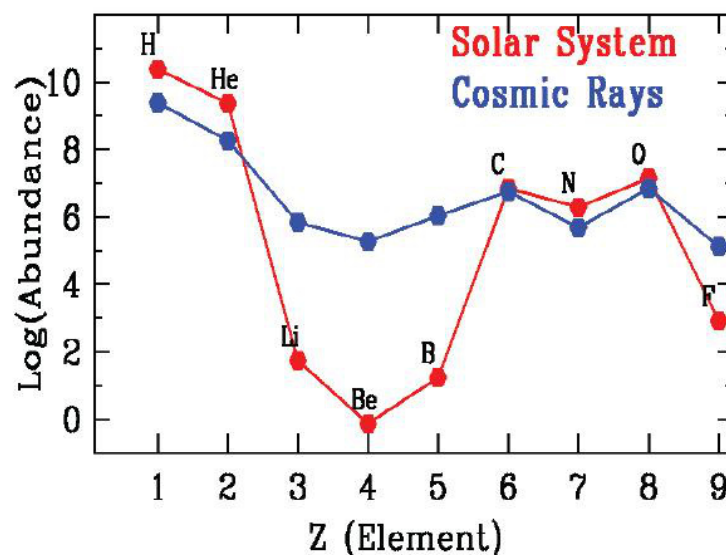


Figure 1.1. Abundance of elements in cosmic rays and in the Solar system. [1]

The interaction of energetic protons with atomic nuclei causes abundant emission of nucleons (both protons and neutrons). Such a process called by G.T. Seaborg „nuclear spallation” [2] may be used to produce an intense beam of neutrons. Typically up to 20 - 30 neutrons can be emitted from each collision of proton in GeV energy range with heavy metallic targets like mercury, tantalum or lead. The intense neutron pulses may be used for different purposes. For example the neutrons can be applied in subcritical fission reactors to produce energy in a safe and easy controlled way using as a fuel not only the uranium or plutonium but also the radioactive waste from standard fission reactors. Another application of intensive neutron beams is to build so called „spallation sources” of neutrons which can be used for various experiments of the solid state physics, biology, material science, etc. Usually the

neutrons are slowed down before being applied to the final studies. In such experiments the protons are interacting with thick targets in which their initial high energy is decreasing by interaction with many atomic nuclei present on their way through the target material. Therefore the knowledge of the cross sections for interaction of protons with different target nuclei at broad range of energies is demanded. The experiments devoted to determination of the necessary cross sections for all targets as well as in a broad range of energies are time consuming and have to be performed also for exotic, e.g. unstable nuclei. This may be difficult or impossible thus it calls for application of reliable theoretical models which would be able to interpolate and extrapolate the present knowledge of the reaction mechanism to other proton energies as well as for all atomic nuclei.

It is observed in many investigations that spectra of neutrons, light charged particles (LCP - i.e., isotopes of hydrogen and helium with  $A \leq 4$ ) as well as intermediate mass fragments (IMF - i.e. particles heavier than LCP but lighter than fission products) consist of two components: The low energy component which is almost isotropic, whereas the high energy one is strongly anisotropic - forward peaked [3, 4]. The present day models of the reaction mechanism assume that the proton impinging on to the target nucleus initiates an intranuclear cascade of the nucleon-nucleon collisions which are the source of fast nucleons and/or pions. The intranuclear cascade leaves the residual nucleus in an excited state what can lead to emission of nucleons but also heavier, complex particles - LCP and IMF. The arguments in a favor of such a picture is the fact that dimensions of the wave-packet representing the proton of GeV energies are smaller than the average distance between nucleons in the nucleus. The two-step model explains reasonably well spectra of nucleons as well as the low energy component of the spectra of complex particles but it was shown that the de-excitation of the target residuum is not able to reproduce the high energy component of the spectra of complex particles. To solve this problem it was proposed by Boudard et al. [5] that the high energy LCP are produced by the coalescence of the nucleons of the target with the nucleon escaping from the intranuclear cascade. Since this model (INCL4.3) quite well reproduced the emission of high energy LCP, its extension (INCL4.6) to IMF (fragments with mass not larger than  $A=8$ ) have been proposed by Boudard et al. [6]. Again the significant improvement of the description of the data has been achieved. It was, however, recently shown [7] that the model does not work well for  ${}^6,7,8\text{Li}$  and  ${}^7\text{Be}$  data measured for protons of energy 0.48 GeV impinging on to the silver target. The character of the spectra (high energy tail of the spectra) and that of the angular distribution (forward peaked distribution) agrees with the data, however, the slope of all the spectra is too small, thus the high energy data are strongly overestimated.

Due to the mentioned facts this coalescence model used in INCL4.6 is not adequate for IMF. It still needs improvements which allow for satisfactory description of existing data and furthermore enable one to achieve such a description for broader range of target masses and beam energies. To realize this a need appears to collect as much as possible of experimental information which should impose stringent constraints on all possible models of the reaction mechanism.

It was observed in our previous investigations [8] that a simple model of two moving sources emitting isotropically (in their c.m. system) is able to reproduce main properties of the experimental spectra and angular distributions of IMF in proton induced reactions on Ni and Au targets. Moreover, it was found that free

parameters of this model change smoothly from Ni to Au target and remain almost constant for a broad range of proton beam energies (from 1.2 to 2.5 GeV) [8]. A similar effect has been observed also for LCP, however then the additional contribution to the fast source has to be included explicitly from the intranuclear cascade stage of the reaction. In the case of complex LCP this contribution consisted in coalescence of nucleons escaping from the target nucleus whereas for protons the emission of protons from nucleon-nucleon collisions has to be taken into consideration. The phenomenological inclusion of the new source of fast LCP required then to scale down by factor  $\sim 0.7$  the original emission from INCL4.3 intranuclear cascade model.

The aim of the present investigation was to study proton induced reactions on a Ag target which has the mass number intermediate between Ni and Au target. It should allow for a check whether the same effects are observed for silver target as those found for light (i.e. Ni) and heavy (i.e. Au) targets with slowly varying properties of the moving sources.

The following topics are addressed in the present thesis:

- ◇ An overview of the current status of knowledge on the spallation reactions is given in chapter 2.
- ◇ Description of the experimental apparatus (the accelerator, scattering chamber and detection system), the raw data, their normalization are presented in chapter 3.
- ◇ Resulting angular and energy distributions are discussed in chapter 4, where they are also compared to the literature data.
- ◇ The theoretical models used in the analysis of the present experimental data are presented in chapter 5. Results of calculations performed by means of intranuclear cascade model combined with two models of the second stage of the reaction: evaporation and statistical multifragmentation are described in details in this chapter.
- ◇ The phenomenological analysis of the data performed in the frame of the model of two moving sources is presented in chapter 6.
- ◇ The parameters of the two moving sources obtained for silver target are compared with those previously published for Ni and Au targets. The result of this comparison is shown in chapter 7.
- ◇ The chapter 8 contains the summary and conclusions.



## Chapter 2

# Review on the current status of knowledge on reaction mechanism in p-nucleus collisions at GeV energies

Since the present thesis concerns the reactions involved by protons on the silver target the actual status of knowledge on the reaction mechanism induced by protons on that target is discussed in this section. Information on the reaction mechanism has been extracted from investigations of various observables. The list of performed experiments on the silver target may be found in the table C.1 in appendix C.

The most abundant experiments were devoted to determination of total production cross sections, kinetic energy spectra and angular distributions of emitted reaction products in inclusive measurements [4, 9–24]. These investigations led to formulation of several general conclusions concerning variation of the cross sections with the beam energy („excitation function”), and with the mass of the products („mass yield curve”).

One of the most important findings is *the leveling of* the excitation function of the production cross sections for all reaction products at proton beam energies larger than several GeV [25]. This was formulated in more general way as so called „limiting fragmentation hypothesis” (LFH) which claims that not only total cross sections but also differential cross sections approach limiting values at high energies [26, 27]. The measurements of differential cross sections are very rare for silver target. The results which are present in the literature cover the beam energy range lower than 1.2 GeV (e.g: ref. [12–14]) and higher than 5 GeV (e.g: ref. [4, 20, 24, 28]). The current state of the double differential cross sections measurements is shown in fig. 2.1. In this figure the proton beam energy dependence of the total production cross section of  ${}^7\text{Be}$  ejectiles in p+Ag collisions is presented. The full (blue) dots depict the total cross section values at energies at which the measurements of differential cross sections are reported in the literature. The open (red) squares show the  ${}^7\text{Be}$  cross sections at those energies at which the present measurements have been done.

The set of measurements of differential cross sections has been reported by N. T. Porile et al. [30] for the Xe nuclei which atomic mass is only  $\sim 20\%$  larger than that of silver. The authors performed investigation of the p+Xe reaction mechanism by measuring the spectra of intermediate mass fragments at  $48.5^\circ$  and  $131.5^\circ$  for proton beam energy from 1 to 19 GeV. It has been observed that the yield of intermediate mass fragments is energy independent for beam energies above  $\sim 9$  GeV what is in accord with the limiting fragmentation hypothesis. The measured spectra are well reproduced for such beam energies by the droplet model [31]. At smaller beam energies the yield of intermediate mass fragments increases with increasing energy. Furthermore, it was found that for these smaller energies another reaction mechanism must be involved for good reproduction of data (fig. 2.2). The understanding of this specific mechanism is a challenge for investigators.

The energy dependence of the  ${}^7\text{Be}$  total production cross sections shown in fig. 2.1 (solid line) confirms that similar effects as those observed by Porile et al. for

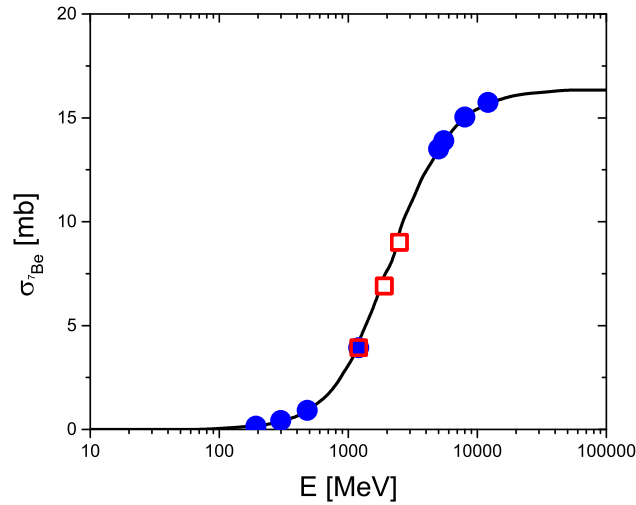


Figure 2.1. The black line presents the parametrization of the proton beam energy dependence of the total cross section on  ${}^7\text{Be}$  production in p+Ag reaction [29]. The blue points depict the total cross sections at energies at which the measurements of differential cross sections are reported in literature. The red squares correspond to the  ${}^7\text{Be}$  cross sections at those energies at which current experiment was performed.

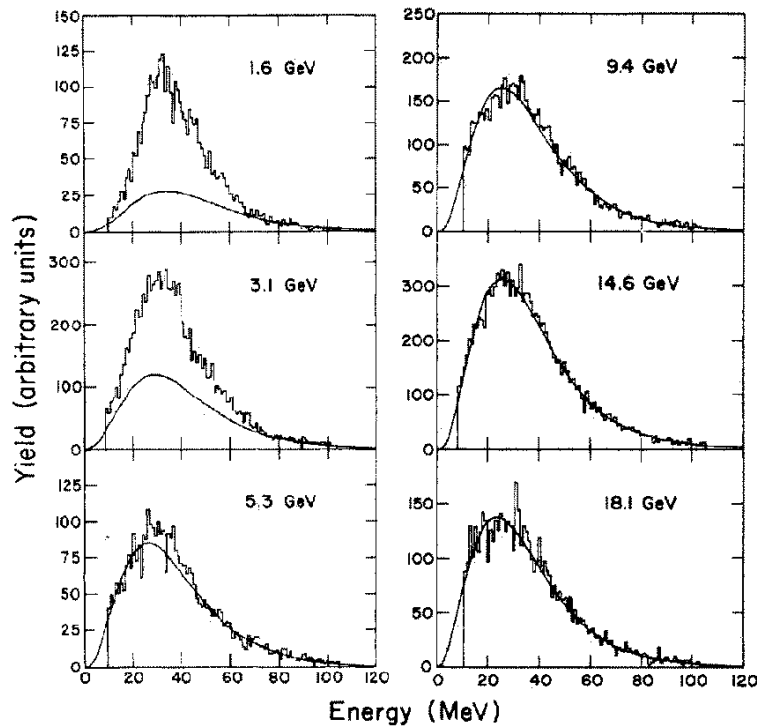


Figure 2.2. The histograms present the energy spectra of fragments with  $Z=6$  emitted at six proton beam energies (depicted on each panel separately) in p+Xe reaction. The curves are fits based on the droplet model. The figure is taken from Porile et al. [30]

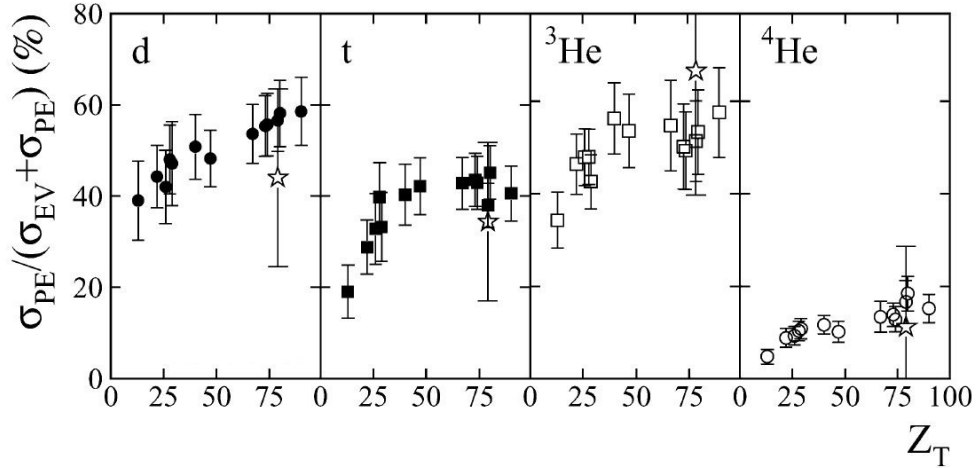


Figure 2.3. The target atomic number  $Z_T$  dependence of the contributions of pre-equilibrium emission relative to the total yield of light charged particles determined by Herbach et al. [32] in p+Ag collisions at proton beam energy 1.2 GeV.  $\sigma_{PE}$  represents yield of LCP for pre-equilibrium process,  $\sigma_{EV}$  - yield of LCP for evaporation emission. The figure is taken from ref. [32].

Xe nuclei are also present in the p+Ag nuclear system at the same region of proton beam energies. To prove this hypothesis more extended investigations are necessary which should involve measurements of not only the total but also of the differential cross sections for different ejectiles. Especially interesting are the data for light charged particles which usually are very abundant in such reactions and data for intermediate mass fragments. Such experiments were recently reported by Herbach et al. [32] for a broad range of atomic nuclei bombarded by protons of 1.2 GeV energy. The authors discuss the presence of two components in the experimental spectra. The first one can be reproduced by model assuming evaporation of particles from excited nucleus formed during collision of proton with the target nucleus. The second component is not described by the assumed mechanism and its qualitative behavior is interpreted by the authors as originating from some pre-equilibrium mechanism. In figure 2.3, taken from ref. [32], the relative contribution of this pre-equilibrium emission is shown. As can be seen this unknown mechanism is responsible for a large part of the total yield of the light charged particles. It is therefore worth performing more involved investigations of such a contribution. Since the measurements of Herbach et al. were done with rather poor statistics (especially for intermediate mass fragments) it is very desirable to produce data which enable one to study angular and energy dependence of differential cross sections with higher accuracy.

In the case of validity of limiting fragmentation hypothesis, the mass and charge dependence of the reaction products from proton - silver collisions should be „frozen” for proton energies larger than about 10 GeV. Total production cross section treated as a function of mass of ejectile, i.e. the *mass yield curve* is presented in fig. 2.4 for the silver target at proton beam energy of 300 GeV.

Mass yield curve has a „v-shape” which, according to authors of ref. [33], reflects the fact that different ejectiles originate from different reaction mechanisms. Heavy

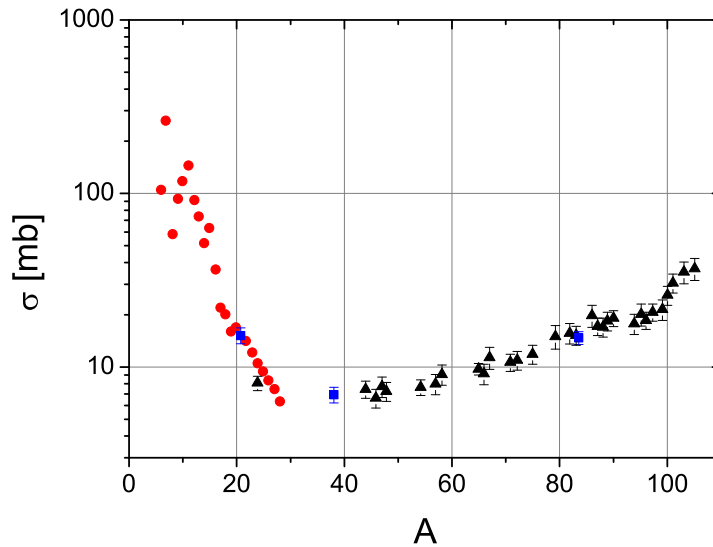


Figure 2.4. Mass-yield curve for interaction of 300 GeV protons with silver (taken from Ref. [33]). Black triangles show cross sections from radiochemical measurements [27, 34], blue squares represent results of mass spectrometric experiment [35], and red circles depict cross sections extracted from interpolation of results obtained in measurements on Kr and Xe targets [36].

products correspond to spallation residua of the target whereas intermediate mass fragments can accompany these residua or can appear as the result of multifragmentation.

Similar shapes of mass yield curves were observed also at lower proton energies. In fig. 2.5 a comparison of mass yield curves obtained at different proton energies (from 1 GeV to 300 GeV) are shown. In wide range of reaction product masses ( $30 \lesssim A \lesssim 90$ ) cross sections measured at proton beam energies from 11.5 GeV to 300 GeV are almost not distinguishable (lines), what may be used as a proof of validity of limiting fragmentation hypothesis. Significant differences between cross sections measured at 1, 3, and 4.9 GeV (points) and those at higher energies of proton beam indicate that the limiting fragmentation hypothesis does not work at energies lower than  $\sim 10$  GeV. It is, however, not clear whether the analog behavior appears for other reaction products, i.e. light charged particles and intermediate mass fragments ( $A \lesssim 30$ ) since these experimental data were measured only for lowest energies.

It is worthy to point out that the mass yield curve for  $A \lesssim 30$  can be well described by a smooth function of  $A$ , i.e., the mass dependence is characterized by a „power-law” behavior of the production cross sections:

$$\sigma(A) \propto A^{-\tau}. \quad (2.1)$$

Similar „power-law” dependence appears when the cross sections are treated as function of  $Z$ . This was discussed for silver target in the paper of S. J. Yennello et al. [17] where authors shown that the parameter  $\tau$  varies with the proton beam energy (see

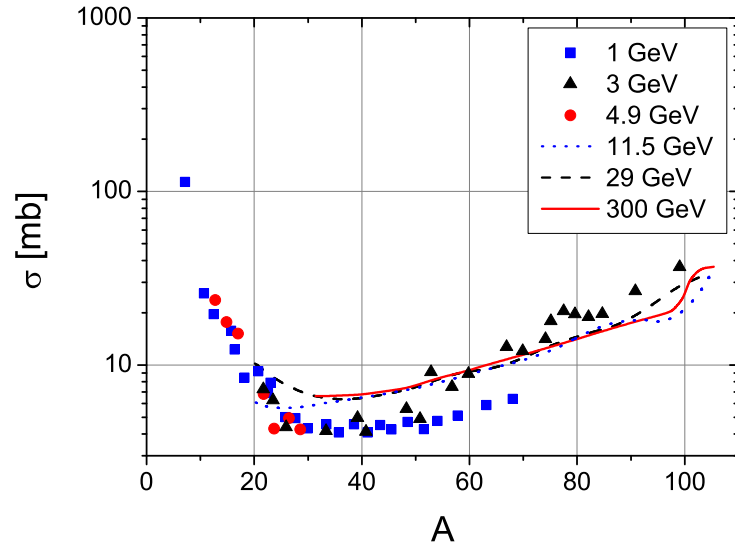


Figure 2.5. Comparison of the mass-yield curves measured in reaction  $p+\text{Ag}$  at different proton beam energies: at 1 GeV (blue squares) by L. N. Andronenko et al. [37], at 4.9 GeV (red circles) by G. D. Westfall et al. [38], at 3 GeV (black triangles) and 29 GeV (black dashed line) both obtained by Katcoff et al. [39], at 11.5 GeV (blue dotted line) obtained by G. English et al. [40], and at 300 GeV (red solid line) measured by N. T. Porile et al. [27] and G. English et al. [34].

fig.2.6). Since no data obtained with silver target were available at beam energies higher than 1 GeV, the authors showed for these energies  $\tau$  values extracted from experiments with xenon target. They accepted explanation of the origin of the energy dependence of  $\tau$  parameter given by R. E. L. Green et al. [11, 13], who interpreted variation of the parameter  $\tau$  with energy of projectile as a change in reaction mechanism from emission dominated by equilibrium processes at lower energies to one dominated by non-equilibrium processes at higher energies. Another interpretation was quoted by A.D. Panagiotou et al. [41], who argued on the basis of Fisher's droplet model that the energy dependence of the  $\tau$  parameter should have a non monotonic behavior with a minimum at the energy at which nuclear liquid-gas phase transition appears.

One can see from inspection of fig. 2.6 that the  $\tau$  reaches a minimal value at a proton energy around 3-5 GeV. It should be, however, emphasized that the data at these energies were obtained not with the silver but with the xenon target. Extrapolation of the  $\tau$  energy dependence determined by silver target data to higher energies may not agree with the xenon data. Therefore the final decision concerning the shape of  $\tau$  energy dependence, and especially position of its minimum, calls for new measurements for silver target at proton energies higher than 1 GeV.

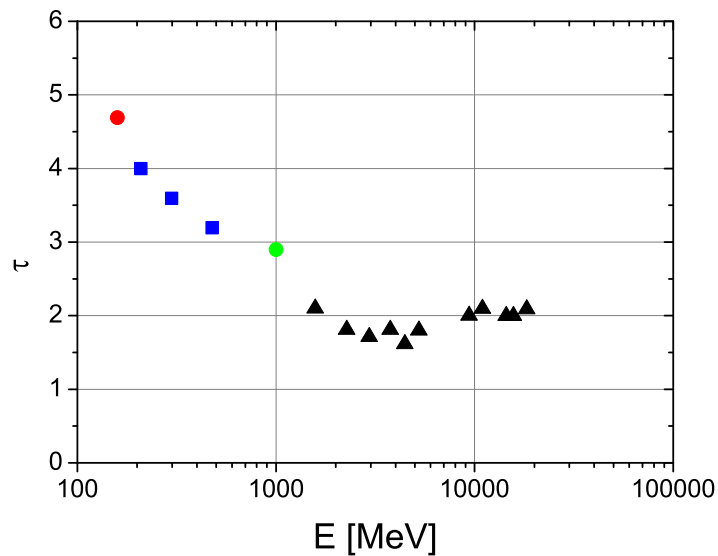


Figure 2.6. „Power-law” parameter  $\tau$  as a function of proton beam energy. Red circle [17], blue squares [11, 13], and green circle [42] coming from measurements on silver target, and black triangles [43] from p+Xe reaction.

### Summary

This short review of the status of knowledge on the reaction mechanism induced by protons at various beam energies and targets, reveal the areas where further investigation should be performed. The following conclusions can be expressed.

- ◇ Both, total and differential cross sections rapidly change in the 1-10 GeV beam energy range. This conclusions is based mainly on the results of measurement for targets different than silver, especially [30], partially confirmed for Ag by the Herbach et al. [32] for 1.2 GeV proton beam energy.
- ◇ There is a lack of measurements of double differential cross sections  $\frac{d^2\sigma}{dE d\Omega}$  for silver target in the most interesting proton beam energy region 1-10 GeV.
- ◇ It was shown by Porile et al. [30] that two different mechanism contribute to the cross sections at this energy region. The proposed up to now theoretical description of the observed spectra is not satisfactorily.

Taking into consideration all these facts, it is clear that new data for proton beam energy from 1 to 10 GeV are desirable. Measurements of LCP and IMF differential cross sections preformed by C. M. Herbach et al. [32] at proton energy 1.2 GeV for silver target suggested that this energy to be a natural choice which enable comparison currently measured data with already published. Performing measurements for two higher energies (1.9, 2.5 GeV) would allow to observe changes in the reaction mechanism which are expected in the 1-10 GeV beam energy range. It would give severe constraints for all theoretical models of the reaction mechanism.

## Chapter 3

# Description of the experiment

The goal of the present study was to investigate experimentally the interaction of protons with Ag nuclei in the proton beam energy range from 1.2 GeV to 2.5 GeV. Double differential cross sections  $\frac{d^2\sigma}{dEd\Omega}$  for production of light charged particles (LCP) and intermediate mass fragments (IMF) have been measured at 15.6°, 20°, 35°, 50°, 65°, 80°, and 100° in laboratory system for proton beam energies 1.2, 1.9 and 2.5 GeV.

### 3.1. Characteristic of internal beam experiments

The **Proton-Induced SpAllation** (PISA) experiment was performed using the internal beam of COSY - **CO**oled **SY**nchrotron and storage ring of 184 m circumference which is operated in the Research Centre Jülich. The COSY facility allows to accelerate protons and deuterons to the wide range of momenta from 0.3 GeV/c to 3.65 GeV/c [44]. Several target stations, both internal and external, allow to conduct measurements. The luminosity of COSY is roughly  $10^{31} \text{ cm}^{-2}\text{s}^{-1}$  [45] on an internal target. Typical approach to prepare the final beam consists of the following steps:

- ◇ injection of particles initially accelerated by JULIC cyclotron, into the COSY ring
- ◇ their acceleration to the final momentum, and
- ◇ accumulation of particles in the ring.

After this sequence the beam can be cooled down using electron or stochastic cooling if necessary. The whole process takes several seconds as it was observed during PISA measurements.

When the beam reaches expected properties it is directed to the internal or external target stations. In case of experiments on an internal target, the prepared beam is circulating in the COSY ring below (like in the case of PISA experiment) or above the target, and finally it is shifted towards the target. The target can be irradiated gradually, and the speed of the vertical beam moving can be adjusted to fit the efficiency of the data acquisition system. Schematic plan of the COSY facility is shown in fig. 3.1, together with target stations of PISA and other experiments.

The internal beam experiment has several very appealing advantages:

- ◇ Due to multiple passing of the beam through the target it is possible to obtain relatively high statistics of the data using a thin target. Such small thickness assured that the re-scattering and absorption of the reaction products in the target is negligible small.
- ◇ The second advantage is a possibility to control the speed of data registration by detectors, so one could fully use the performance of the data acquisition (DAQ) system. This was achieved in the present study by controlling the pace of shifting

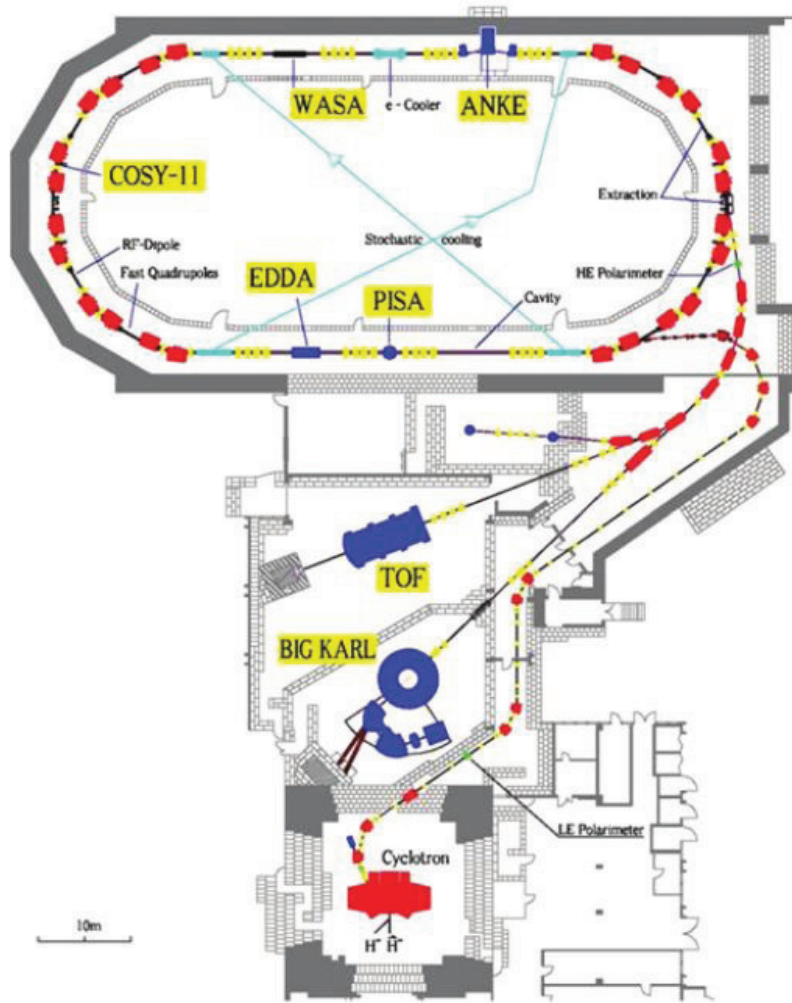


Figure 3.1. The COSY facility with internal and external experiments. [44]

the beam towards the target. The computer controlled beam used the signal from one of the detectors to establish a negative feedback, see fig. 3.2.

- ◇ The most important profit in the case of PISA experiment was assuring the same experimental conditions for each beam energy used during the measurements. As it was described to above the COSY facility works in cycles consisted of the sequential operations: injection of particles, their accumulation, acceleration, and finally the controlled beam consuming. It allowed us to change the energy of the beam from cycle to cycle without modifying other experimental conditions. Such a procedure assures that the experiment was performed in the same conditions for all three energies: 1.2, 1.9, and 2.5 GeV. Furthermore, it was also possible to collect similar statistics of events for each energy by carrying out the measurements in so called super-cycle mode. In this mode several cycles were alternated for each requested beam energy. Adjusting number of cycles and their length enabled us to achieve almost the same statistics for all beam energies. It is illustrated by fig. 3.2 where the green line represents the intensity of the COSY beam and the red line shows the counting rate of the detector which was used to establish the negative feedback for computer controlling the speed of vertical

movement of the beam towards the target. Three cycles at energy 1.2 (three narrow peaks in the figure) followed by one cycle at 1.9 GeV and one cycle at 2.5 GeV gives roughly the same statistics (area under the red line) for all energies.

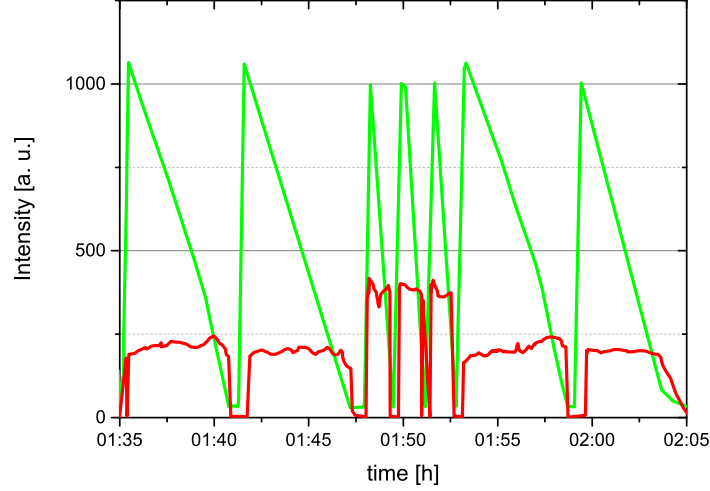


Figure 3.2. Green line presents the intensity of the COSY beam whereas the red line depicts the counting rate of the detector used to establish the negative feedback.

Both signals are presented in arbitrary units in the real-time scale.

The internal beam experiment involves, however, a series of problems. First of all, the scattering chamber is then a part of the synchrotron, what means that it has to assure the same vacuum (of order of  $10^{-8} \text{ mbar}$ ) as that in the COSY ring. To achieve this the chamber itself and part of the detecting system placed in the chamber have to be built from very high quality materials. Mounting of the detectors in the chamber has to be done with closed valves separating the chamber from the COSY ring and must be followed by intensive pumping which may take quite a long time.

The second issue is caused by the limited access to the experimental equipment when other experiments are performed. Thus the detectors, target system, and some parts of the data acquisition system must be carefully prepared and tested in conditions which are not exactly the same as those in the COSY ring. Every change has to be planned and performed quickly during synchrotron maintenance periods. It means that some devices have to be mounted several weeks before the internal beam experiment, without an opportunity to change later anything up to the experiment. Any further modifications of the apparatus (during the experiment) should be avoided especially if they involve opening of the scattering chamber.

Besides technical problems mentioned above, also the pure physical issues are raised in front of the scientist. For example, the absolute data normalization cannot be performed in internal beam experiments according to the standard method used in external beam measurements, i.e. by determination of the current of particles impinging on the target and of the target thickness. It has to be rather done by measuring the cross sections of monitor reactions together with those of the studied processes.

### 3.2. The scattering chamber and the detecting system

To put possibly strong constraints to all theoretical models of the reaction mechanism the experimental data should be as exclusive as possible. Therefore in the present experiment the charge and mass identification of the reaction products was undertaken. For this purpose the telescopes built of several silicon detectors followed for some of them by the CsI scintillator detectors have been used. The telescopes were positioned at the following angles in respect to the beam direction: 15.6°, 20°, 35°, 50°, 65°, 80°, and 100°.

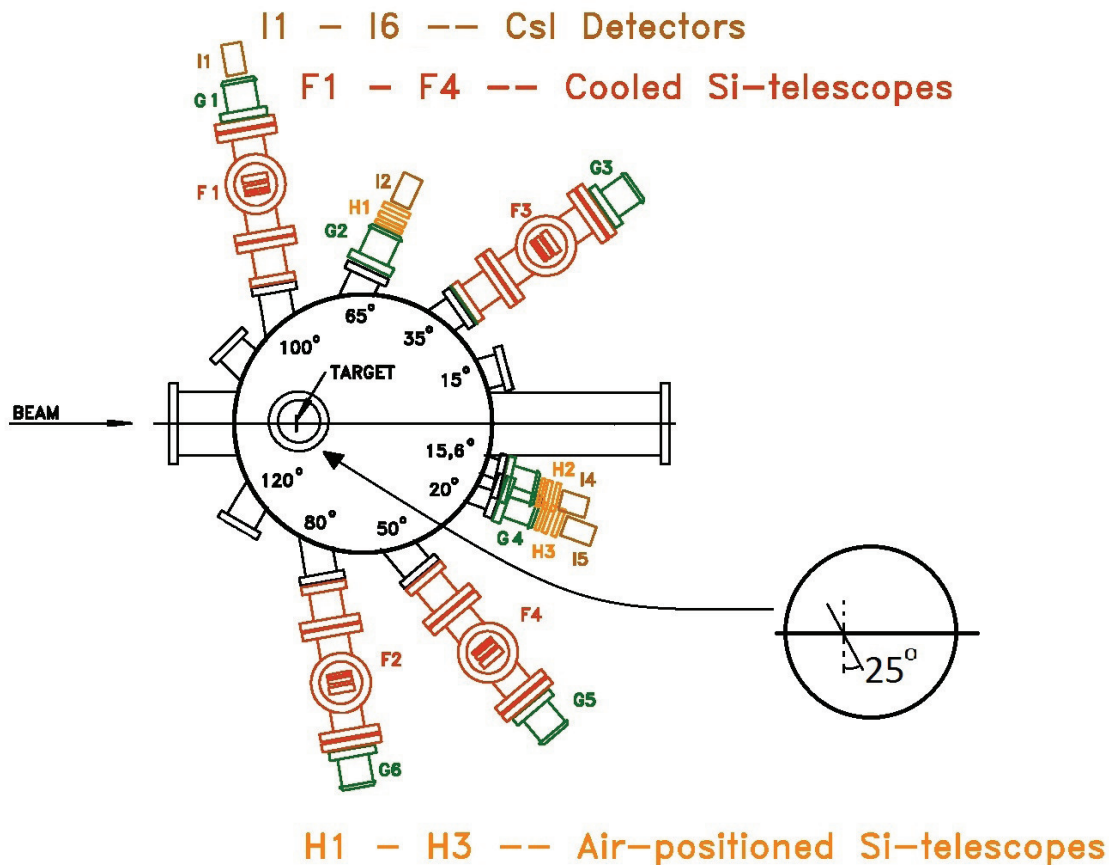


Figure 3.3. The setup of PISA's detectors. Detection arms mounted on scattering chamber which was positioned directly in the ring of COSY. As it is shown, the target has been rotated by 65° in respect to the beam direction.

The crucial part of the experimental setup of PISA was the scattering chamber shown schematically in fig. 3.3.

The chamber have several ports tipped with the flanges which were used for mounting the detection arms at the following angles: 15.6°, 20°, 35°, 50°, 65°, 80°, and 100°. Three types of detecting arms were used:

- ◇ cooled silicon telescopes F3, F4, and F2 at 35°, 50°, and 80°, respectively,
- ◇ air-positioned silicon telescopes H2, H3, and H1 backed by CsI scintillator detectors I4, I5, and I2 at 15.6°, 20°, 65°, respectively,
- ◇ cooled silicon telescope F1 followed by scintillator detector I1 at 100°.

The vacuum part of each detector arm was closed from outside by the 50  $\mu\text{m}$  stainless steel foil (G1 - G7). The silicon detectors of the telescope at  $100^\circ$  were placed inside the vacuum chamber, whereas the scintillator detector was installed in air outside the stainless steel foil G1.

A silver target of  $580 \mu\text{g}/\text{cm}^2$  thickness has been used. It was turned by  $65^\circ$  in respect to the beam direction to assure approximately the same effective thickness for products of the reactions flying in direction of all detectors.

### 3.2.1. Cooled silicon telescopes

The semiconductor telescopes positioned at  $35^\circ$ ,  $50^\circ$ , and  $80^\circ$  were cooled-down to  $-10^\circ\text{C}$  to obtain good energy resolution. Due to this the distinct and unambiguous (A,Z) identification of products with Z up to 5 was achieved. The energy resolution of data for elements with  $5 < Z \leq 8$  was poorer because of smaller statistics of the data, thus only elemental identification has been done. In table 3.1 the energy detection thresholds and the energy detection ranges are presented for each detection arm with cooled-down silicon detectors, including that at  $100^\circ$ . The last silicon telescope was backed by the stainless steel foil followed by the CsI scintillator detector placed in air. The use of scintillating detector expanded the detection range of hydrogen isotopes to higher energies.

Table 3.1. Energy thresholds and ranges (in MeV) of reaction products detected at various scattering angles for cooled-down silicon telescopes. For telescope at  $100^\circ$  the range is larger because of presence of the CsI scintillator detector.

Ejectile	Angle [degrees]			
	35	50	80	100
p	3.5-21.5	3.5-23.5	3.5-6.5	9.5-163.5
d	4.5-36.5	4.5-31	4.5-9.5	13.5-218.5
t	4.5-39.5	4.5-34	4.5-10	14.5-159.5
$^3\text{He}$	8.5-97.5	8.5-95	13.5-21.5	9.5-173
$^4\text{He}$	9.5-120.5	8.5-119.5	14.5-25.5	10.5-133.5
$^6\text{He}$	10.5-115.5	10.5-121.5	15.5-27	11.5-82.5
$^6\text{Li}$	17.5-179.5	15.5-174.5	18.5-50.5	18.5-114
$^7\text{Li}$	17.5-158.5	16.5-159.5	20.5-55.5	19.5-106
$^8\text{Li}$	18.5-108.5	17.5-104	21.5-54	19.5-82
$^9\text{Li}$	20.5-62	17.5-53.5	22.5-51.5	21.5-50.5
$^7\text{Be}$	25.5-127.5	21.5-138.5	27.5-71.5	25.5-109.5
$^9\text{Be}$	26.5-95	24.5-90.5	29.5-80.5	27.5-75.5
$^{10}\text{Be}$	27.5-93.5	25.5-82.5	20.5-81.5	29.5-80
$^{10}\text{B}$	35.5-104	30.5-99	38.5-98.5	36.5-80.5
$^{11}\text{B}$	35.5-119.5	30.5-99.5	39.5-95.5	37.5-91
$^{12}\text{B}$	36.5-78.5	34.5-70.5	42.5-69	39.5-66
C	45.5-116.5	40.5-106	47.5-92	11.5-61.5
N	55.5-97	49.5-88	59.5-85.5	13.5-73.5
O	68.5-92.5	59.5-89.5	68.5-82.5	16.5-73

Semiconductor telescopes have to contain two or more detectors. The first of the detectors should be as thin as possible assuring the good quality signal. It gives

information on the differential  $dE/dx$  energy loss, whereas other, thicker detectors in the telescope collect the charge which is proportional to the full energy  $E$  of the charged product. This two quantities are coupled by the following relationship which contains the atomic  $Z$  and mass  $A$  numbers of the detected particle:

$$\frac{dE}{dx}(E) \sim \frac{AZ^2}{E} \quad (3.1)$$

and therefore may be used for  $(A,Z)$  identification of particles.

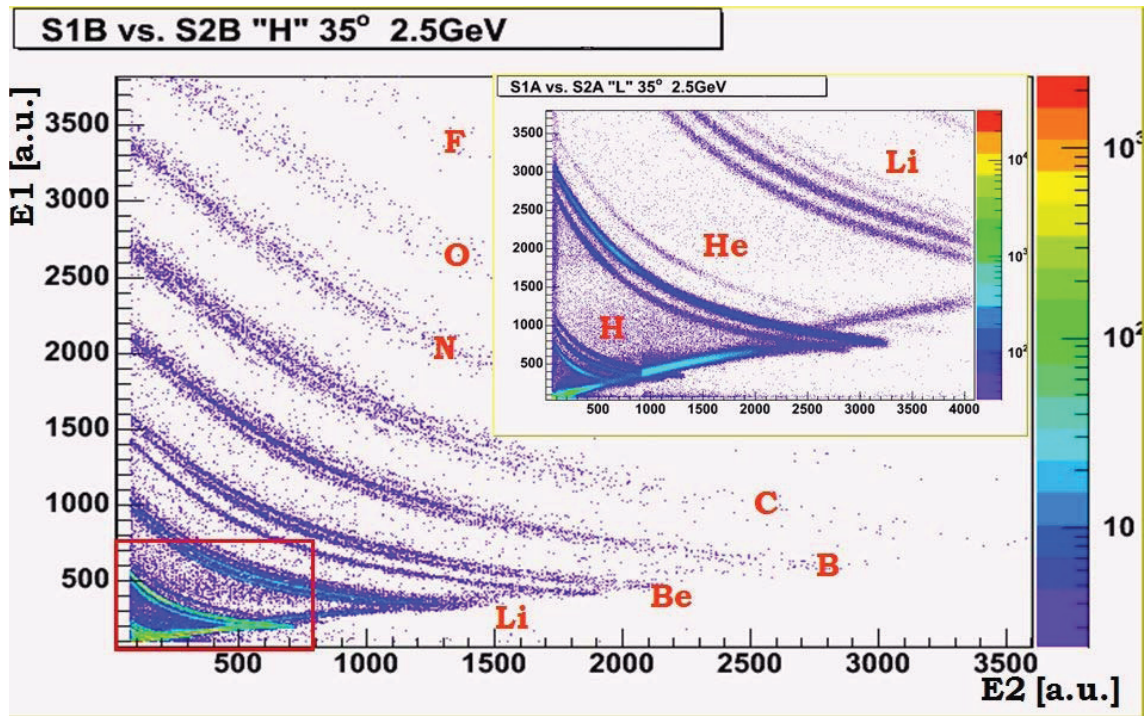


Figure 3.4. The example of collected on-line histograms  $\Delta E - E$  during PISA experiment. Both axes represent the energy loss in Si detectors in arbitrary units.

The typical  $\Delta E - E$  histogram built of signals from the first and the second detector in the silicon telescope, collected during experiment is presented in figure 3.4. As can be seen the points are assembled along the lines corresponding to different  $(A,Z)$  according to formula 3.1. The background is on the acceptable level and does not influence the identification of particles.

The setup of PISA data acquisition system supports two levels of amplification for signals from silicon detectors. Thanks to this two histograms were registered simultaneously during measurements. The first one which covers  $Z \leq 8$ , and the second one which contains signals only for the reaction products  $Z \leq 2$ , see the upper right corner of the fig. 3.4. Such a method enables us to register as many as possible different particles and simultaneously to increase resolution for hydrogen and helium isotopes.

To obtain differential cross sections  $\frac{d^2\sigma}{dEd\Omega}$  from such histograms it is necessary to perform energy calibration which must be done separately for each silicon detector because it depends on the thickness of the detector and the signal amplification. The energy calibration was made by fitting two-dimensional spectra (like fig. 3.4) for all pairs of the silicon detectors.

The thickness of silicon detectors is presented in table 3.2 together with that of the stainless steel foils and CsI scintillators.

Table 3.2. Thicknesses of the detectors in the  $\Delta E - E$  silicon telescopes. Thicknesses of the separating stainless steel foil and CsI scintillator detector are presented as well. [46]

Angle degree	Foil $\mu m$	Silicon detectors				Foil $\mu m$	CsI cm
		$\mu m$					
15.6°	50	89	1016	1016	89	-	7
20°	50	89	1016	1016	89	-	7
35°	-	48	426	6000		-	-
50°	-	41	398	6000		-	-
65°	50	84	1016	1016	89	-	7
80°	-	56	420			-	-
100°	-	52	401	1000	2012	50	7

### 3.2.2. The scintillator CsI detectors

The silicon telescopes were backed for four angles; 15.6°, 20°, 65°, and 100° by a 7 cm thick cesium iodide detector activated with thallium: CsI(Tl) with a photo-diode readout, which were used to detect high-energy light charged particles (LCPs) passing through the silicon detectors. The scintillating detector at 100° was separated from silicon telescope by 50  $\mu m$  stainless steel foil. The telescopes which contained scintillator detectors worked according to the same rules like discussed above fully semiconductor telescopes:  $\Delta E - E$ . The last silicon detector at those angles where scintillator detectors were used was transparent what allowed to register ejectiles without re-scattering effect and without an extra gap in the energy spectra. The thickness and the kind of material of the mentioned foil were taken into consideration during the energy calibration.

Since the density (4.5  $g/cm^3$ ) of the CsI scintillator is larger than the silicon density it has a higher stopping power. Additionally the scintillator detectors used in PISA experiment were much thicker than the silicon detectors what enabled us to measure larger energy range of the spectra than with pure semiconductor telescopes. The example of the  $\Delta E - E$  identification spectra obtained by a pair consisted of the silicon detector and the CsI detector is shown in fig. 3.5.

The energy calibration of the signals from the scintillator detectors where the light output is a nonlinear function of the energy was made in the following way: The light output was parametrized with eq. 3.2 as in ref. [47] :

$$L(E, A, Z) = a_0 + a_1(E - a_3AZ^2 \ln(\frac{E}{a_2AZ^2} + 1)) \quad (3.2)$$

The parameter  $a_0$  and  $a_1$  were fixed at values specific for the individual detectors, since they were determined by the electronic setup. The parameters  $a_2$  and  $a_3$ , which contain information on quenching of the light signal in CsI, were common for all scintillating detectors. Similarly like for silicon detector parameters were fitted to the two dimensional  $\Delta E - E$  spectra where the information about  $\Delta E$  was taken

Table 3.3. Thresholds and ranges of the energy (in MeV) of isotopically and elementally identified reaction products detected at various scattering angles for air-positioned silicon detectors backed by CsI scintillator detectors.

Ejectile	Angle [degrees]		
	15.6	20	65
p	7.5-162	7.5-162.5	7.5-161.5
d	9.5-208.5	9.5-212.5	8.5-213
t	10.5-239.5	10.5-244.5	9.5-246.5
$^3\text{He}$	21.5-297.5	21.5-297.5	21.5-297.5
$^4\text{He}$	23.5-296.5	23.5-298.5	24.5-257.5
$^6\text{He}$	26.5-85.5	26.5-89.5	26.5-86.5
$^6\text{Li}$	42.5-147	42.5-149.5	42.5-147
$^7\text{Li}$	45.5-156	45.5-156.5	44.5-152.5
$^8\text{Li}$	47.5-125.5	47.5-127.5	46.5-118.5
$^9\text{Li}$	49.5-103	50.5-109.5	49.5-78.5
$^7\text{Be}$	62.5-160.5	62.5-167.5	61.5-148
$^9\text{Be}$	68.5-113.5	69.5-126.5	68.5-113
$^{10}\text{Be}$	71.5-130.5	71.5-122	71.5-107.5
$^{10}\text{B}$	90.5-117.5	92.5-125.5	91.5-124.5
$^{11}\text{B}$	94.5-127.5	95.5-134.5	93.5-114
C	10.5-108.5	85.5-100	50.5-101.5
N	12.5-74.5		62.5-95.5
O	14.5-89		74.5-86.5

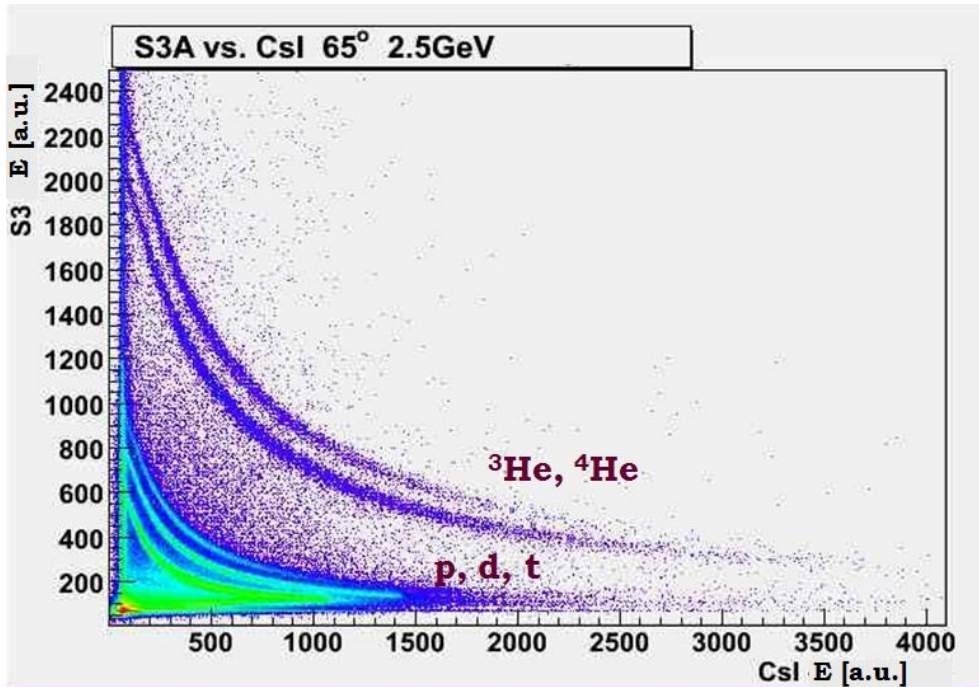


Figure 3.5. The example of the  $\Delta E - E$  histogram collected on-line by Si-CsI telescope mounted at the angle of  $65^\circ$ . Both axes represent the energy loss in arbitrary units.

from the silicon detector placed in front of the scintillator detector. The losses of the particle energies in the stainless steel foil and in the air were taken into account. The best results of fits were obtained for values of parameters shown in table 3.4.

Table 3.4. Values of parameters common for all scintillators [48].

	p	d	t	He
$a_2$ [MeV]	75			
$a_3$ [MeV]	157.5	150	135	

Figure 3.6 illustrates the increase of the detected energy range due to application of CsI detector in the telescope.

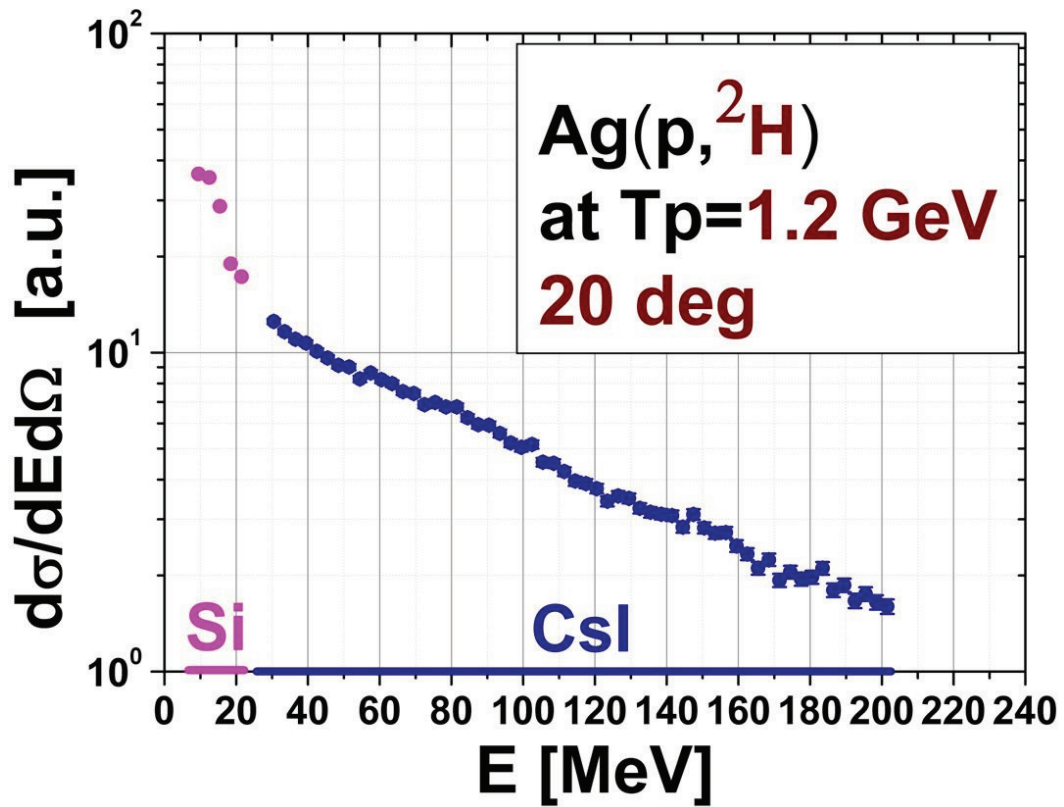


Figure 3.6. Example of collected on-line histograms  $\frac{d\sigma}{dEd\Omega}$  (in arbitrary units) with marking the area from both main parts of Si-CsI pair.

### 3.3. Normalization of the data

As it was mentioned above the internal beam experiment data must be normalized in a specific manner. In order to obtain absolute normalization of double differential cross sections  $\frac{d^2\sigma}{dE d\Omega}$  for production of light charged particles and intermediate mass fragments the cross sections of a monitor reaction should be determined together with the data of interest.

In the case of PISA experiment the absolute normalization of the cross sections was obtained from comparison of the value of the total production cross section of  ${}^7\text{Be}$ , extracted from measured double differential cross sections with known in the literature values.

Since the total production cross section of  ${}^7\text{Be}$  was very frequently measured in proton induced reactions it was possible to perform a realistic parameterization (A. Bubak, et al. [29]) of this total cross section as a function of target mass and proton beam energy for all targets from  ${}^{12}\text{C}$  to U and for very broad range of proton energies, i.e., from the reaction threshold up to  $\sim 20$  GeV. Proton energies used in PISA experiment (1.2 GeV, 1.9 GeV, 2.5 GeV) belong to the energy range of validity of the above parameterization as illustrated by fig. 3.7.

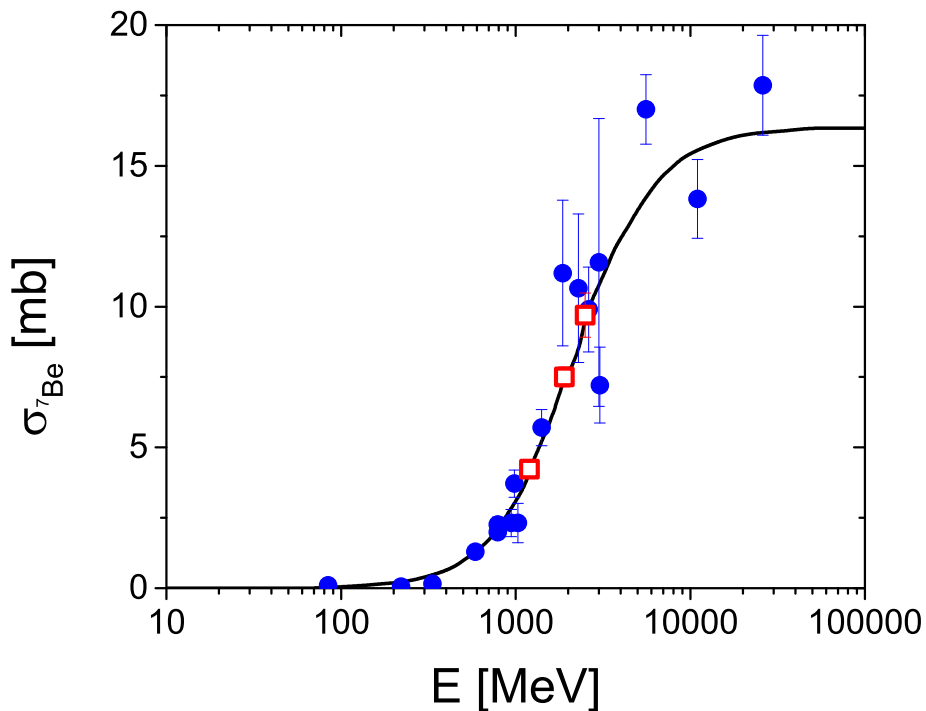


Figure 3.7. The black line presents the parametrization of the proton beam energy dependence of the total cross section on  ${}^7\text{Be}$  production in p+Ag reaction [29]. The blue circles present experimental  ${}^7\text{Be}$  total cross section taken from [29] while the red squares indicate PISA's  ${}^7\text{Be}$  total cross section values for proton energy 1.2, 1.9 and 2.5 GeV.

The total  ${}^7\text{Be}$  production cross section was not measured in straightforward way in the PISA project but it could be extracted from double differential cross sections  $\frac{d^2\sigma}{dE d\Omega}$ . In order to get total cross section one has to integrate spectra over full range

of angles and kinetic energies of the ejectile. It was realized by the following method: The differential cross sections of  ${}^7\text{Be}$  used in the integration were measured only for limited angular range (from  $15.6^\circ$  to  $100^\circ$  in the laboratory system) and for energies larger than  $\sim 25$  MeV (because of the energy threshold of detection of the telescopes built of silicon detectors). The experimental cross sections were parameterized by means of two moving source model (described in detail in Appendix A) to allow for interpolation and extrapolation of the data to angular and energy regions not measured in the experiment, what was necessary to perform the angular and energy integration.

Examples of the fits with two moving source model to  ${}^7\text{Be}$  data for  $50^\circ$  at three different proton beam energy 1.2, 1.9 and 2.5 GeV are presented in fig. 3.8.

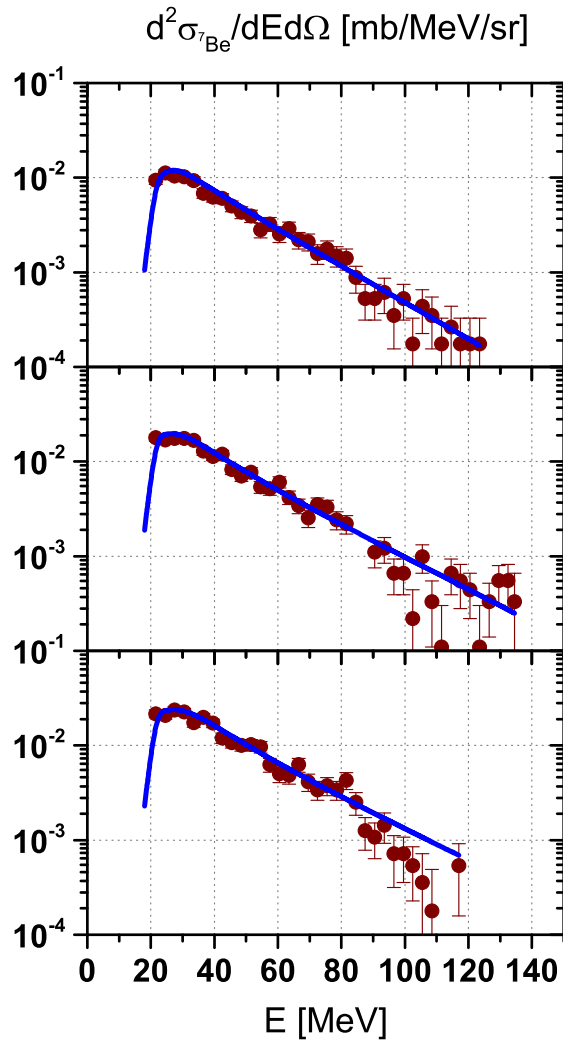


Figure 3.8. Points - PISA data (p+Ag,  $50^\circ$ ) for  ${}^7\text{Be}$ , blue line represents the fits of the phenomenological two moving source model. The upper panel presents data for proton beam energy 1.2 GeV, while 1.9 GeV is in the middle and 2.5 GeV in the bottom panel.

The angular dependence of the experimental cross sections was very smooth thus the extrapolation should not introduce any significant inaccuracy of the total cross section. However, extrapolation of the spectrum to low energy region may involve larger inaccuracy because variation of the cross section is there quite large. To decrease possible error of the extrapolation the following constraints were taken into account: One can expect that the cross section is very close to zero at very small energies (because of the Coulomb repulsion of  ${}^7\text{Be}$  fragment and the emitting source). It increases with energy reaching a maximum above the Coulomb barrier, and decreases exponentially at high energies. Such a shape can be well approximated by Maxwell function used in the moving source model. Furthermore, such a shape of the energy spectra was observed in the experiments performed in inverted kinematics [49], i.e., experiments in which heavy projectile was impinging on the hydrogen target. In these experiments all ejectiles have large enough kinetic energy to be detected, thus also these parts of the spectra were measured which are not accessible in the PISA experiment.

Table 3.5. Normalization factors with statistical errors and values of parameters  $\sigma$  fitted to isotopic spectra. The right column contains values of total cross sections for  ${}^7\text{Be}$  taken from parameterization of literature data published in ref. [29].

Energy GeV	Normalization factor	$\sigma_{{}^7\text{Be}}$ [29] mb
1.2	0.0878 ( $\pm 8.6\%$ stat.)	3.990
1.9	0.110 ( $\pm 9.0\%$ stat.)	7.078
2.5	0.179 ( $\pm 10.0\%$ stat.)	9.151

## Chapter 4

# The experimental results

The data collected by PISA experiment, are presented in this chapter. In the first section the comparison with the literature data is performed whereas in next two sections representative examples of light charged particle (LCP) and intermediate mass fragment (IMF) spectra are discussed.

### 4.1. The comparison of present data with those from the literature

It is very fortunate that the proton-Ag reactions were recently measured by another group (Herbach et al. [32]) exactly at the same proton beam energy as one of the energy values (1.2 GeV) used in the present experiment. The data of Herbach et al., contain both, LCP and IMF data thus they can be straightforward compared with current results. The statistics of data from that experiment is poorer than statistics of PISA data therefore the present double differential cross sections  $\frac{d^2\sigma}{dEd\Omega}$  have to be integrated over the angles or even over the angles and energies of ejectiles, for comparison to single differential cross sections  $d\sigma/dE$  and total production cross sections  $\sigma$  of Herbach et al.

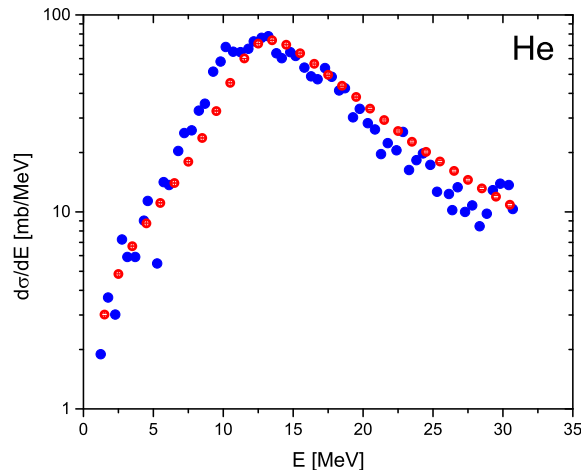


Figure 4.1. Comparison of  $d\sigma/dE$  cross sections obtained by angle integration of the double differential cross sections  $\frac{d^2\sigma}{dEd\Omega}$  for helium ejectiles (the  $^3\text{He}$ ,  $^4\text{He}$  and  $^6\text{He}$  data are added) published in ref. [32] (blue dots) and present  $\frac{d^2\sigma}{dEd\Omega}$  (red dots) prepared in the same manner.

It is clear that both, the absolute magnitude of the cross sections for He as well as the shape of the angle integrated spectrum agree very well for both experiments. The same, or even better agreement may be observed for intermediate mass fragments data, represented in ref. [32] by spectra of lithium and beryllium ions also summed over isotopes. It can be seen in fig. 4.2.

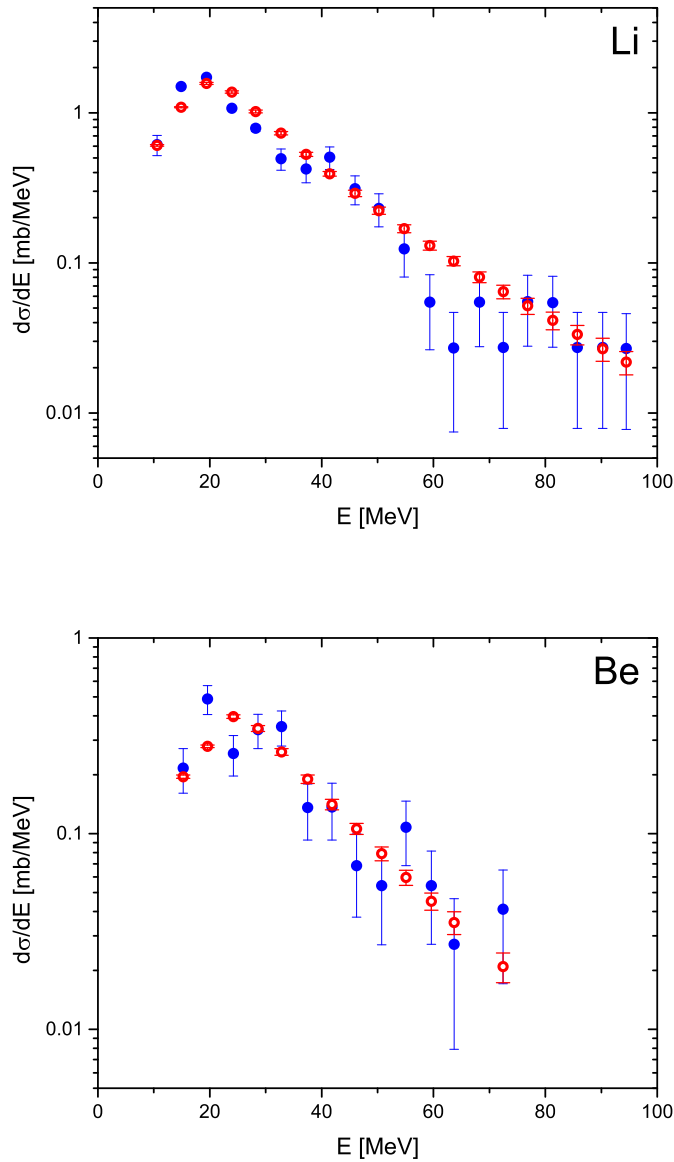


Figure 4.2. Angle integrated and summed over isotopes differential cross sections  $\frac{d^2\sigma}{dE d\Omega}$  for production of lithium (upper panel) and beryllium (lower panel) particles. Blue dots represent data of Herbach et al. [32] whereas the open circles depict the data from present experiment.

The scatter of points from [32] is larger than that of the present data what indicates that statistics of the present experiment is better than that of Herbach et al. Nevertheless, the present data perfectly follow the shape and the magnitude of the literature data.

The total production cross sections for all measured, isotopically identified reaction products obtained in ref. [32] by angle and energy integration of  $\frac{d^2\sigma}{dEd\Omega}$  are compared in fig. 4.3 with the present  $\frac{d^2\sigma}{dEd\Omega}$  integrated in the same angular and energy range. As can be seen the perfect agreement of all isotopically identified particles was achieved. It should be emphasized that both experiments used completely different experimental methods, i.e., the present experiment was performed on the internal whereas the experiment of Herbach, et al. on the external beam with different detector systems and different method of absolute normalization. Such an excellent agreement proves that results of both experiments are trustworthy.

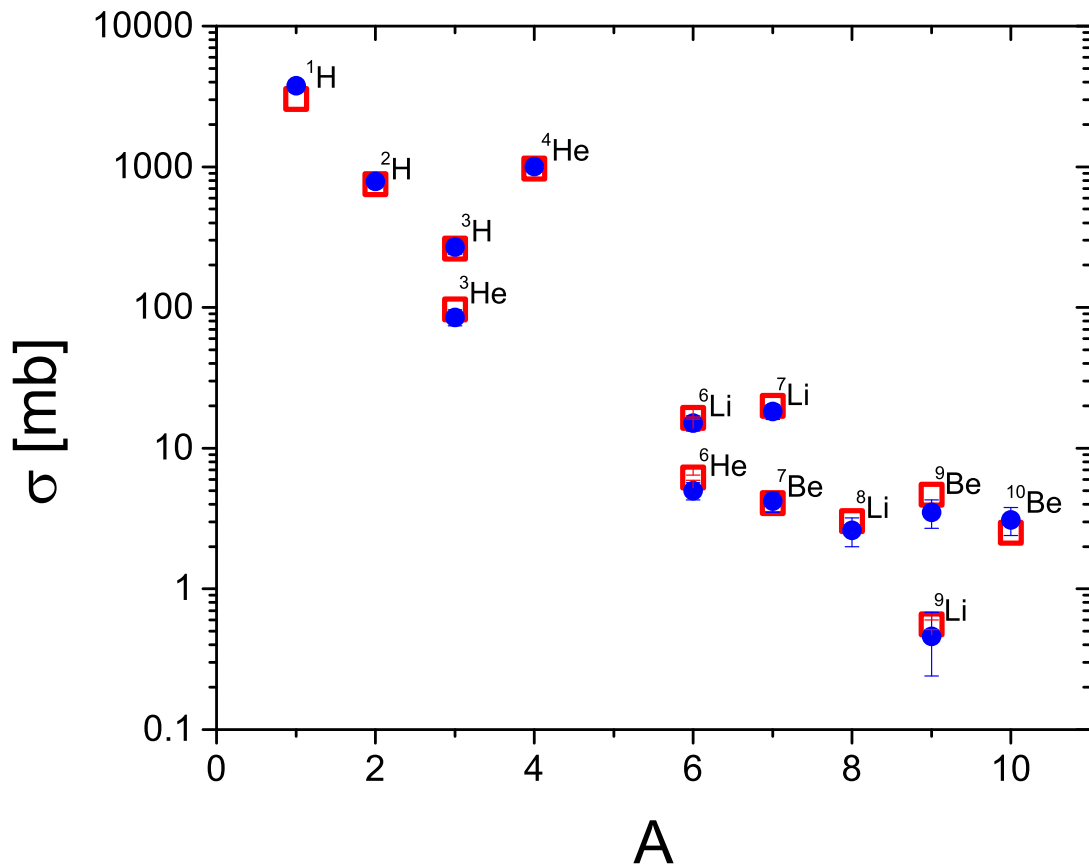


Figure 4.3. Comparison of the total cross sections on  $^{1,2,3}\text{H}$ ,  $^{3,4,6}\text{He}$ ,  $^{6,7,8,9}\text{Li}$  and  $^{7,9,10}\text{Be}$  production. The blue dots present the data taken from [32]. The red squares show the experimental PISA's data. Both sets of data are collected from reactions induced by 1.2 GeV protons on silver target. The double differential cross sections  $\frac{d^2\sigma}{dEd\Omega}$  were integrated over the full range of angles and over the energy range from 0 to 100 MeV.

## 4.2. Light charged particles (LCP)

The double differential cross sections  $\frac{d^2\sigma}{dEd\Omega}$  were measured for three isotopes of hydrogen ( $^{1,2,3}\text{H}$ ) and three isotopes of helium ( $^{3,4,6}\text{He}$ ) for the following laboratory

angles ( $15.6^\circ$ ,  $20^\circ$ ,  $35^\circ$ ,  $50^\circ$ ,  $65^\circ$ ,  $80^\circ$ , and  $100^\circ$ ) at three proton beam energies (1.2 GeV, 1.9 GeV and 2.5 GeV). The angular dependence of the cross sections for LCP is shown in figs. 4.4 and 4.5. The spectra of three isotopes of hydrogen measured at proton beam energy 1.9 GeV are presented in fig. (4.4) for three representative angles  $20^\circ$ ,  $65^\circ$ , and  $100^\circ$ . The spectra of helium isotopes are shown in the same way in fig 4.5. It may be seen that spectra consist of two clearly distinguishable parts. The first of them – the low energy part – is almost independent of angle for all ejectiles. Thus, the emission of particles with kinetic energy in the range of 0 - 25 MeV is isotropic.

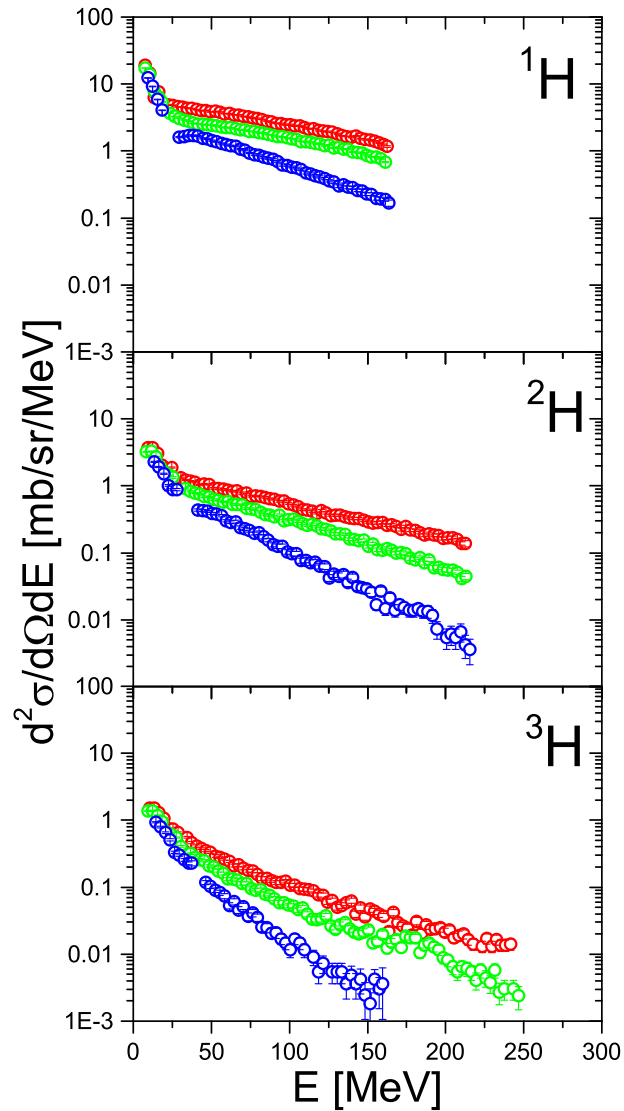


Figure 4.4. The angular dependence of hydrogen isotope spectra for three chosen angles measured at proton beam energy 1.9 GeV. The red dots represents data for  $20^\circ$ , while the green and blue dots depict data for  $65^\circ$  and  $100^\circ$ , respectively.

The second part of spectra, that for kinetic energy bigger than 25 MeV is angle dependent. All spectra monotonically decrease in this energy range, however, the slope of the spectra increases with the scattering angle. This dependence may be easily explained assuming that the high energy particles originate from the first, pre-equilibrium stage of the reaction. In such a case they must preserve memory of the beam direction and therefore they are predominantly emitted in the forward direction.

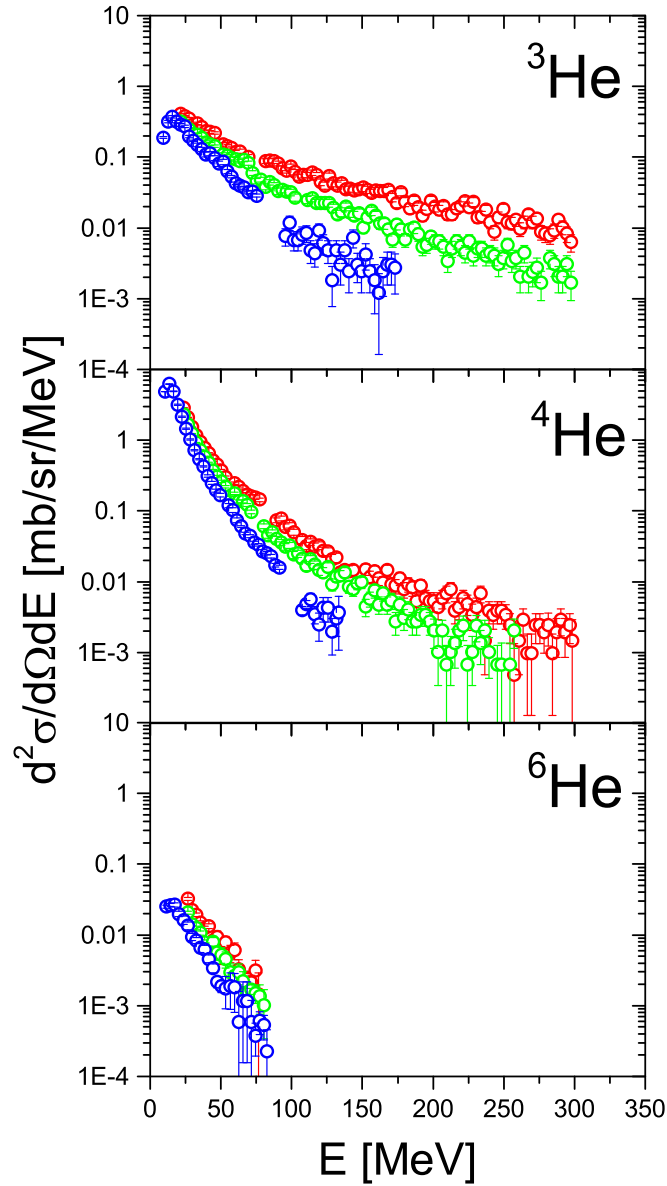


Figure 4.5. The angular dependence of helium isotopes for three chosen angles measured at proton beam energy 1.9 GeV. The red dots represents data for  $20^\circ$ , while the green and blue dots depict data for  $65^\circ$  and  $100^\circ$  respectively.

The beam energy dependence of the LCP experimental spectra is shown in figure 4.6 for hydrogen isotopes and in figure 4.7 for helium isotopes, respectively. It is evident that evolution of the spectra with the proton beam energy is very smooth. Shape of the spectra practically does not change for all isotopes. The only difference is a slight increase of the magnitude of the cross sections with the beam energy.

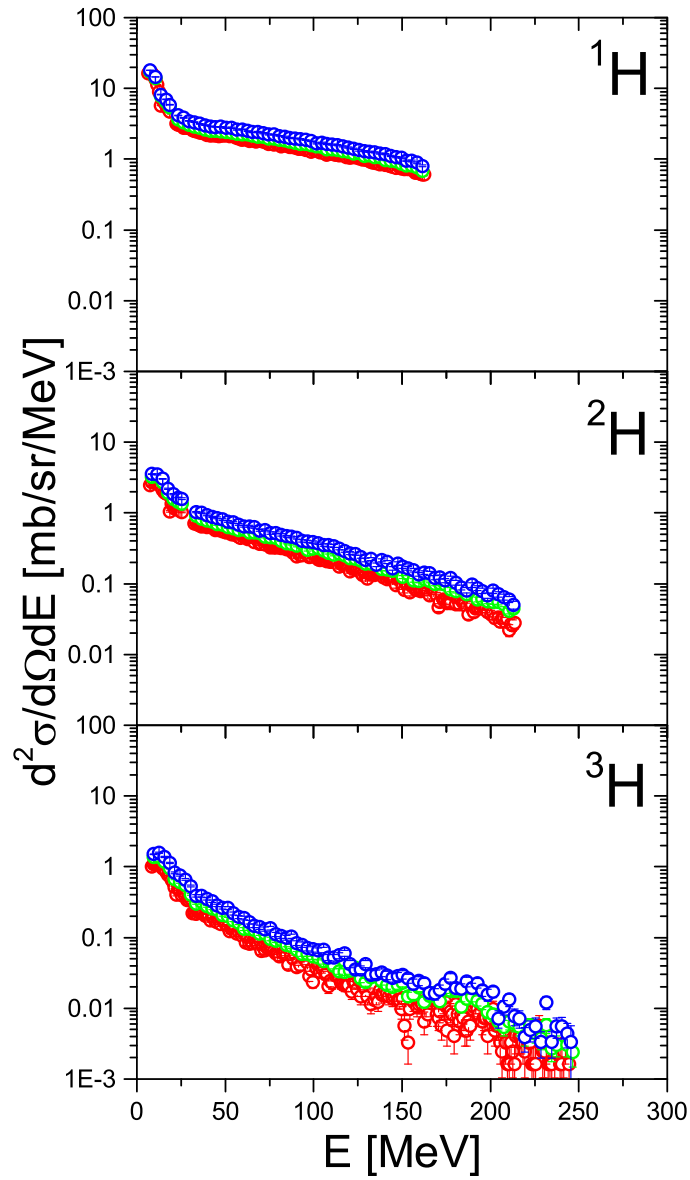


Figure 4.6. The beam energy dependence of the hydrogen spectra for representative angle  $65^\circ$ . The blue dots depict the data measured at the beam energy 2.5 GeV, the green dots represent the data at 1.9 GeV and the red ones correspond to the data at energy 1.2 GeV.

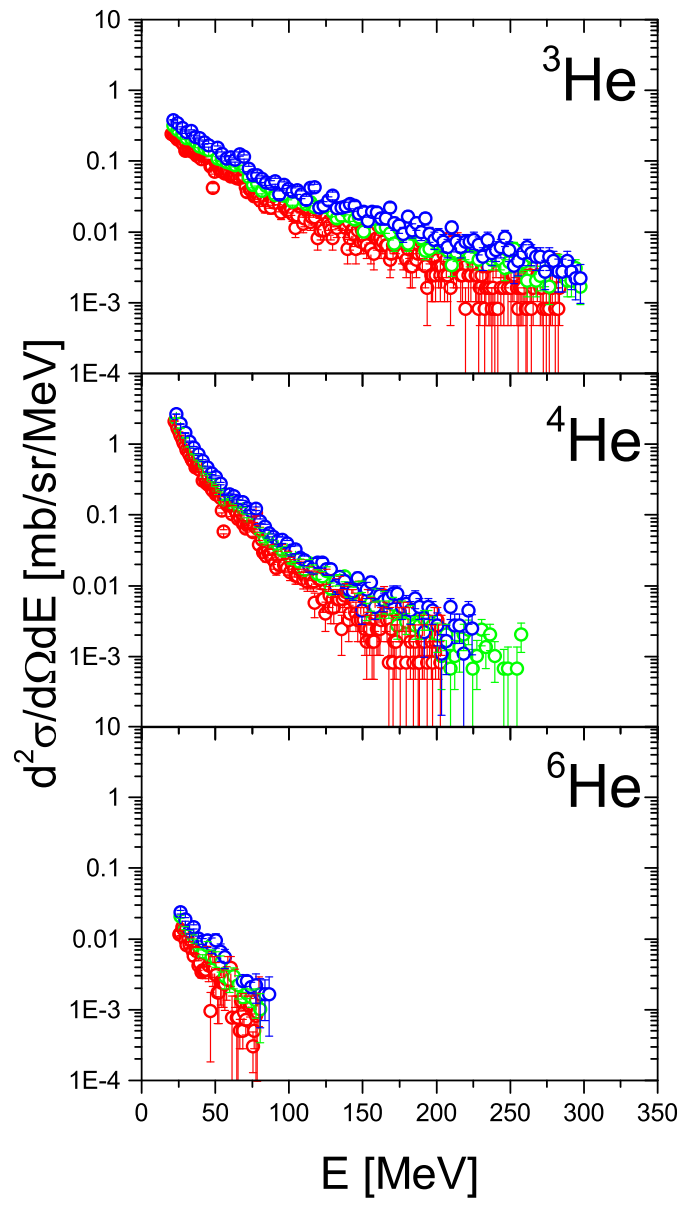


Figure 4.7. The same as in fig. 4.6 but for helium isotopes.

### 4.3. Intermediate mass fragments – IMF

In the present experiment the intermediate mass fragments were detected besides the light charged particles. The spectra of isotopically identified  ${}^6,7,8,9\text{Li}$ ,  ${}^{7,9,10}\text{Be}$ ,  ${}^{10,11,12}\text{B}$  as well as elementally identified spectra of carbon, nitrogen, and oxygen were measured at all three beam energies. The spectra of intermediate mass fragments behave in very similar manner to spectra of light charged particles. Therefore only selected, representative spectra are presented in the current section. The figures in which remaining spectra are shown may be found in the Appendix E.

The spectra of lithium isotopes measured at  $35^\circ$ ,  $50^\circ$ , and  $100^\circ$  are presented in fig. 4.8. Similarly to the hydrogen and helium spectra two energy parts of the spectra may be distinguished. The low energy part is isotropic whereas the high energy tail of the spectra become significantly steeper with the increasing scattering angle.

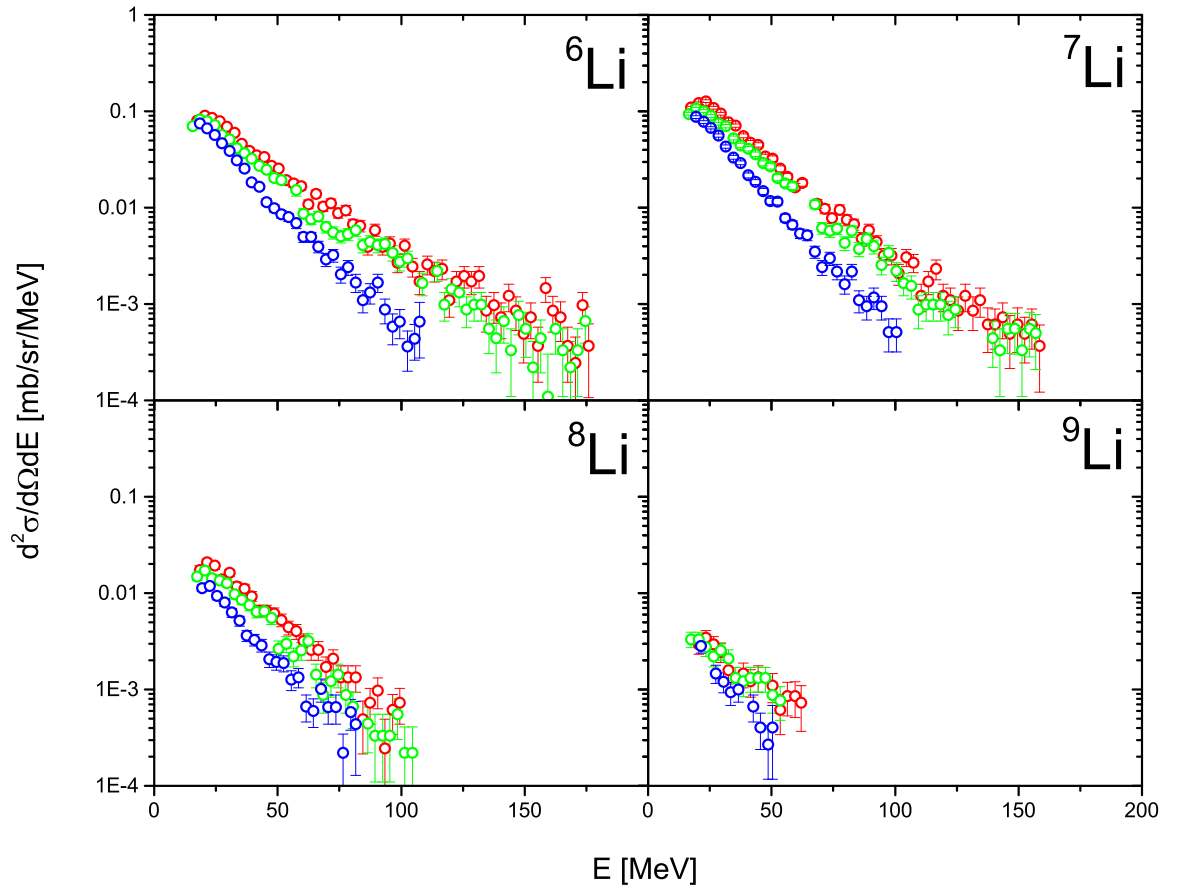


Figure 4.8. Evolution of the shape of lithium isotope spectra with the scattering angle. The red dots represent data measured at proton beam energy 1.9 GeV for  $35^\circ$ , while the green and blue dots depict the data for  $50^\circ$  and  $100^\circ$ , respectively.

The energy dependence presented in the figure 4.9 shows the same behavior like described above for the helium and hydrogen. The shape of the spectra is identical for every isotope. The largest cross sections are at the highest beam energy of 2.5 GeV and the lowest at the lowest proton energy of 1.2 GeV.

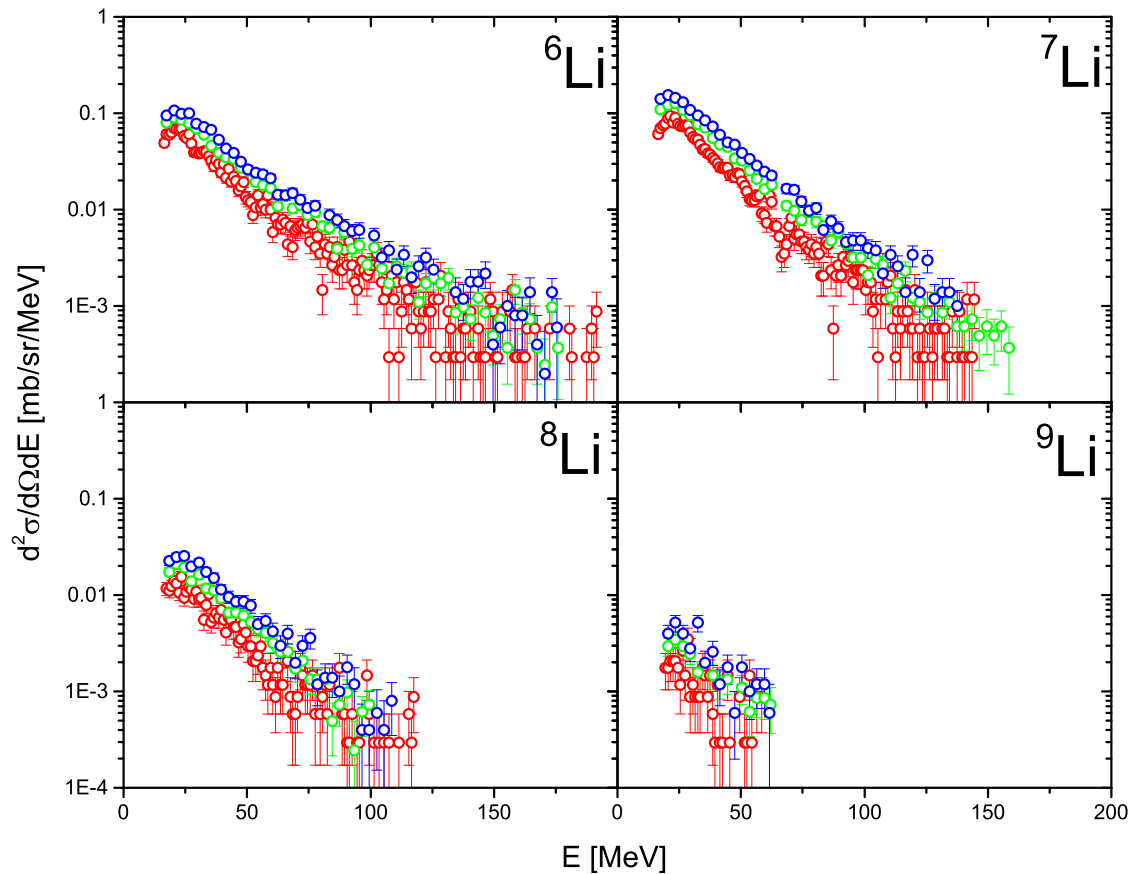


Figure 4.9. Evolution of the lithium spectrum measured at  $50^\circ$  with the beam energy. The blue dots correspond to data measured at the proton beam energy 2.5 GeV, the green dots represent data at 1.9 GeV, and the red ones depict the data for 1.2 GeV energy.

The heaviest registered reaction products are presented in figures 4.10 and 4.11. The angular and energy dependences of these data are almost the same as those for lighter particles. The poor statistics of the carbon, nitrogen, and oxygen ejectiles does not allow us to distinguish individual isotopes of these elements but it is clear that the same, general trend is preserved as for lighter products.

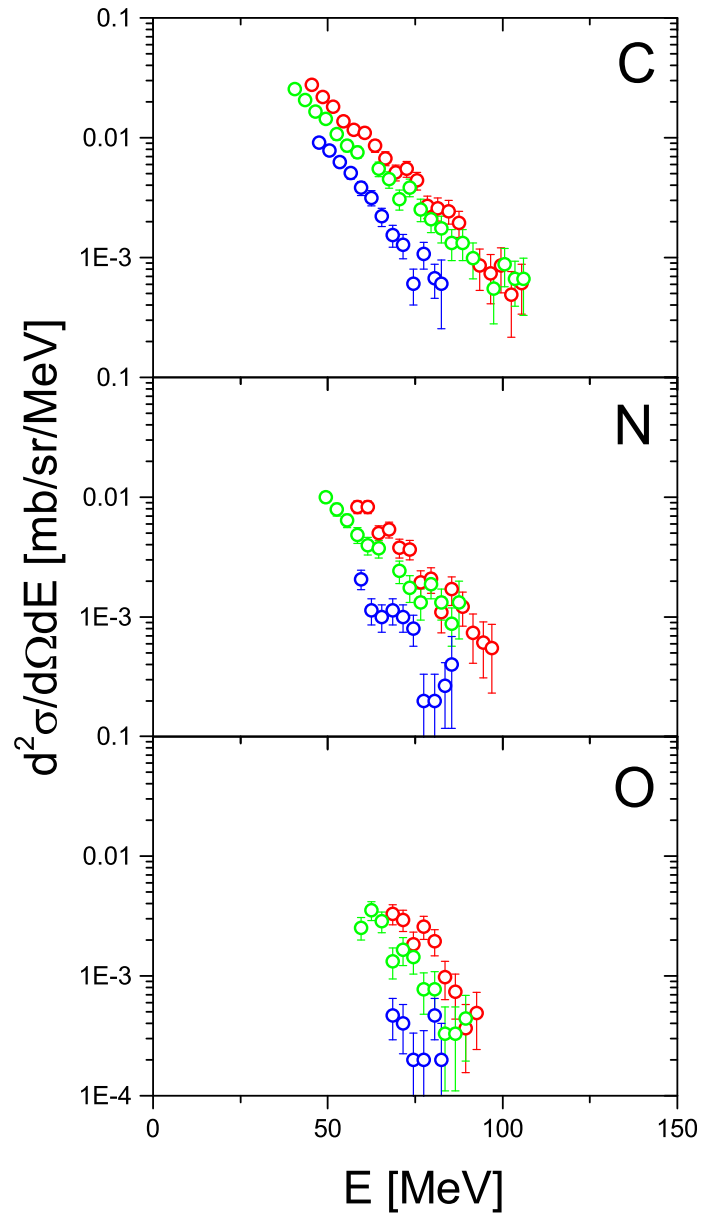


Figure 4.10. Experimental spectra collected for carbon (upper panel), nitrogen (middle panel), and oxygen (bottom panel) measured for the proton beam energy of 1.9 GeV. Red dots represent data measured at the scattering angle of  $35^\circ$ , green dots correspond to  $50^\circ$ , and blue ones depict results for  $100^\circ$ .

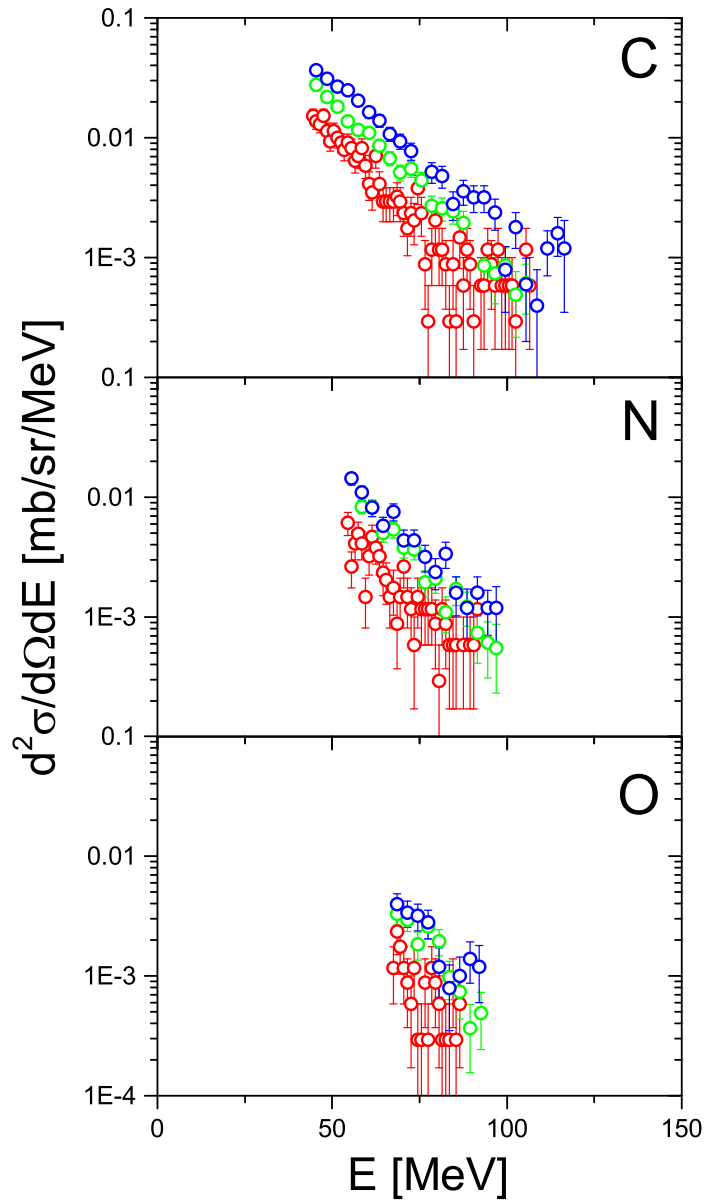


Figure 4.11. Experimental spectra for carbon (upper panel), nitrogen (middle panel), and oxygen (bottom panel) measured at angle of  $35^\circ$  for three proton beam energies. Red points depict data collected at 1.2 GeV, green points at 1.9 GeV, and blue ones at 2.5 GeV.

## Chapter 5

# The microscopic models of the reaction mechanism

In the current chapter the microscopic theoretical models of the proton induced reactions will be presented. The most popular approach to the theoretical description of the reactions induced by GeV proton was initially proposed by R. Serber [50] in 40's past century. It consists in assumption that they proceed in two steps.

In the first stage of the reaction the impinging proton causes a cascade of nucleon-nucleon and pion-nucleon collisions inside the atomic nucleus. Some of the nucleons or groups of them can escape from the nucleus, taking significant part of the accessible energy, while the rest of the energy is absorbed by the nucleus what leads to its excitation. Thus the pre-equilibrium stage of the reaction is characterized by the emission of fast, energetic particles. The model assumes that there are mainly nucleons and light charged particles (LCP). The momentum conservation principle causes that they are moving predominantly along the beam direction. The model calculations are carried out until the excited nuclei reach an equilibrium state. In the second stage of the reaction the excited residual nuclei undergo the de-excitation by different processes which are described by appropriate reaction models.

In the next section the intranuclear cascade model will be discussed as an example of the typical reaction model of the first step of the proton-nucleus collisions. The models responsible for de-excitation of the residual, excited nucleus are described in the following sections.

### 5.1. The intranuclear cascade model - INCL

The basic assumption of all intranuclear cascade models is that the main process responsible for interaction of high energy proton with the atomic nuclei is a cascade of nucleon-nucleon collisions. The interaction with the mean field of the total nucleus as well as collisions with groups of nucleons are treated as possible corrections in some of the realizations of the model.

The most involved and sophisticated version of the intranuclear cascade is the INCL (IntraNuclear Cascade Liège) model. Here the main properties of this model are presented. It was initially invented by J. Cugnon et al. [51], [52]. The physical effects which were taken into account in the INCL code will be briefly discussed below:

#### The static potential well

According to the basic assumption of the INCL model the nucleons of the nucleus are bound in the static (time independent) potential. This potential is taken in the shape of the square well, however, the momentum dependent radius  $R(p)$  of the well

is used. This causes effectively a presence of the diffuse nuclear surface. The radius  $R(p)$  of the potential well is defined by formula:

$$\left(\frac{p}{p_F}\right)^3 = -\frac{4\pi}{3A_T} \int_0^{R(p)} \frac{d\rho(r)}{dr} r^3 dr \quad (5.1)$$

where  $p$  denotes the nucleon momentum,  $p_F$  is the Fermi momentum,  $\rho$  is used for spatial density distribution function of nucleons, and  $A_T$  corresponds to the mass number of the target nucleus.

### The spatial and momentum distributions of nucleons

The Saxon-Woods formula (eq. 5.2) has been used to describe the spatial distribution of the nucleons inside the target nucleus:

$$\rho(r) = \begin{cases} \rho_0 / [1 + \exp(\frac{r-R_0}{a})] & \text{for } r < R_{max} \\ 0 & \text{for } r \geq R_{max} \end{cases} \quad (5.2)$$

with a cut at  $R_{max} = R_0 + 8a$ .

The parameters  $R_0$  and  $a$  have a meaning of radius of the nucleon density distribution and its diffuseness, respectively. They are fixed in the INCL code according to the following formulas:

$$R_0 = (2.745 \times 10^{-4} A_T + 1.063) A_T^{1/3} fm \quad (5.3)$$

and

$$a = 0.51 + 1.63 \times 10^{-4} A_T fm. \quad (5.4)$$

The  $\rho_0$  parameter value has been adjusted to assure that the distribution is normalized to  $A_T$ , the target mass number.

The uniform momentum distribution of the nucleons in the target was assumed, i.e. the nucleon momenta were chosen randomly from a sphere with the radius equal to the Fermi momentum  $p_F$ .

The following algorithm is applied to generate the initial momentum  $\vec{p}$  and position  $\vec{r}$  of each target nucleon:

- ◇  $\vec{p}$  is chosen randomly in a sphere of radius  $p_F$ ,
- ◇ momentum dependent radius  $R(p)$  of the spatial sphere is calculated according to formula 5.1.

The position  $\vec{r}$  of the nucleon is randomly selected inside this sphere.

### Collisions inside the nucleus

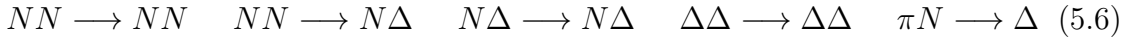
Nucleons in the proton - target nucleus system are divided into two groups. The first group, spectators, consists of nucleons which are not involved in previous collisions. The second group consists of nucleons already engaged in them. At the beginning of the reaction only the beam nucleon belongs to the second group.

Collisions between spectators are not allowed. The cascade starts at the first collision of the proton impinging on to nucleus with one of the spectators. Then this spectator leaves its group moving to the group of active nucleons and may take part in the next collisions.

The nucleons inside the nucleus matter move along straight lines as long as two of them do not collide or until they reach the surface of the nucleus (they can be transmitted through the nuclear surface or be reflected from it). The collision occurs when the distance between two interacting particles is smaller than the minimal distance defined by eq. (5.5), where the  $\sigma_{total}$  is the total nucleon-nucleon cross section.

$$d_{minimal} \leq \sqrt{\sigma_{total}/\pi} \quad (5.5)$$

Two nucleons can scatter both elastically and inelastically, in agreement with the momentum and energy conservation law. During the inelastic interaction the  $\Delta$  creation occurs, which later decays into pion and nucleon. The following sets of possible reactions are considered:



The final state of the particles after collisions is influenced by the Pauli blocking effect. The main idea of the implementation of this effect is as follows:

Let the  $p_n$  and  $p_m$  will be the probability of the phase space occupation by  $n$  and  $m$ -particles, then the probability of the collision can be expressed by  $P = (1 - p_n)(1 - p_m)$ . The key is in the calculation of the  $p_n$ , which is realized by counting nearby nucleons in a small volume of the phase space eq. (5.7), with  $r_{Pauli} = 3.18 fm$  and  $p_{Pauli} = 200 MeV/c$ .

$$p_n = \frac{1}{2} \frac{(2\pi\hbar)^3}{\frac{4\pi}{3} r_{Pauli}^3 \frac{4\pi}{3} p_{Pauli}^3} \sum_{i \neq n} \theta(r_{Pauli} - |\vec{r}_i - \vec{r}_n|) \times \theta(p_{Pauli} - |\vec{p}_i - \vec{p}_n|) \quad (5.7)$$

The sum in the eq. (5.7) is limited to the nucleons with the same isospin as the particle  $n$ . The factor  $\frac{1}{2}$  is caused by presence of two spin components which are not treated explicitly.

### The coalescence

To enable the emission of particles built of several nucleons, i.e. light charged particles, the coalescence mechanism was introduced into the INCL code [5]. The clue of this approach is allowing the escaping nucleons to attach additional nucleons. Those particles have to fulfill the criterion of proximity in the phase space i.e. the escaping nucleons can attach other nucleons if they are close in the spatial and momentum distance.

The largest ejectile which can be created by the coalescence process in the INCL4.3 code is the atomic nucleus of helium ( ${}^4He$ ) [5]. The probability of emitting heavier particles decreases rapidly. Recently attempt was undertaken to increase the range of masses of the particles created by the coalescence (see ref. [6]), however, it was found that the coalescence leading to heavier complex particles than  ${}^4He$  does not reproduce satisfactorily the experimental spectra [7]. Formally the criteria of the coalescence are expressed by the following formula:

$$r_{n,n-1} p_{n,n-1} \leq D \quad (5.8)$$

The  $n$  and  $n-1$  enumerate the Jacobi coordinates of the  $n$ -th nucleon of the ejectile in respect to a group of  $n-1$  nucleons of this particle. The  $D$  parameter was chosen to be equal  $387 MeV \frac{fm}{c}$ .

Additional information about the model, details of used parametrization, the criteria of stopping calculation, and so on can be found in refs. [5, 53].

## 5.2. The theoretical models of the second reaction stage

It is generally assumed that after the first, fast stage of the reaction the excited target remnant is in the thermal equilibrium state. Many theoretical models were created to describe possible ways of its de-excitation. They assume different mechanisms of this process. For example it can proceed as sequential or simultaneous emission of particles. The most important of the first kind processes is evaporation of nucleons and complex particles. In the present study the Generalized Evaporation Model - GEM2 of the nuclear evaporation is used [54,55]. The simultaneous emission known also as the multifragmentation is the main process taken into consideration for the highly excited nuclei in the Statistical Multifragmentation Model - SMM [56–58] which is used in the present thesis as an alternative to the evaporation model.

### 5.2.1. Generalized Evaporation Model - GEM2

GEM2 uses the classical Weisskopf - Ewing formalism [59, 60] which assumes that emission of the particle with mass- and atomic-numbers ( $A_n, Z_n$ ) in its ground state from excited atomic nucleus (with mass  $A_T$ , charge  $Z_T$ , and excitation energy  $E_T^*$ ) occurs with probability  $P_n(E_{kin})$  dependent on its kinetic energy  $E_{kin}$ .

$$P_n(E_{kin})dE_{kin} = g_n\sigma_{inv}(E_{kin})\frac{\rho_{new}(E_T^* - Q - E_{kin})}{\rho_T(E_T^*)}E_{kin}dE_{kin} \quad (5.9)$$

In equation (5.9)  $Q$  is the  $Q$ -value of the reaction in which the *new* target remnant is created by emission of particle  $n$ . The quantities  $\rho_{new}$  and  $\rho_T$  describe the density of states for original target remnant -  $T$ , and for the newly created nucleus - *new*. The  $\sigma_{inv}(E_{kin})$  is the cross section for inverse reaction to the evaporation of the particle  $n$ , while the factor  $g_n$ , used for normalization, can be expressed by the formula (5.10) (where  $S_n$  and  $A_n$  are the spin and mass of the emitted particle, respectively):

$$g_n = \frac{(2S_n + 1)A_n}{\pi^2\hbar^2} \quad (5.10)$$

Table 5.1. The set of isotopes explicitly considered as ejectiles by the GEM2 code.

$Z_n$	Ejectiles							
0	$n$							
1	$p$	$d$	$t$					
2	${}^3He$	${}^4He$	${}^6He$	${}^8He$				
3	${}^6Li$	${}^7Li$	${}^8Li$	${}^9Li$				
4	${}^7Be$	${}^9Be$	${}^{10}Be$	${}^{11}Be$	${}^{12}Be$			
5	${}^8B$	${}^{10}B$	${}^{11}B$	${}^{12}B$	${}^{13}B$			
6	${}^{10}C$	${}^{11}C$	${}^{12}C$	${}^{13}C$	${}^{14}C$	${}^{15}C$	${}^{16}C$	
7	${}^{12}N$	${}^{13}N$	${}^{14}N$	${}^{15}N$	${}^{16}N$	${}^{17}N$		
8	${}^{14}O$	${}^{15}O$	${}^{16}O$	${}^{17}O$	${}^{18}O$	${}^{19}O$	${}^{20}O$	
9	${}^{17}F$	${}^{18}F$	${}^{19}F$	${}^{20}F$	${}^{21}F$			
10	${}^{18}Ne$	${}^{19}Ne$	${}^{20}Ne$	${}^{21}Ne$	${}^{22}Ne$	${}^{23}Ne$	${}^{24}Ne$	
11	${}^{21}Na$	${}^{22}Na$	${}^{23}Na$	${}^{24}Na$	${}^{24}Na$	${}^{25}Na$		
12	${}^{22}Mg$	${}^{23}Mg$	${}^{24}Mg$	${}^{25}Mg$	${}^{26}Mg$	${}^{27}Mg$	${}^{28}Mg$	

One of the most significant extensions of the classical formulas is possibility of emitting the excited particles. This improves the agreement of calculated cross sections on IMF production with those observed experimentally.

In the GEM2 code the values of the inverse cross sections can be calculated in two ways according to Dostrovsky [61], and Furihata [55] formulas. For purposes of current study the Furihata approach was used.

The density of states was calculated in agreement with the Fermi-gas model with level density parameter formula proposed by the Gilbert, Cameron, Cook and Ignatyuk [62].

The GEM2 computer program considers 66 stable and long living isotopes as the ejectiles. All of them are listed in the table 5.1.

### 5.2.2. Statistical Multifragmentation Model - SMM

In this section another approach to the transition from excited target remnant to the final nuclei, i.e., multifragmentation is discussed. Multifragmentation models, start with the assumption that the excited nucleus is in the thermodynamical equilibrium. Such an excited nucleus can undergo volume fluctuations. If the volume becomes large the density of the nucleus can appear to be smaller than the ground state density. In such a situation one can treat the nuclear matter as a „bubble phase”, i.e. the regions of much smaller density („bubbles”) can be created in the more dense surrounding. This leads to instability of the nucleus which therefore can split into several pieces. Furthermore, if the average density is smaller than half of the ground state density the nucleus behaves like a gas container with set of droplets of liquid which can escape from the excited nucleus being observed as light charged particles or intermediate mass fragments.

During such fluctuations nuclear system can also loose the excitation energy by evaporation or fission. The most complete approach to the statistical multifragmentation is realized by SMM code of Botvina et al. [56, 63].

In this code it is assumed that at first the atomic nuclei expand and after achieving small enough density break up into nucleons and heavier fragments, which still could be excited. It may be expected that the pure statistical approach allows to consider all possible breakup channels as equally probable. However, it was shown that the probability  $W_f$  of a specified decay channel  $f$  is proportional to the exponential function of the entropy  $S_f(E^*)$ , where  $E^*$  is the excitation energy of the nucleus [56]:

$$W_f \propto \exp(S_f(E^*)) \quad (5.11)$$

Because the model treats compound nucleus as one of possible decay channels, it allows for the smooth transition from evaporation at low excitation energies to the simultaneous fragmentation for high energies according to the accessible phase space for fragments. The fragments with the mass number smaller or equal to four are treated as stable particles - LCP. The fragments heavier than  $A=4$  are considered as heated drops of the nuclear matter, and their energy is calculated in accordance with the liquid-drop model. Their decay is then described by the Fermi breakup model [64]. The products with mass bigger than  $A=16$  may loose their energy by the evaporation/fission mechanism. The mutual Coulomb interaction between

fragments is taken into consideration in the frame of the Wigner-Seitz approximation [56]. All ejectiles after fragmentation and de-excitation are propagated in the Coulomb field.

### 5.3. The comparison of the theoretical calculations with the experimental data

The experimental data were compared with the model calculations performed for the appropriate beam energies and the scattering angles. INCL4.3 - the model of the first stage of the reaction - describes the production of light ejectiles with the mass number  $A \leq 4$  and atomic number  $Z \leq 2$ . The fragments built of two or more nucleons are created by the coalescence of nucleons during the cascade of the nucleon-nucleon collisions. The emission of particles from the excited nucleus remnant in the second stage of the reaction was treated by GEM2 or SMM model. The neutrons and LCP (light charged particles: p, d, t,  $^3\text{He}$  and  $^4\text{He}$ ) are emitted both, in the first and in the second stage of the reaction whereas the IMF (intermediate mass fragments with the atomic number  $Z \geq 3$ ) originate only from the second step of the process. The obtained results are presented in the following subsections.

#### 5.3.1. Angular dependence of light charged particle data

In this subsection the variation of the cross section with the scattering angle is discussed using as an example the data measured at 1.2 GeV proton beam energy for two scattering angles:  $20^\circ$  and  $100^\circ$ . The shape of the spectra is practically the same for the cross sections measured at higher beam energies (1.9 and 2.5 GeV). The data and model calculations for hydrogen isotopes are shown in fig. 5.1 whereas those for helium isotopes are presented in fig. 5.2. The full dots depict the cross sections measured at  $20^\circ$  and the open circles correspond to  $100^\circ$  data. The solid lines present calculations made for  $20^\circ$  whereas the dashed lines show model results for  $100^\circ$ . The green lines represent calculations performed in the frame of the INCL4.3 model, the blue and red lines depict GEM2 and SMM results, respectively.

As can be seen the data for all ejectiles do not change with the angle when their energy is smaller than  $\sim 25$  MeV. For higher energies the exponential tail of spectra is more steep for  $100^\circ$  than for  $20^\circ$ . Thus it may be stated that two components are visible in the experimental spectra: the isotropic, low energy component and the high energy one which strongly decreases with the increasing scattering angle. It may be conjectured that the isotropic emission is mainly due to the presence of the equilibrated, excited nucleus whereas the anisotropic emission is characteristic for fast, non-equilibrium stage of the reaction. Indeed, the anisotropic component of theoretical spectra in fig. 5.1 is only due to the first stage of the reaction - its shape and character of the angular dependence is reproduced by INCL4.3. The agreement of the model cross sections with the data is the best for tritons and deteriorates for lighter hydrogen isotopes being the poorest for protons. Furthermore, the data for  $100^\circ$  are well described for all isotopes, whereas the description deteriorates with decreasing scattering angle. This may suggest that some specific mechanism, not taken into consideration in the INCL4.3 model, is present in the first stage of the reaction. It manifests itself mainly for forward scattering angles and lightest ejectiles. The same conclusions may be derived from inspection of fig. 5.2 where  $^3\text{He}$

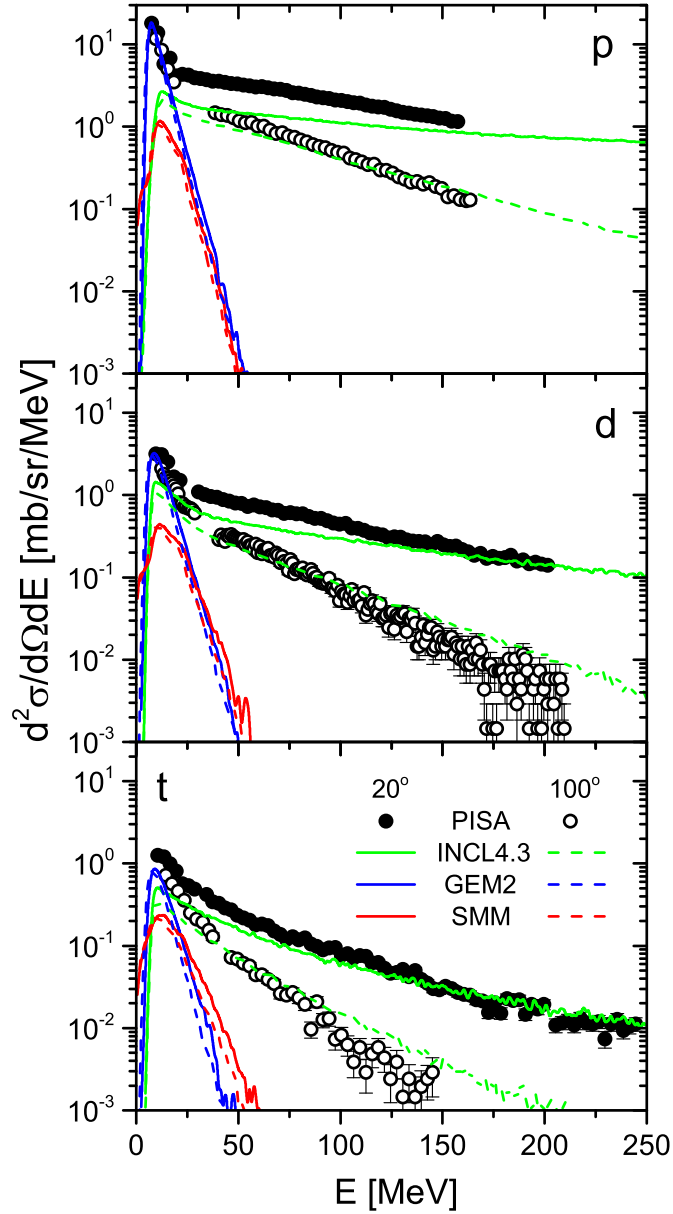


Figure 5.1. Comparison of the double differential cross sections  $\frac{d^2\sigma}{dE d\Omega}$  calculated by various models with the experimental data for hydrogen isotopes. Full and open dots represent the experimental data measured for proton beam energy 1.2 GeV at  $20^\circ$  and  $100^\circ$ , respectively. Solid lines depict results of calculations performed for  $20^\circ$  and the dashed lines those for  $100^\circ$ . The green, blue, and red colors indicate calculations due to INCL4.3, GEM2, and SMM model, respectively.

and  $^4\text{He}$  spectra behave in the same manner like spectra of tritons in fig. 5.1. The isotropic component of the p, d, and t spectra as well as that of  $^3\text{He}$  and  $^4\text{He}$  spectra is well described by GEM2 model which treats emission of these light particles as evaporation process. The spectra evaluated in the frame of the SMM model underestimate significantly the isotropic component for all light charged particles.

It is worth to note that SMM model cross sections agree well with the data for the heaviest helium isotope -  ${}^6\text{He}$  whereas the GEM2 spectra lead to poorer agreement.

In figures 5.1 and 5.2 the sum of results of calculations from particular models was not shown. This sum is presented in fig. 5.3. The energy scale of the figure is enlarged to allow for observation of details of the spectra.

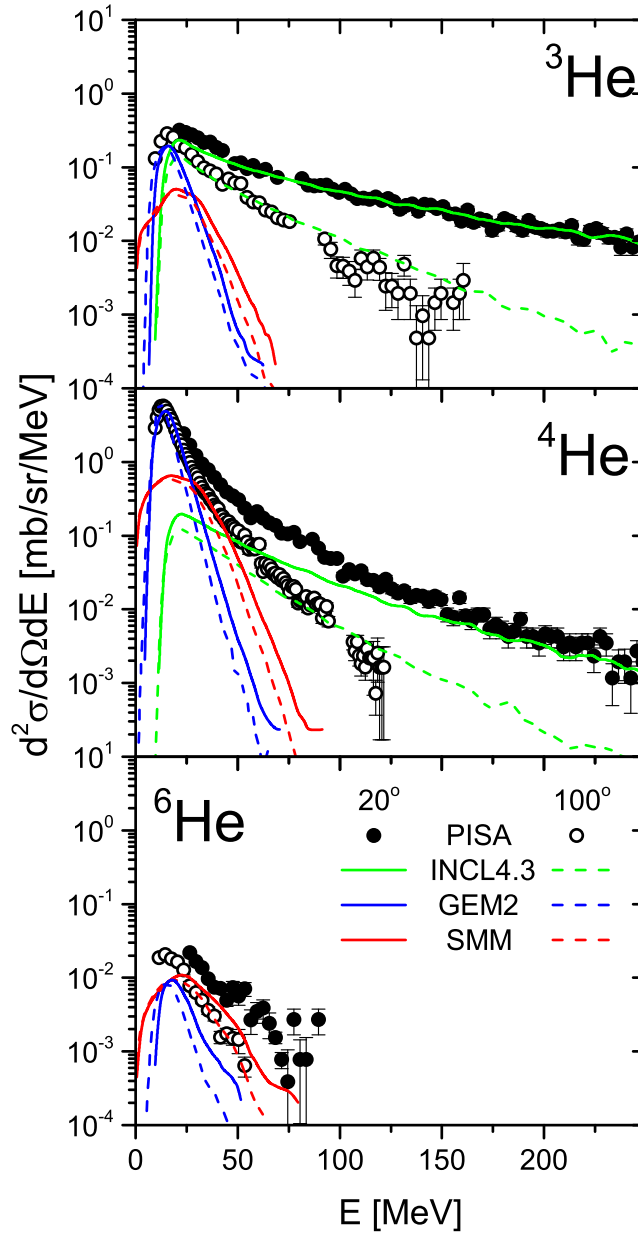


Figure 5.2. The same as in fig. 5.1 but for He isotopes.

### 5.3.2. Beam energy dependence of light charged particle data

In the current subsection the variation of the cross sections with the proton beam energy is presented. The data measured at the angle  $65^\circ$  for two beam energies

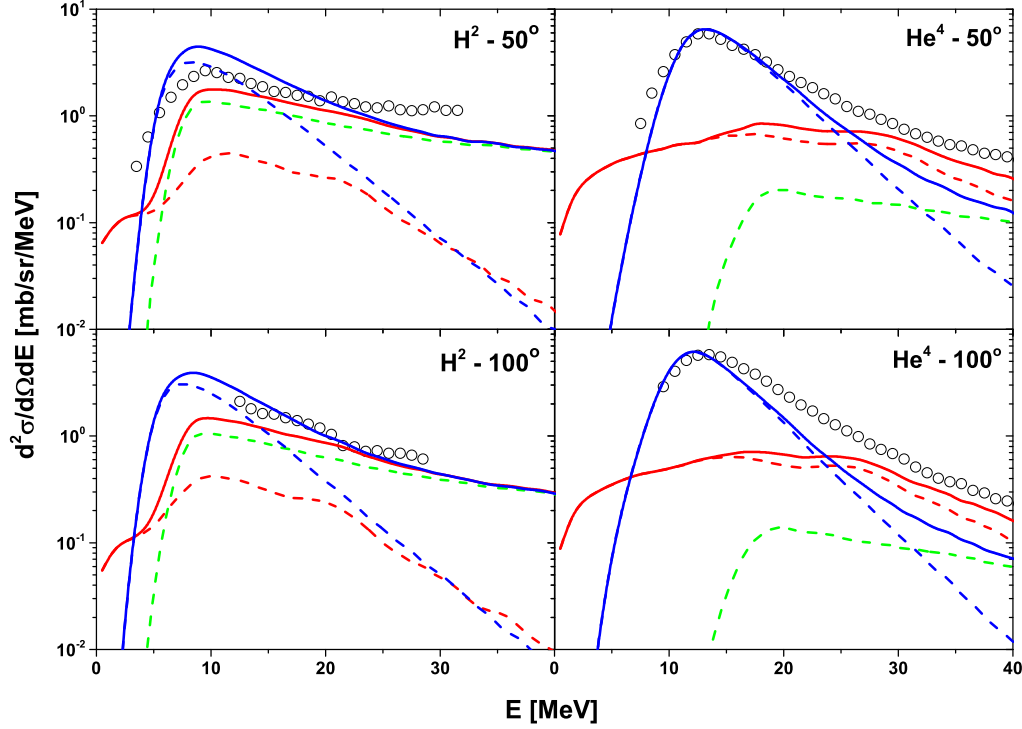


Figure 5.3. Comparison of the double differential cross sections  $\frac{d^2\sigma}{dE d\Omega}$  calculated by various models with the experimental data for deuteron and alpha particles on the left and right panels, respectively. Open dots represent the experimental data measured for proton beam energy 1.2 GeV at 50° and 100°, on upper and lower panels, respectively. Dashed lines present results from calculations in the frame of particular model: INCL4.3, GEM2, and SMM, while solid lines depict sum of them: blue color for INCL4.3+GEM2, and red color for INCL4.3+SMM. The green dashed lines indicate results of INCL4.3 calculations. In order to show discrepancy between experimental data and its description by the microscopic models (GEM2 and SMM) only part of spectra is presented for ejectile energy <40 MeV.

1.2 GeV and 2.5 GeV, are used as examples. The data and model calculations for hydrogen isotopes are shown in fig. 5.4 while those for helium isotopes are presented in fig. 5.5. The experimental data for beam energy 1.2 GeV and 2.5 GeV are represented by the open and full points, respectively. The solid lines correspond to the results of calculations made for proton beam energy of 2.5 GeV whereas the dashed lines presents the calculations performed for 1.2 GeV. The type of used model is indicated by colors as follow: the green lines describe results of INCL4.3 model, the blue lines correspond to the results of GEM2, and the red lines represent the calculation performed by the SMM model.

As can be seen the shape of the experimental spectra for all ejectiles does not change with the beam energy. The only visible difference between measured data is the increase of absolute value of the cross section when the beam energy increases. The same behavior is observed for all ejectiles. The INCL4.3 calculations reproduce only the high energy tail of the spectra,  $E \geq 75$  MeV. Below the results of the first stage model are almost the same for all three beam energies. The spectra in the energy region from 0 to 25 MeV are well described by calculations performed in

the GEM2 model framework. The same relation between calculations for different beam energies, as for experimental data, can be observed. Values of cross sections calculated by this model increase with the impinging proton energy. The agreement of GEM2 calculations with the experimental data is satisfying in the mentioned part of the spectra. In contrast to the mentioned models, the results of the third model - SMM are not in accordance with the measured data. The theoretical cross sections calculated for 1.2 GeV beam energy strongly underestimated the data. On the other hand the predictions of SMM agree much better with the experiment at highest beam energy, i.e. 2.5 GeV. It is interesting to note that the  ${}^6\text{He}$  data are better reproduced by the SMM model than by GEM2 calculations.

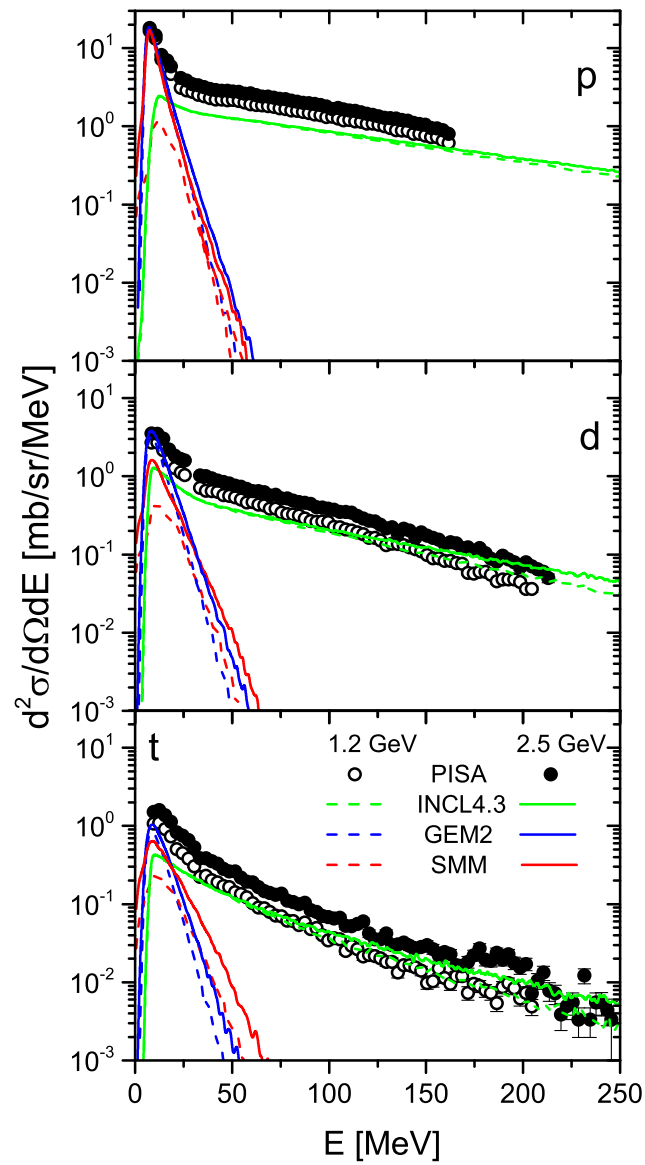


Figure 5.4. Comparison of the double differential cross sections  $\frac{d^2\sigma}{dE d\Omega}$  calculated by various models with the experimental data for hydrogen isotopes. Full and open dots represent the experimental data measured for detection angle  $65^\circ$  at 2.5 GeV and 1.2 GeV, respectively. Solid and dashed lines depict results of calculations performed for the proton beam energies 2.5 GeV and 1.2 GeV whereas the colors: green, blue and red indicate calculations for INCL4.3, GEM2 and SMM model, respectively.

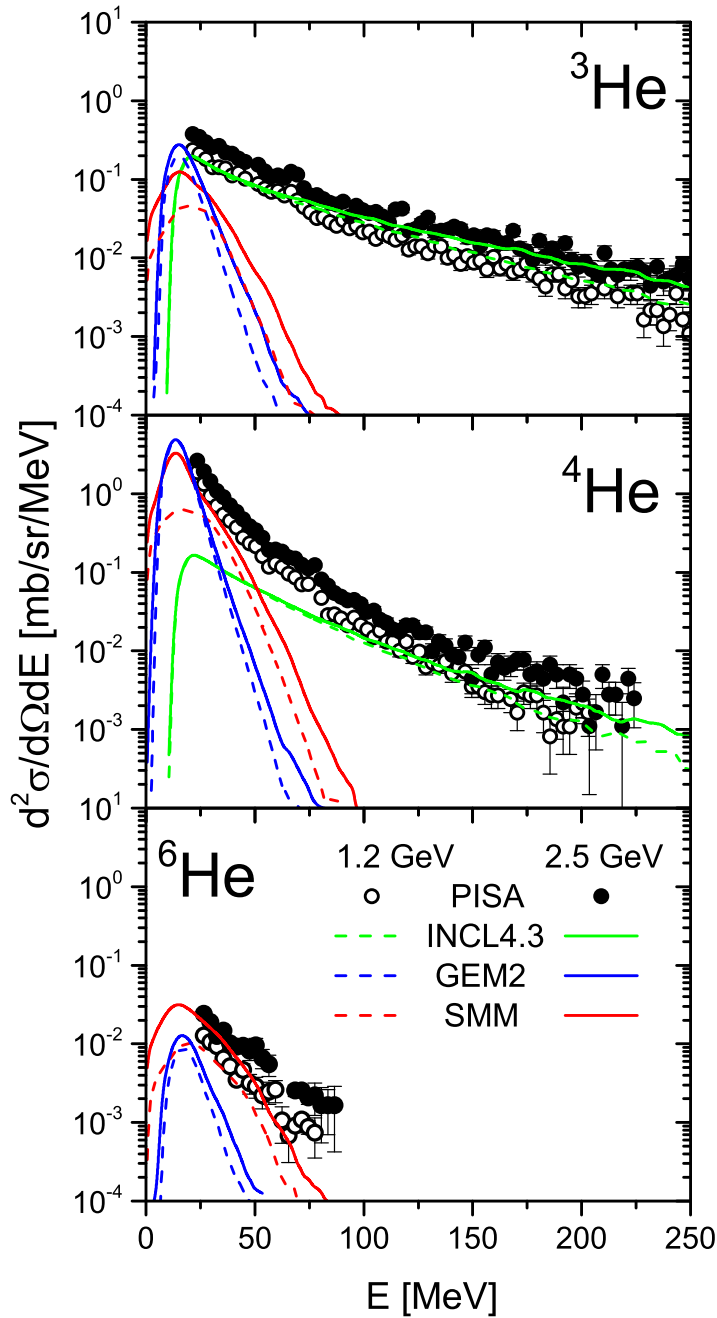


Figure 5.5. The same as in fig. 5.4 but for He isotopes.

### 5.3.3. Angular dependence of intermediate mass fragments emission

In this subsection variation of the double differential cross sections  $\frac{d^2\sigma}{dE d\Omega}$  with the angle is discussed. As examples of experimental data, selected spectra of lithium, beryllium and boron isotopes are presented in figs. 5.6, 5.7, and 5.8, respectively.

They were measured for the proton beam energy 1.2 GeV at the angles  $20^\circ$  and  $100^\circ$ . The full and open dots correspond to the data obtained at  $20^\circ$  and  $100^\circ$ , respectively. The solid lines represent the results of the model calculations performed at  $20^\circ$ , whereas the dashed lines show those at  $100^\circ$ . The used models: GEM2 and SMM are indicated by the color of the lines: blue and red, respectively. The behavior of experimental data is in general very similar to that observed for LCP. The spectra are built of two components. The low energy, isotropic component and the high energy one which is forward peaked. This anisotropy manifests itself in the increasing slope of the high energy tail of the spectra. The tail, which is present in data for all ejectiles, is always steeper for the  $100^\circ$  than for  $20^\circ$ . This effect decreases with the mass of ejectiles.

The INCL4.3 - model of the first stage of the reaction - does not take into consideration the emission of particles composed of more than four nucleons. Therefore all IMF data analyzed in the present work are compared with predictions of the models which assume emission of IMF from the second stage of the reaction. Two models used to reproduce the measured cross sections - GEM2 and SMM - predict bell-shaped energy spectra. The slope of the high energy part of calculated spectra is similar to that of the experimental data measured at  $100^\circ$ , but it is too steep for the  $20^\circ$ . The width of theoretical spectra is always smaller for GEM2 than that for multifragmentation model. Moreover, the cross sections for all ejectiles obtained from the GEM2 calculations are lower than those evaluated by the SMM model and are also smaller than experimental data. Since GEM2 as well as SMM assume emission from equilibrated nucleus one can make conjectures that a large contribution from non-equilibrium processes is present in the experimental data for forward scattering angles. This is the same effect as that observed for LCP. As it was mentioned above, the INCL4.3 model applied in the current work, does not have possibility to coalesce nucleons into particles heavier than alpha particle. So it was impossible to verify mentioned hypothesis. The most modern version of the INCL - the INCL4.6 which allows for coalescence of emitted nucleons into IMF with mass number  $A < 9$  [6] - also does not solve this problem. As it was checked by S. Sharma [7] for an experiment performed with protons of energy 480 MeV impinging on to a silver target, the INCL4.6 underestimates significantly the slope of the high energy tail of the IMF spectra.

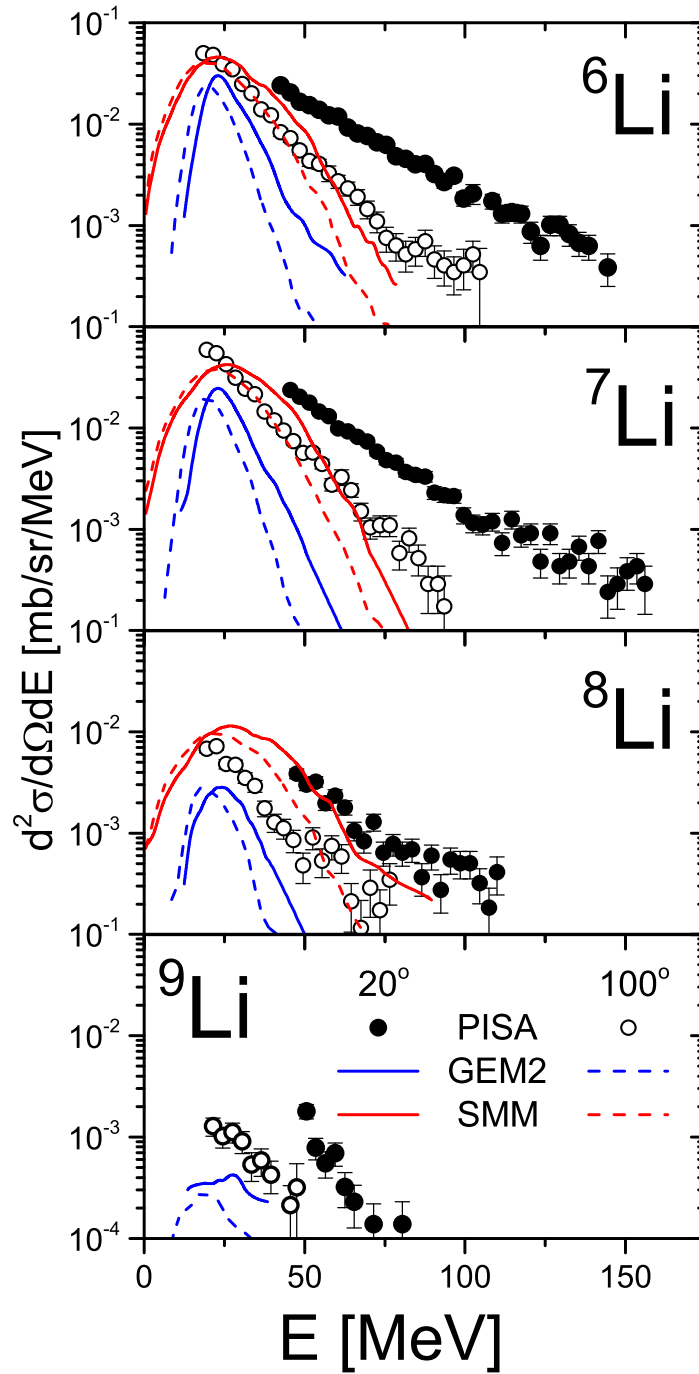


Figure 5.6. Comparison of the double differential cross sections  $\frac{d^2\sigma}{dE d\Omega dE}$  calculated by models of the second stage of the reaction with the experimental data for lithium isotopes. Full and open dots represent the experimental data measured for proton beam energy 1.2 GeV at  $20^\circ$  and  $100^\circ$ , respectively. Solid lines depict results of calculation performed for  $20^\circ$  and the dashed lines those for  $100^\circ$ . The blue and red colors indicate calculations for GEM2 and SMM model, respectively.

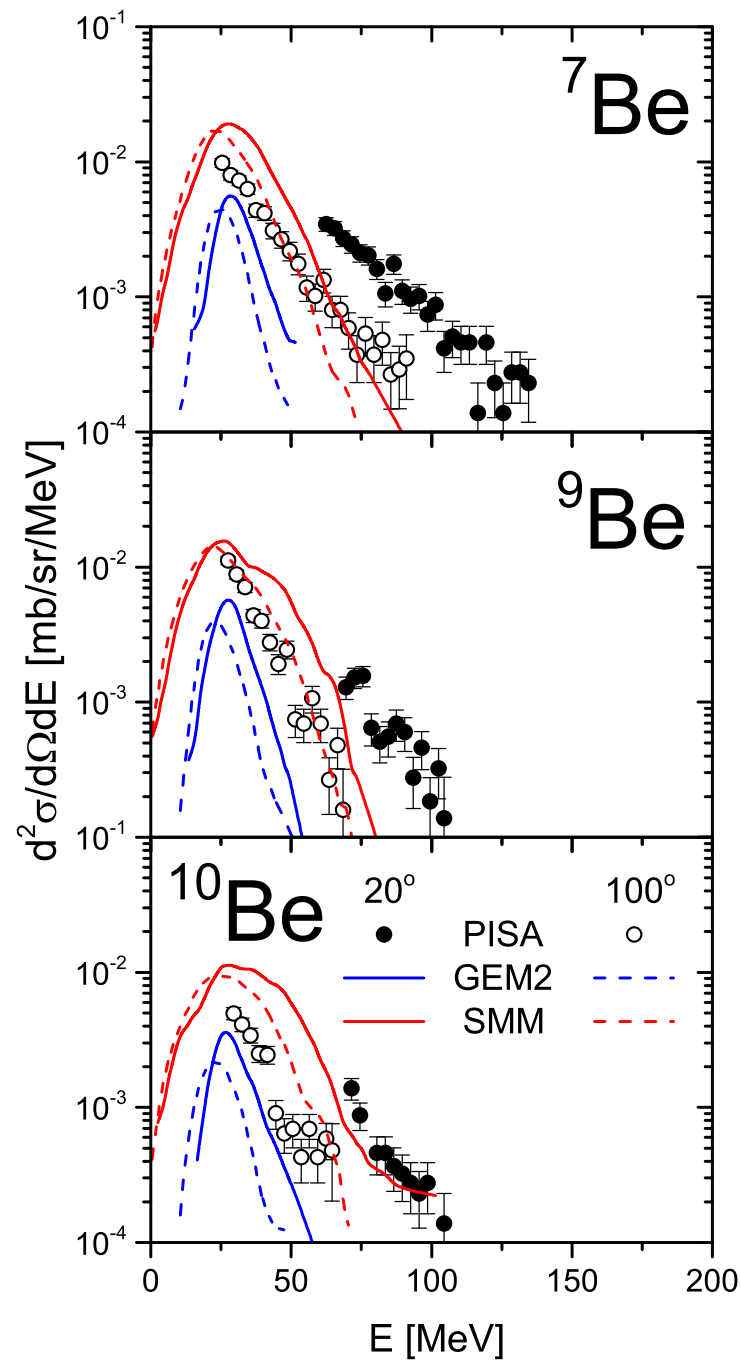


Figure 5.7. The same as in fig. 5.6, but for beryllium isotopes.

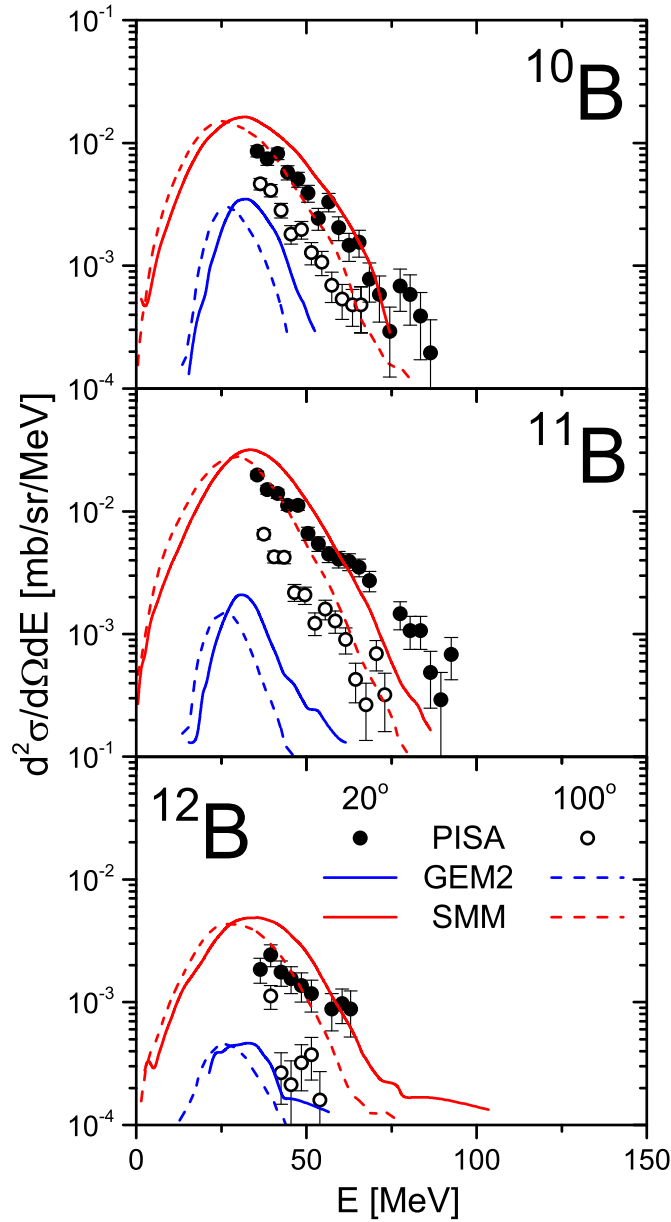


Figure 5.8. The same as in fig. 5.6, but for boron isotopes. The spectra at angle  $35^\circ$  are shown instead of those at  $20^\circ$ .

#### 5.3.4. Beam energy dependence of intermediate mass fragment emission

In the current subsection the variation of the IMF cross sections with the beam energy is presented. The IMF data measured at the angle  $65^\circ$  for two proton beam energies 1.2 GeV and 2.5 GeV are used as examples. The experimental and theoretical spectra for lithium, beryllium, and boron isotopes are shown in figs. 5.9, 5.10, and 5.11, respectively. The data measured at 2.5 GeV are represented by full dots whereas those at 1.2 GeV by open dots. The results of calculations are depicted as solid lines for the higher energy and as dashed lines for the lower one. The GEM2 calculations are represented by blue lines whereas the SMM results by red lines.

The energy dependence of IMF data is very similar to that observed for LCP cross sections. The shape of the spectra does not change with the beam energy but the absolute value of the cross sections increases. This effect observed in the data is well reproduced by both theoretical models. The SMM model produces the cross sections of almost the same magnitude as the data at small energies of IMF ( $E < 50$  MeV) however underestimates the high energy tail. The GEM2 model, on the other hand, systematically underestimates the data.

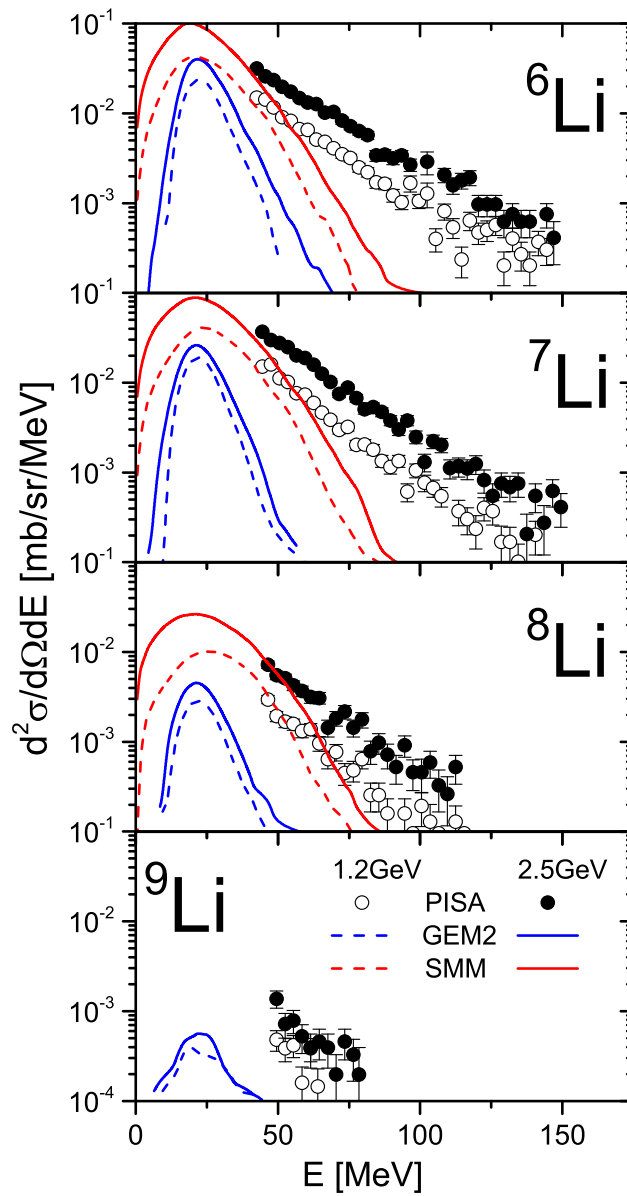


Figure 5.9. Comparison of the double differential cross sections  $\frac{d^2\sigma}{dE d\Omega}$  calculated by various models of the second stage of the reaction with the experimental data for lithium isotopes. Full and open dots represent the experimental data measured for detection angle  $65^\circ$  at 2.5 GeV and 1.2 GeV, respectively. Solid and dashed lines depict results of calculations performed for the proton beam energies 2.5 GeV and 1.2 GeV whereas the colors: blue and red indicate calculations for GEM2 and SMM model, respectively.

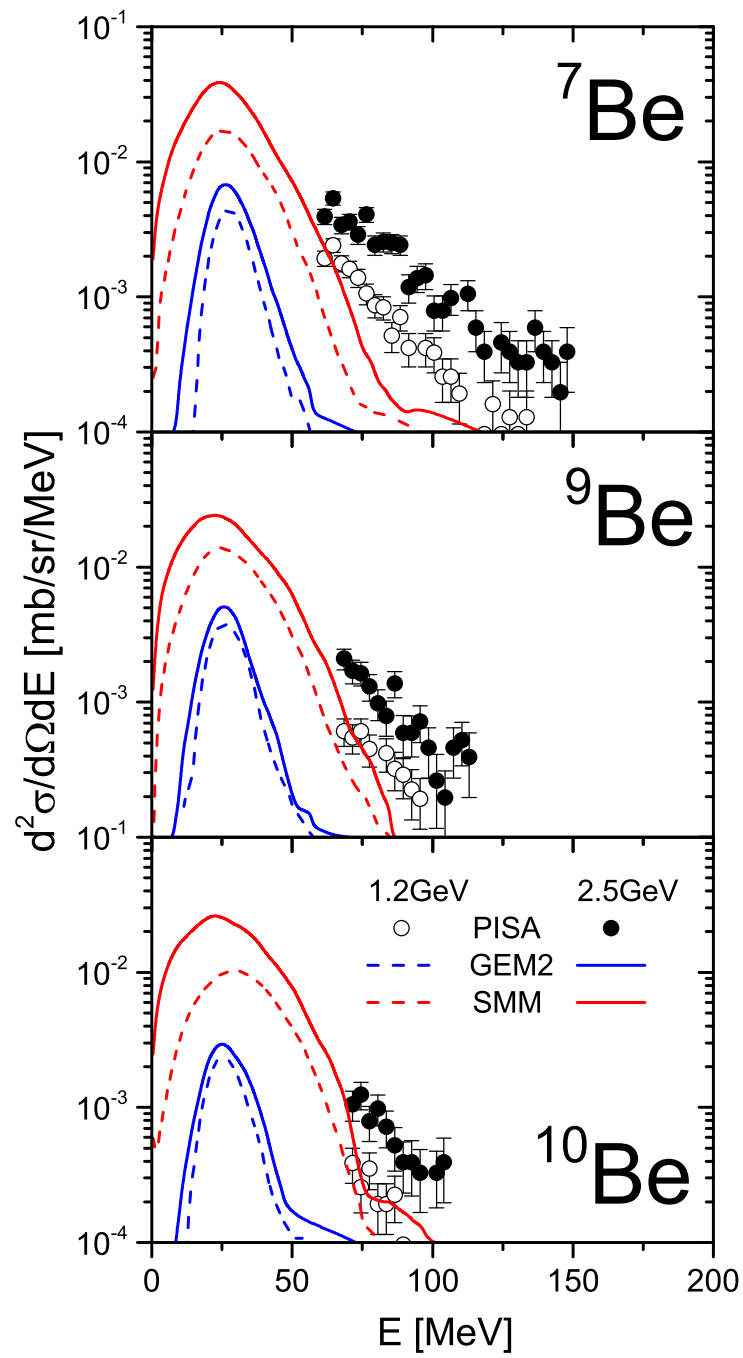


Figure 5.10. The same as in fig. 5.9, but for Be isotopes.

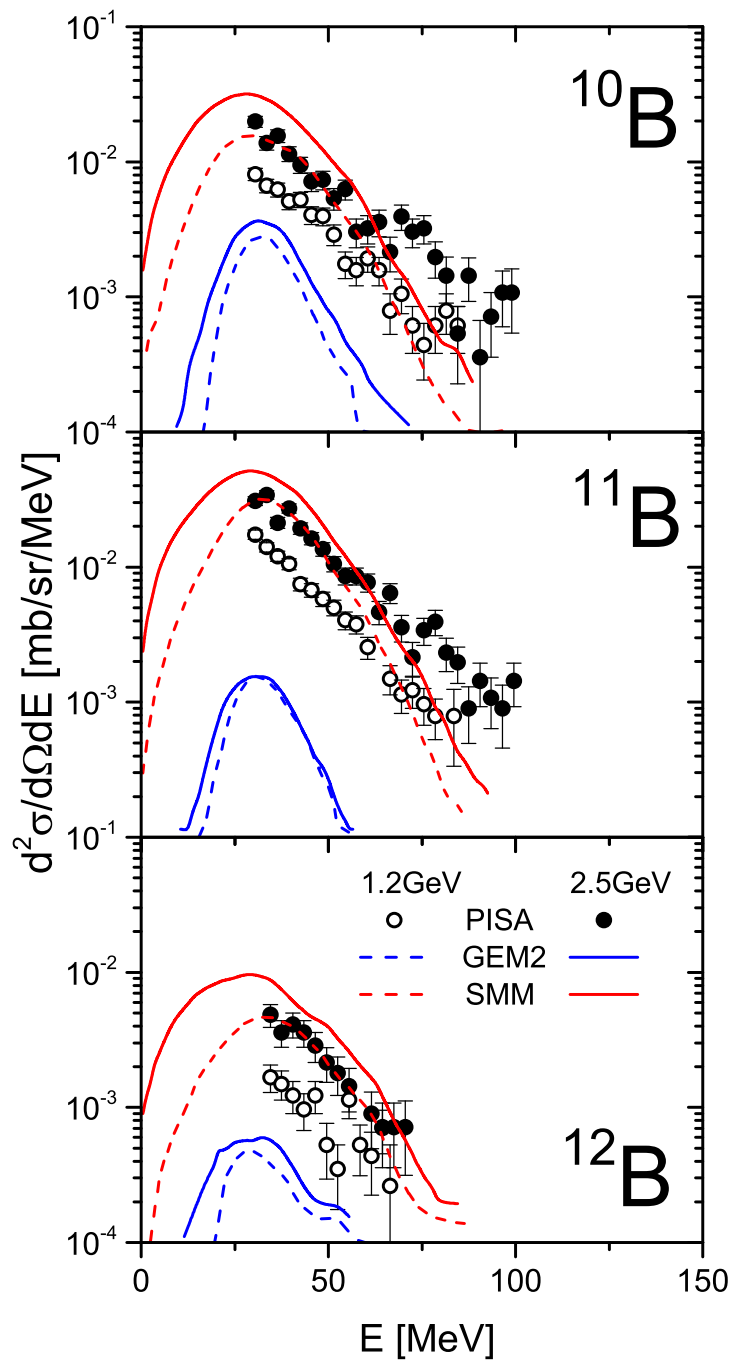


Figure 5.11. The same as in fig. 5.9, but for boron isotopes. Data and results from for  $50^\circ$  are used.

## Chapter 6

# The phenomenological model

Results of the current experiment show that double differential cross sections for production of LCP and IMF change smoothly with the scattering angle and fragment energy. The presence of different angular dependence of the spectra measured for small- and high-energy regions of emitted particles suggests that they correspond to the emission from two different sources. Following this suggestion the double differential cross sections of proton induced reactions were frequently parameterized as result of the emission of particles from two isotropically emitting sources moving along the direction of the beam. Such a description of the spectra was used successfully in previous studies of proton induced reactions on Ni and Au target nuclei: Ni [8, 65], Au [8, 66] at the same proton beam energies as in the present investigations.

This approach has the following physical interpretation. An impinging proton knocks out a group of nucleons during its way through the atomic nucleus. In such a collision two groups of nucleons are formed. The first of them - the group of knocked out nucleons, called „fireball”, is moving much faster than the second one which has the shape of a ball with the cylinder-like hole. Both groups form atomic nuclei which are excited and able to emit particles. Due to the size limitations arising from the geometrical dimensions of the interaction volume of the impinging proton with the target the „fireball” consists of only several nucleons. Therefore, the emission from the „fireball” is restricted to nucleons and LCPs. Such a limitation is not so restrictive for the heavier group of nucleons. Therefore it can emit LCP and IMF but it may also break up into more than two (excited) nuclei which in turn can be sources of particles. Such an interpretation allows for the interpolation and extrapolation of measured data by simple phenomenological model of two or more moving sources. This model is described in detail in the appendix A. The parameter of the model can be used to calculate total production cross sections as well as energy and angular distributions of particles. Thus, the model may serve as a simple parametrization of the data and can also put constraints to the existing microscopic models.

As it was shown in the previous chapters, the microscopic two-step description of the experimental data by INCL4.3 plus GEM2 or SMM is not sufficient. There is clearly visible that high energy tail of the IMF’s spectra is not well described. It is also the case for the middle part of LCP’s spectra, i.e. the ejectile energy range between 35 and 150 MeV.

It is important to emphasize that, the INCL model with the coalescence describes well the high energy part of spectra of light charged particles. This suggests that similar effect might be responsible for high energy spectra of intermediate mass fragments. The present version of the INCL model, i.e. the INCL4.3, does not allow to calculate the emission of complex fragments heavier than  $^4\text{He}$ , thus it was

not possible to check this hypothesis. The newer version of the intranuclear cascade model (INCL4.6 [6]) enables one to calculate the coalescence of nucleons into heavier fragments (with mass number  $A < 9$ ), however, it was found [7] that this model does not reproduce well the IMF spectra from p+Ag collisions.

Thus instead using the microscopic model it was decided to perform the analysis, which allows to take into account a possibility to emit particles from additional sources with their properties (the velocity, temperature and yield) treated as the parameters of the fit. Such a procedure was successfully applied in refs. [8, 65, 66]:

- ◇ To reproduce the LCP data the phenomenological contribution from single moving source was added to microscopic model cross sections calculated by INCL4.3 for the first stage of the reaction and GEM2 for the second stage. Since adding the phenomenological contribution would influence the total reaction cross section the microscopic model cross sections were multiplied by the factor smaller than unity. This factor as well as parameters of the moving source were fitted to reproduce well the data.
- ◇ The IMF spectra were described by sum of contributions from two moving sources which parameters were fitted to the data.

The method of analysis presented to above delivers values of parameters which can be easily compared with those obtained in the papers of A. Budzanowski et al. [8, 65, 66] for light (nickel) [65] and heavy (gold) [66] targets. Results of such an analysis for the lightest nuclei (Al and C targets) are also available in the PhD thesis of M. Fidelus [67]. The silver nucleus used in the present study is roughly twice heavier than the nickel nucleus and twice lighter than the gold nucleus. Thus the analysis of the present data can serve as a test for variation of the parameters of the phenomenological model. The systematic (monotonic) variation may be treated as indication of consistency of the postulated reaction mechanism model.

The parameters of the phenomenological models were searched by fitting simultaneously the model predictions to the data at all accessible angles independently for each ejectile.

### The moving source model for LCP data

For the LCP, the combination of microscopic models and phenomenological contribution has been applied. The result of the INCL4.3+GEM2 calculations were scaled down by factor  $F$  and added to the contribution emerging from the single moving source. The  $F$  factor as well as properties of the source were treated as free parameters. The  $F$  parameter found for proton data were further fixed and used as a constant for all other LCP for given beam energy. This is marked in the table 6.1 by taking fixed  $F$  value into the square brackets. The results of the fit was almost independent of the parameter  $k$  value (reduced height of the Coulomb barrier for emitted fragments), thus it was arbitrary fixed at 0.02, for all calculations.

The values of the parameters are presented in the table 6.1. The physical interpretation of the parameters is as follows (see Appendix A):

- ◇  $\beta$  - represents LAB velocity of the emitting source in the  $c$  units.
- ◇  $T$  - corresponds to the apparent temperature of the source in MeV,
- ◇  $\sigma$  - depicts the total cross section for emission of given particle from moving source in mb,
- ◇  $kB/d$  - the ratio of the effective Coulomb barrier to its diffusion (cf. Appendix A)
- ◇  $F$  - factor scaling down the microscopic calculation of INCL4.3+GEM2

Table 6.1. Values of the parameters used to fit the INCL4.3+GEM2 and single moving source contributions to the LCP data for three beam energies listed in the  $E_p$  column.

$E_p$ GeV	Ejectile	$\beta$	T [MeV]	$\sigma$ [mb]	B/d	F	$\chi^2$
1.2	p	0.132	39.9	1562	9.8	0.656	356.5
	d	0.092	32.9	280	1.8	[0.656]	23.9
	t	0.038	17.5	111	10.8	[0.656]	10.0
	$^3\text{He}$	0.052	23.3	32	11.6	[0.656]	5.6
	$^4\text{He}$	0.057(6)	22.0(1.3)	62(9)	2.7(3)	[0.656]	37.7
1.9	p	0.1456	41.5	1892	9.0	0.694	243.2
	d	0.0937	35.5	386	3.2	[0.694]	23.1
	t	0.0365	19.0	174	2.2	[0.694]	9.9
	$^3\text{He}$	0.0524	25.6	56	9.5	[0.694]	6.0
	$^4\text{He}$	0.048(4)	22.0(9)	108(11)	2.2(2)	[0.694]	19.4
2.5	p	0.1427	43.3	2306	4.1	0.727	148.1
	d	0.0886	37.4	510	3.6	[0.727]	17.4
	t	0.0359	20.5	233	3.4	[0.727]	8.95
	$^3\text{He}$	0.0469	27.5	84	5.9	[0.727]	5.3
	$^4\text{He}$	0.045(3)	22.2(8)	108(11)	2.1(3)	[0.727]	16.6

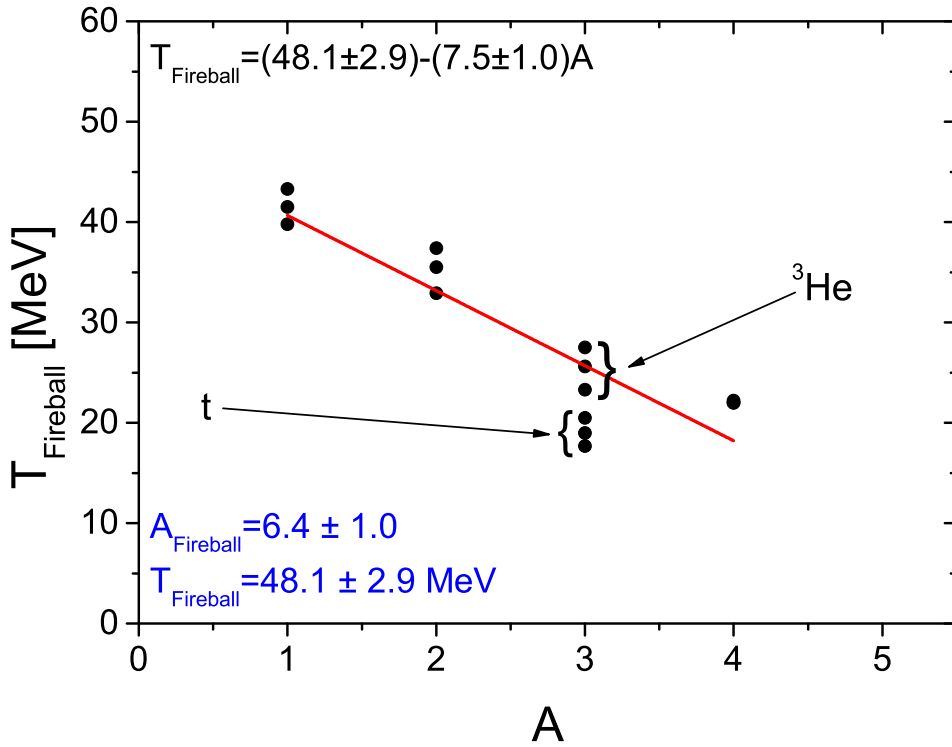


Figure 6.1. The figure presents the values of the temperature parameter obtained from the fits as a function of mass of ejectiles. The circles depict the temperature values found for different beam energies (1.2 GeV, 1.9 GeV, and 2.5 GeV). Red line presents linear fit to the points.

Results of the calculations are presented in fig. 6.2 for hydrogen isotopes and in fig. 6.3 for helium isotopes. The scaled down microscopic model contribution is depicted by the red line, the moving source contribution by the blue line and their sum by the black line. As can be seen in the figures the agreement of theoretical lines with the data shown as open circles is very good for all LCP. Significant improvement of the data description in comparison to that obtained by microscopic model itself is clearly visible (cf. figs. 5.1, and 5.2 with 6.2, and 6.3). It is worth to notice that the obtained improvement was achieved with very smoothly varying parameters versus mass of the ejectiles as well as versus the beam energy. For example the scaling factor  $F$  for the microscopic model changes from 0.656 to 0.727 when the beam energy increases more than twice (from 1.2 to 2.5 GeV). Similar variation of other parameters with the energy is also visible.

The variation of apparent temperature parameter  $T$  with the mass of ejectile may be used to estimate the mass and temperature of the emitting source (see the formulae given in the Appendix A.3). This dependence is shown in fig. 6.1 where the mass dependence of the temperature parameter is shown for three beam energies. As can be seen the mass dependence is practically the same for all three beam energies and may be well approximated by the straight line:

$$T = [-7.5(1.0)A_{LCP} + 48.1(2.9)] \text{ MeV} \quad (6.1)$$

The parameters of the straight line listed above can be transformed to the mass of the fireball and its temperature:

$$\tau_{Fireball} = 48.1(2.9) \text{ MeV} \quad (6.2)$$

$$A_{Fireball} = 6.4(1.0) \quad (6.3)$$

The coalescence model included in the INCL4.3 code calculates the emitting fragments up to the  ${}^4\text{He}$ , thus the data for  ${}^6\text{He}$  were treated in the same way like the data for intermediate mass fragments, ie.: two moving sources were fitted.

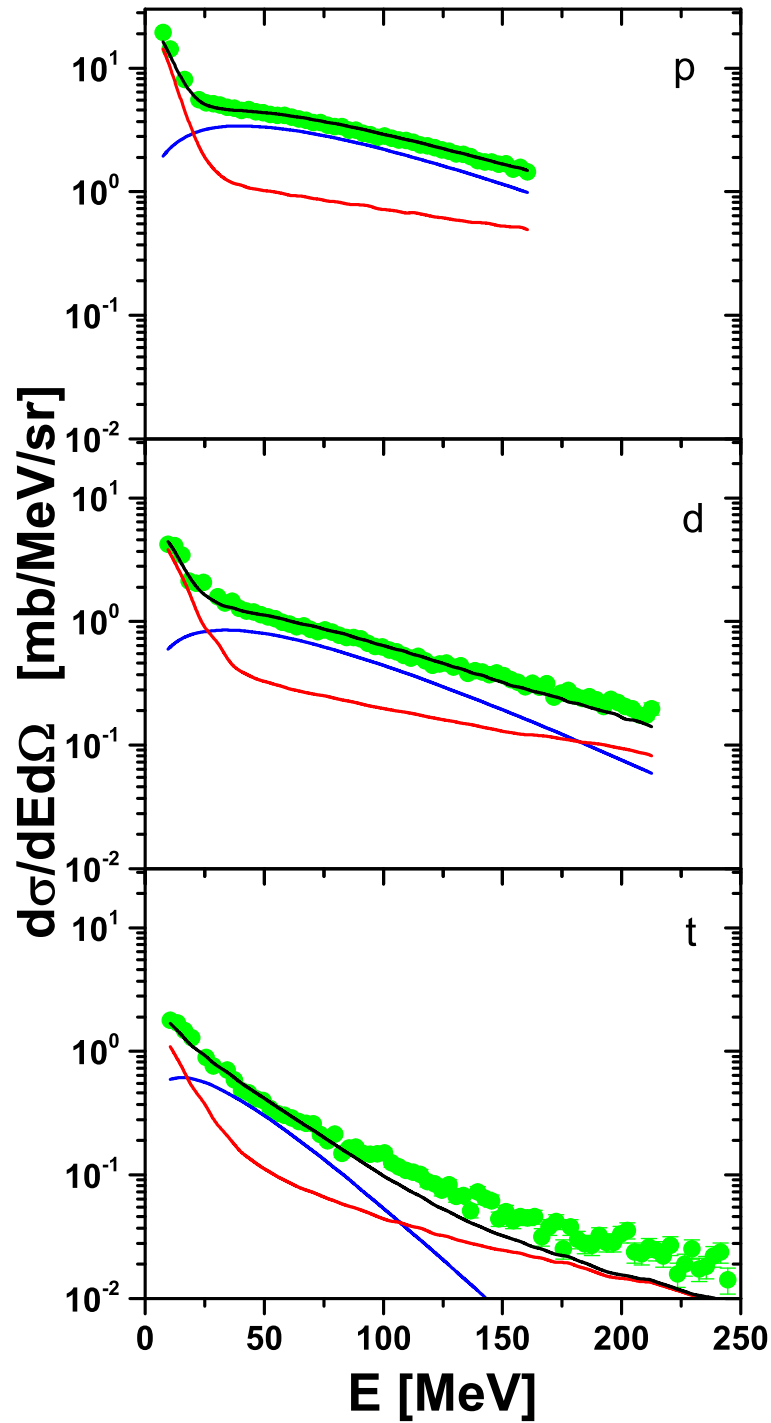


Figure 6.2. The figure presents experimental data (represented by green points) of double differential cross sections  $\frac{d\sigma}{dEd\Omega}$  for hydrogen isotopes registered at the angle  $20^\circ$  in reaction with 2.5 GeV of proton beam energy on silver target. Fits of the moving source are presented by the blue lines, while the calculations of the two steps model INCL4.3+GEM2 are depicted by the red lines. The black line depicts sum of both contributions.

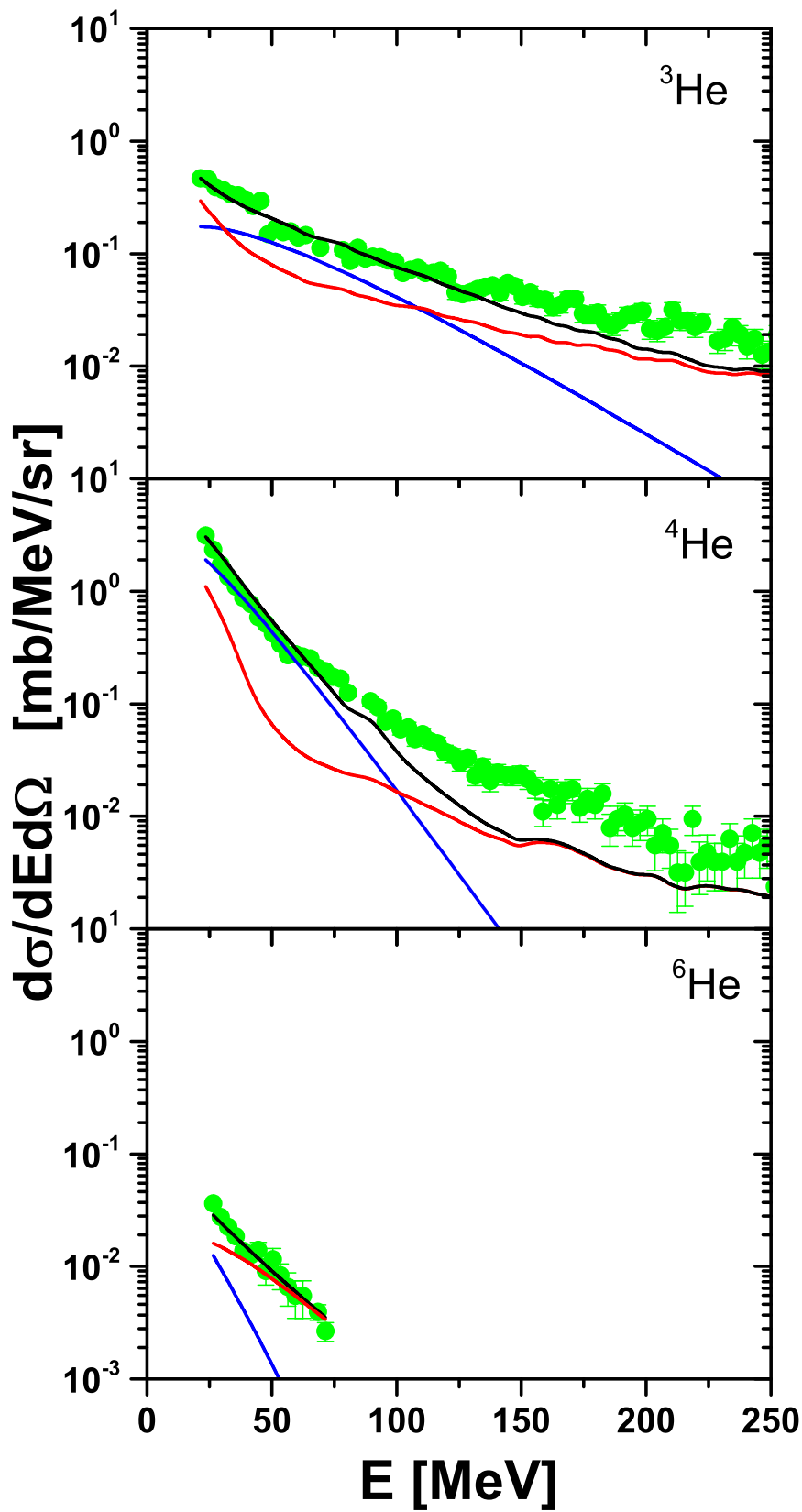


Figure 6.3. The same as in fig. 6.2, but for helium isotopes. Two moving source model was fitted to the  ${}^6\text{He}$  data, both sources are presented in the figure (blue and red lines).

The approach with adding a fast moving source gives good description of the experimental data. Such a procedure allows to reproduce the emission particles with mass up to  $A=4$ .

Moreover the parameters obtained during the analysis enable us to determine relative contribution of emission of LCP from the fireball. It was shown in the table 6.2 that the production of the hydrogen isotopes, as well as the  $^3\text{He}$  from fireball is significant. For alpha particles emission from fireball corresponds to only  $\sim 15\%$  of total cross section.

Table 6.2. Averaged over beam energy and the atomic number the relative contribution to the LCP production cross sections of the emission from the fireball in reactions induced by protons on a silver target.

A LCP mass number	Relative yield of emission [%] from fireball
1	$39 \pm 2$
2	$35 \pm 3$
3	$41 \pm 4$
4	$15 \pm 2$

## Application of the phenomenological model to the IMF

As it was mentioned, present experimental data of intermediate mass fragments emitted were analyzed by applying two moving source approach. In figures 6.4, 6.5, 6.6 a typical example of performed fits to the collected data is presented, for the scattering angle  $50^\circ$  and for 2.5 GeV of the proton beam energy. The black line presents the sum of contributions from both fitted sources, while the red and blue lines depict results obtained for each source.

The very good description of the spectra of all intermediate mass fragments has been obtained, as it is indicated by the  $\chi^2$  values. The complete set of the parameter values is presented in the tables 6.3 and 6.4.

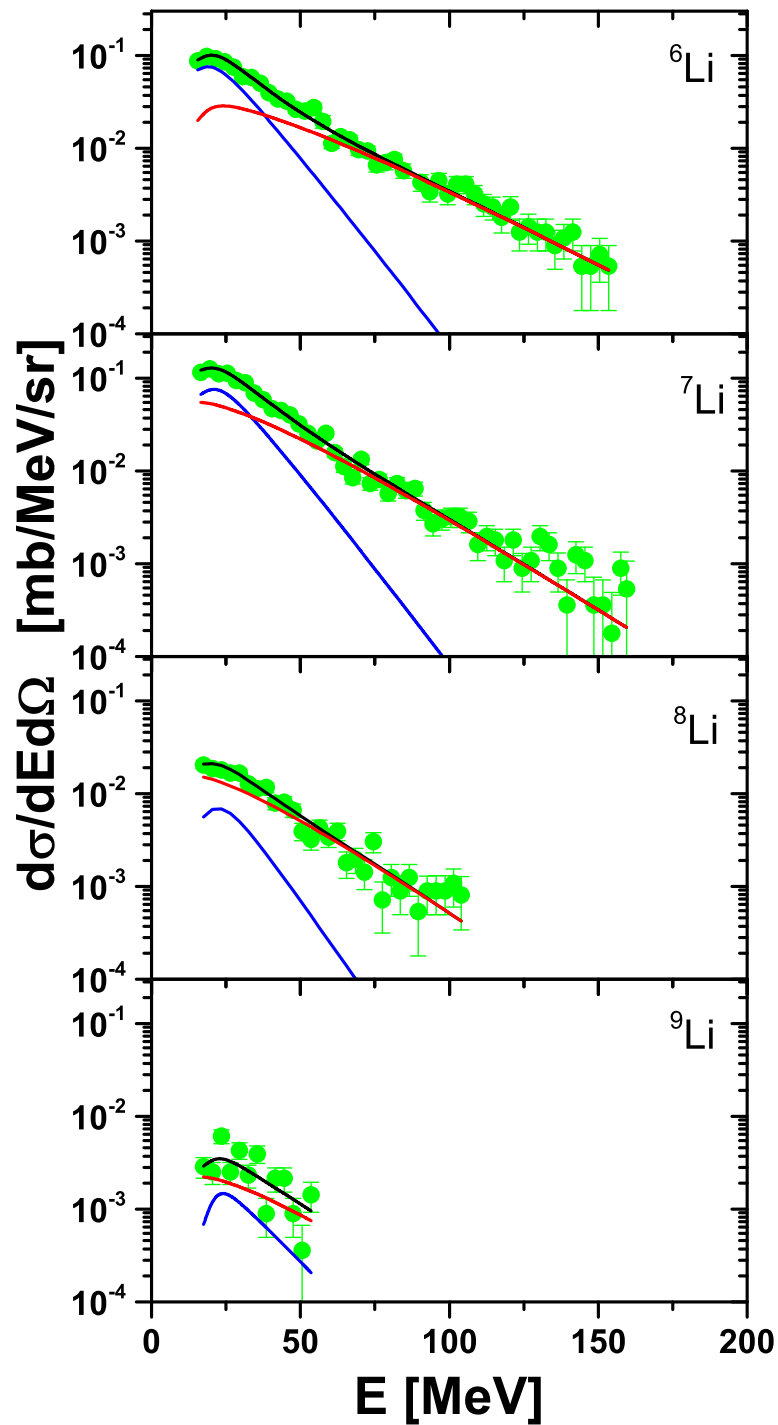


Figure 6.4. The figure presents experimental data of double differential cross sections  $\frac{d\sigma}{dEd\Omega}$  for lithium isotopes registered at the angle  $50^\circ$  from the reaction of 2.5 GeV protons with a silver target (points). Fits of two moving sources are also presented with indication of the contribution of each source. The blue lines depict the „slow” source, while the red lines represent the „fast” source. Black lines show the sum of both contributions.

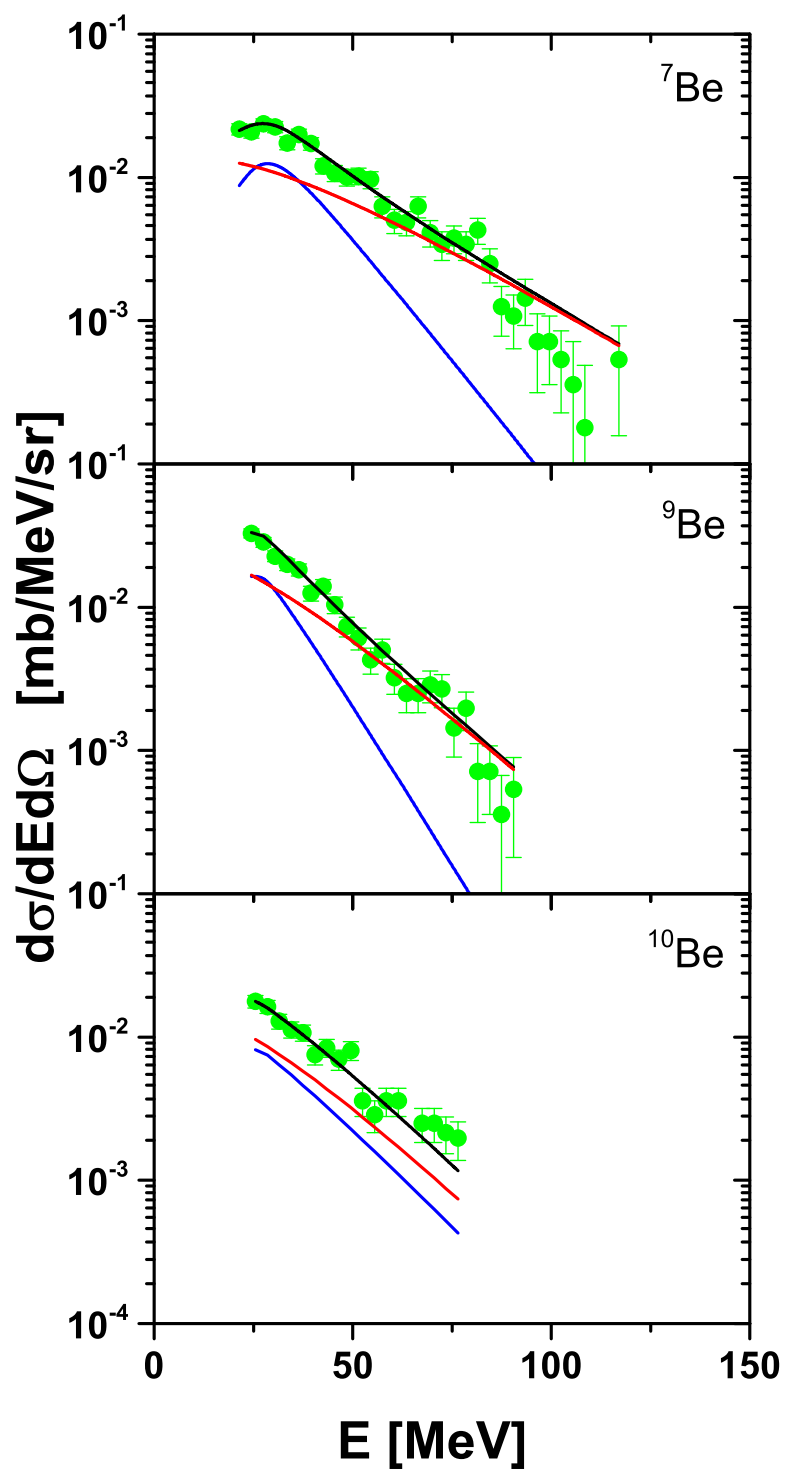


Figure 6.5. The same as in fig 6.4 but for beryllium isotopes.

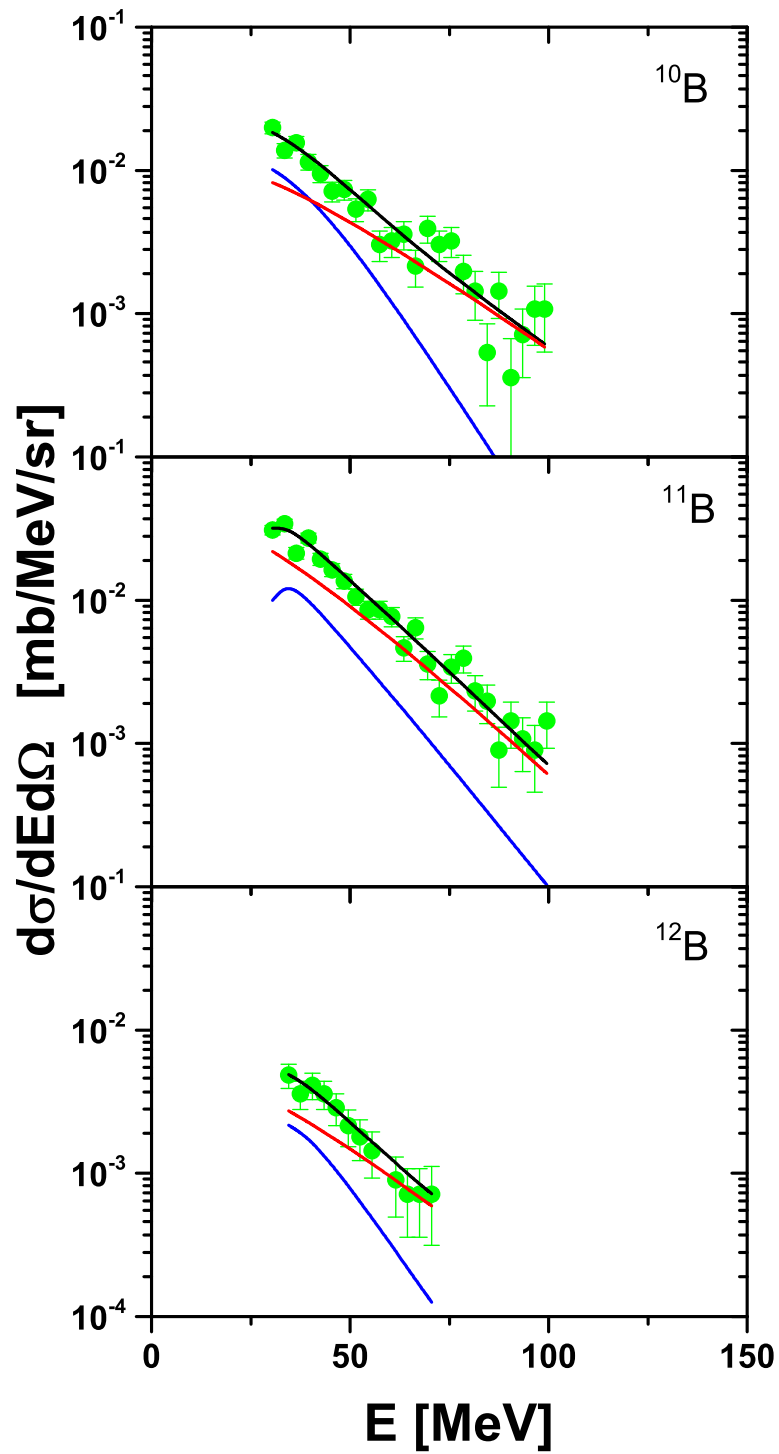


Figure 6.6. The same as in fig 6.4, but for boron isotopes.

Table 6.3. Parameters of two moving sources for isotopically identified intermediate mass fragments. Index „1” corresponds to the „slow” moving source, while index „2” indicates parameters for the „fast” moving source. The rows for given ejectile correspond to proton beam energy 1.2, 1.9 and 2.5 GeV, respectively. The values of the velocity  $\beta_1$  of the „slow” sources are fixed at a values: 0.0036c, 0.0029c and 0.0025c for beam energy 1.2, 1.9 and 2.5 GeV, respectively. They were estimated as velocity of the heavy remnant from the BUU model calculation performed by A. Kowalczyk [68]. (part I)

Ejectile	$k_1$	$T_1$ MeV	$\sigma_1$ mb	$k_2$	$\beta_2$	$T_2$ MeV	$\sigma_2$ mb	B/d	$\chi^2$
${}^6\text{He}$	[0.72]	$9.1 \pm 0.5$	$4.0 \pm 0.5$	[0.42]	$0.034 \pm 0.005$	$14.8 \pm 0.5$	$2.2 \pm 0.5$	$4.4 \pm 1.0$	2.00
	[0.72]	$8.9 \pm 0.7$	$5.3 \pm 0.8$	$0.41 \pm 0.06$	$0.028 \pm 0.004$	$15.7 \pm 0.5$	$4.4 \pm 0.8$	$3.3 \pm 0.7$	1.41
	[0.72]	$9.1 \pm 0.9$	$6.6 \pm 1.2$	$0.42 \pm 0.08$	$0.027 \pm 0.005$	$17.5 \pm 0.9$	$5.3 \pm 1.2$	$4.0 \pm 1.0$	1.56
${}^6\text{Li}$	$0.81 \pm 0.01$	$9.0 \pm 0.3$	$10.0 \pm 0.5$	[0.3]	$0.0342 \pm 0.0015$	$19.9 \pm 0.3$	$6.9 \pm 0.5$	$8.2 \pm 0.8$	1.37
	$0.75 \pm 0.03$	$9.9 \pm 0.4$	$16.7 \pm 0.9$	$0.34 \pm 0.06$	$0.0319 \pm 0.0016$	$21.8 \pm 0.3$	$10.3 \pm 0.7$	$5.6 \pm 1.0$	1.47
	$0.72 \pm 0.04$	$9.8 \pm 0.5$	$23.5 \pm 1.4$	$0.43 \pm 0.05$	$0.0302 \pm 0.0017$	$22.6 \pm 0.4$	$13.0 \pm 0.9$	$3.6 \pm 0.6$	1.17
${}^7\text{Li}$	0.88	8.2	9.0	0.27	0.0252	16.3	11.3	8.4	1.73
	$0.88 \pm 0.04$	$8.8 \pm 0.6$	$15.4 \pm 1.5$	[0.3]	$0.0227 \pm 0.0012$	$17.7 \pm 0.2$	$19.0 \pm 1.5$	$5.4 \pm 0.8$	1.76
	$0.83 \pm 0.05$	$9.8 \pm 0.6$	$23.6 \pm 2.4$	[0.3]	$0.0244 \pm 0.0016$	$18.9 \pm 0.3$	$20.4 \pm 2.0$	$4.4 \pm 0.9$	1.68
${}^8\text{Li}$	[1.0]	7.2	0.62	0.30	0.0221	14.5	2.6	12.7	1.17
	0.99	7.5	1.25	0.32	0.0207	16.4	4.1	6.6	1.08
	[0.95]	8.7	2.0	0.29	0.0209	17.1	5.2	5.2	1.24
${}^9\text{Li}$	[0.95]	12.5	0.002	[0.3]	0.0127	15.6	0.652	[8.3]	1.58
	[0.95]	9.5	0.13	0.36	0.0197	16.7	0.90	15.6	1.47
	[0.95]	$11.5 \pm 3.0$	$0.42 \pm 0.15$	[0.36]	$0.0341 \pm 0.0068$	$16.4 \pm 2.1$	$0.64 \pm 0.22$	[9.0]	1.56

Table 6.4. Continuation of the Table 6.3 for Be and B isotopes.

Ejectile	$k_1$	$T_1$ MeV	$\sigma_1$ mb	$k_2$	$\beta_2$	$T_2$ MeV	$\sigma_2$ mb	B/d	$\chi^2$
${}^7\text{Be}$	0.87	11.3	1.46	0.27	0.0297	18.9	2.77	11.0	0.94
	0.84	11.4	3.3	0.25	0.0306	21.0	4.2	6.7	1.03
	0.90	11.6	4.3	0.25	0.0293	21.8	5.4	6.1	1.21
${}^9\text{Be}$	0.89	8.5	1.8	0.28	0.0201	13.6	2.8	21.1	1.28
	0.88	9.7	2.4	0.23	0.0190	15.1	5.2	20.5	1.33
	0.85	9.0	3.6	0.30	0.0196	15.5	5.6	12.3	1.50
${}^{10}\text{Be}$	0.76	9.8	1.36	0.32	0.0312	13.2	0.99	19.8	1.00
	[0.88]	11.1	2.9	[0.23]	0.0265	13.0	2.5	2.7	1.06
	0.91	12.1	1.3	0.29	0.0183	14.9	3.9	37.6	1.05
${}^{10}\text{B}$	[0.84]	9.9	2.4	0.30	0.0283	17.4	0.86	4.7	1.19
	[0.84]	10.7	4.1	[0.28]	0.0259	17.3	1.9	4.1	0.96
	0.84	11.6	2.6	0.22	0.0214	18.6	3.7	13.9	1.48
${}^{11}\text{B}$	[0.94]	[6.5]	0.82	0.44	0.0183	12.7	4.4	9.2	1.17
	[0.94]	8.2	1.6	0.24	0.0168	13.3	11.3	[6.0]	1.05
	0.94	11.7	3.4	0.19	0.0237	14.3	9.4	13.3	1.05
${}^{12}\text{B}$	$0.96 \pm 0.23$	$8.5 \pm 3.2$	$0.27 \pm 0.11$	$0.28 \pm 0.38$	$0.069 \pm 0.033$	$19.5 \pm 9.2$	$0.25 \pm 0.28$	[10.0]	1.15
	[0.94]	10.7	0.84	[0.23]	0.45	13.8	0.38	52.8	0.79
	[0.94]	10.0	0.80	[0.19]	0.0221	16.2	1.4	6.0	0.78

## Chapter 7

# Comparison of present results with those for Ni and Au targets

The results of the present phenomenological analysis are compared in this chapter with those published in the literature for Ni and Au targets at the same proton beam energies [8, 66]. To assure that the comparison of the present and literature results is meaningful the same procedure has been used as that applied in the literature to extract values of the model parameters, i.e. the apparent temperature  $T$ , the velocity  $\beta$  of the source and the absolute yield of each source  $\sigma$ . It was shown in the previous chapter, that it is possible to obtain a good agreement between the IMF data and a simple phenomenological description, which assumes that the particles are emitted isotropically from two sources moving along the beam direction. Equally good description was obtained for LCP, where contribution to the cross sections from one of these sources was replaced by the results of calculations within the intranuclear cascade INCL4.3 scaled down by factor  $\sim 0.7$  to make room for the contribution from the second moving source - called „the fireball”. The properties of the slow source fitted to the IMF data are discussed in the following section whereas those for the fast source are presented in the next section.

### 7.1. Properties of the slow source

The INCL4.3 calculations scaled down by a factor adjusted to proton data have been used for the LCP data (p,d,t, $^3\text{He}$ , and  $^4\text{He}$ ) instead fitting the slow source contribution. Values of the scaling factor  $F$  used in the calculations are shown in table 7.1. The factor  $F$  was fitted together with parameters of the fast source for the proton cross sections and was kept constant for other data. As can be seen values of the  $F$  factor are almost the same for all targets and energies (with slight monotonic increase with the proton beam energy) what means that the relative contribution of the fast source is almost the same in all cases and is equal to about 30 % of the total yield.

Table 7.1. The scaling factor  $F$  used in the description of LCP data by a sum of scaled down INCL4.3 + GEM2 cross sections and a fast source contribution. The symbol  $E_p$  represents value of the incident proton beam energy. The results for Ni and Au targets were taken from refs. [66] and [8], respectively whereas those for Ag target were obtained in the present work.

$E_p$ (GeV)	Target		
	Ni	Ag	Au
1.2	0.70	0.66	0.63
1.9	0.70	0.69	0.69
2.5	0.79	0.73	0.73

It was found that the velocity of the slow source and its temperature almost do not change in the fits performed to the cross sections of different IMF. Furthermore the fitted velocity of this source was very close to velocity of the residual nuclei after intranuclear cascade. Thus the velocity of the slow source was fixed for all IMF at the average velocity of the residual nuclei of the intranuclear cascade. The values of velocities of the slow source are listed in table 7.2. They cover the range from 0.0025 to 0.0051 what proofs the statement that the source is „slow”.

Table 7.2. The velocity  $\beta$  (in units of the speed of light) of the slow source used in the description of the IMF data. Its value was fixed at the average velocity of residual nuclei after the first, fast stage of the reaction. The symbol  $E_p$  represents value of the proton beam energy. The results for Ni and Au targets were taken from refs. [66] and [8], respectively whereas those for Ag target were used in the present work.

$E_p$ (GeV)	Target		
	Ni	Ag	Au
1.2	0.0051	0.0036	0.0030
1.9	0.0049	0.0029	0.0030
2.5	0.0047	0.0025	0.0030

It turned out that the temperature of the slow source was independent of the mass of IMF therefore only the average (over IMF) value of the temperature is presented in table 7.3. The standard deviation of the temperature (given in parenthesis) allows to judge the spread of temperatures for individual IMF. The temperature values do not change with the beam energy and differ only slightly for different targets.

Table 7.3. The apparent temperature parameter T (in MeV) of the slow source used in the description of the IMF data. Its value was averaged over all IMF. The symbol  $E_p$  represents value of the proton beam energy. The results for Ni and Au targets were taken from refs. [66] and [8], respectively whereas those for Ag target were obtained in the present work.

$E_p$ (GeV)	Target		
	Ni	Ag	Au
1.2	8.1(1.1)	9.1(1.7)	11.5(1.2)
1.9	9.2(1.0)	9.7(1.2)	10.8(1.7)
2.5	8.8(1.8)	10.4(1.3)	10.6(1.1)

As it was stated in chapter 2 many authors observed the „power-law” 2.1 dependence of the yield of IMF on the mass number  $A_F$ :

$$\sigma(A_F) \propto (A_F)^{-\tau}.$$

The large spread of absolute yields for different IMF in the mass range studied in the present work, i.e.  $A_F = 6 - 12$ , makes inaccurate extraction of the parameter  $\tau$ . Nevertheless similar values of this parameter were observed for Ni and Au data and for the present Ag data. Values of the parameter were extracted from a linear fit to the dependence of the logarithm of the cross section on the logarithm of the mass of the ejectiles. They are collected in table 7.4.

Table 7.4. The parameter  $\tau$  of the „power-law” dependence of the yields of IMF (the  $\sigma$  parameter of the slow source) on the mass of the ejectiles. The symbol  $E_p$  represents value of the proton beam energy. The results for Ni and Au targets were taken from refs. [66] and [8], respectively whereas those for Ag target were obtained in the present work.

$E_p$ (GeV)	Target		
	Ni	Ag	Au
1.2	2.1(2.0)	3.5(1.1)	2.0(1.2)
1.9	2.6(1.7)	3.3(1.6)	2.2(1.2)
2.5	1.8(1.2)	3.7(1.2)	2.5(1.3)

The values of the  $\tau$  parameter are equal in the limits of errors for all investigated targets (Ni, Ag, Au) and all impinging proton energies from 1.2 GeV to 2.5 GeV. This is also the case for the temperature and the velocity parameters. Therefore it suggests that the mechanism of the reaction responsible for the emission of particles from an equilibrated nucleus, is the same. From inspection of figures 6.4, 6.5, and 6.6 it is evident that the slow source contributes mainly to low energy part of spectra (ejectile energies smaller than  $\approx 50$  MeV). The same energy region is well described by SMM model as it is visible in figs. 5.6, 5.7, and 5.8. Thus it may be conjectured that the competition of evaporation and multifragmentation is responsible for the emission mechanism.

## 7.2. Properties of the fast source

The high energy part of the experimental spectra could not be well reproduced by the slow source alone thus the second, fast source was added. It was found that parameter values of the fast source changed smoothly when treated as a function of the ejectile mass in spite of the fact that they have been fitted independently to data for each reaction channel. This will be discussed separately for each of the model parameters in the following subsections.

### 7.2.1. Apparent temperature parameter $T$

The energy and momentum conservation demands, as it was emphasized by Hirsch et al. [36], that the apparent temperature parameter  $T$  of the ejectiles emitted *from the same source* of the mass  $A_S$  and temperature  $\tau$  should follow the straight line as a function of the ejectile mass  $A_F$ :

$$T = \frac{A_S - A_F}{A_S} \tau. \quad (7.1)$$

The parameters  $a$  and  $b$  of the straight line :

$$T = aA_F + b \quad (7.2)$$

are then in the straightforward way connected to the mass of the source  $A_S$  and its temperature  $\tau$ :

$$\tau = b \quad (7.3)$$

$$A_S = -\frac{b}{a} \quad (7.4)$$

It was found in previous publications of the PISA collaboration [8, 66] that the temperature parameter decreases monotonically with the mass of detected particles. Since the slope of this function is almost the same for all LCP and for all IMF, but it differs between LCP and IMF the authors suggested that LCP and IMF particles originate from two different sources called „fireball” and „fast source”, respectively. The blue straight line shown in figures 7.1, 7.2 and 7.3 represents temperature dependence on the LCP mass whereas the green straight line represents this dependence for IMF. Parameters of the lines for all targets and beam energies are listed in the table 7.5 what allows to compare quantitatively properties of the corresponding sources. As can be seen the temperature  $\tau$  and the mass  $A_S$  of the source are approximately equal to  $\tau \sim 46$  MeV,  $A_S \sim 7$  for LCP and  $\tau \sim 24$  MeV,  $A_S \sim 28$  for IMF, respectively. It should be pointed out that very similar values were obtained for all targets taken into consideration i.e. Ni, Ag, and Au as well as for all studied proton incident beam energies; 1.2, 1.9, and 2.5 GeV.

Table 7.5. Parameters of the formula 7.2 which represents the dependence of the source temperature on the mass of emitted particles. The particles cover LCP and IMF (with mass number from  $A=6$  to  $A=12$ ) for all targets and energies. The quantities  $a$  and  $b$  are the parameters of the straight lines fitted to mentioned formula for T separately for LCP and for IMF. The symbol  $A_S$  represents the mass number and  $\tau$  the temperature of the source emitting LCP and IMF.

Target	$E_p$ GeV	LCP			IMF ( $A < 13$ )		
		a	$b = \tau$	$A_S$	a	$b = \tau$	$A_S$
Ni	1.2	-6.8(1.2)	44.9(3.4)	6.6(1.3)	-0.85(4)	21.2(4)	24.8(1.3)
	1.9	-6.8(1.2)	46.6(3.3)	6.9(1.3)	-0.89(4)	22.8(4)	25.6(1.3)
	2.5	-6.4(1.1)	46.3(3.0)	7.2(1.3)	-0.89(4)	24.1(4)	27.2(1.4)
Ag	1.2	-5.8(1.0)	42.8(2.7)	7.3(1.3)	-0.77(5)	22.3(5)	29.1(2.0)
	1.9	-6.4(1.1)	46.0(3.1)	7.2(1.3)	-0.82(5)	23.4(5)	28.4(2.0)
	2.5	-6.6(1.1)	48.1(2.9)	7.3(1.3)	-0.86(6)	24.7(5)	28.8(2.0)
Au	1.2	-6.5(1.1)	44.6(3.2)	6.9(1.3)	-0.83(4)	21.8(4)	26.4(1.4)
	1.9	-5.8(1.0)	45.8(2.7)	7.9(1.4)	-0.84(4)	25.7(3)	30.5(1.5)
	2.5	-6.7(1.1)	49.7(3.1)	7.4(1.3)	-0.92(4)	26.5(4)	28.7(1.4)

The close similarity of the source masses and temperatures for different beam energies as well as for different targets is still better visible in the table 7.6 where their values averaged over beam energy and over targets are presented.

Table 7.6. The source temperature  $\tau$  and source mass  $A_S$  averaged over energies and averaged over targets for light charged particles ( $\langle \tau_{LCP} \rangle, \langle A_{S_{LCP}} \rangle$  and for intermediate mass fragments ( $\langle \tau_{IMF} \rangle, \langle A_{S_{IMF}} \rangle$ ).

	$\langle \tau_{LCP} \rangle$	$\langle A_{S_{LCP}} \rangle$	$\langle \tau_{IMF} \rangle$	$\langle A_{S_{IMF}} \rangle$
Ni	46.0(1.9)	6.9(8)	22.7(2)	25.9(8)
Ag	45.5(1.7)	7.3(8)	23.5(3)	28.1(1.0)
Au	46.7(1.7)	7.4(8)	24.9(2)	28.5(8)
average	<b>46.0(1.0)</b>	<b>7.0(4)</b>	<b>23.8(1)</b>	<b>27.5(5)</b>

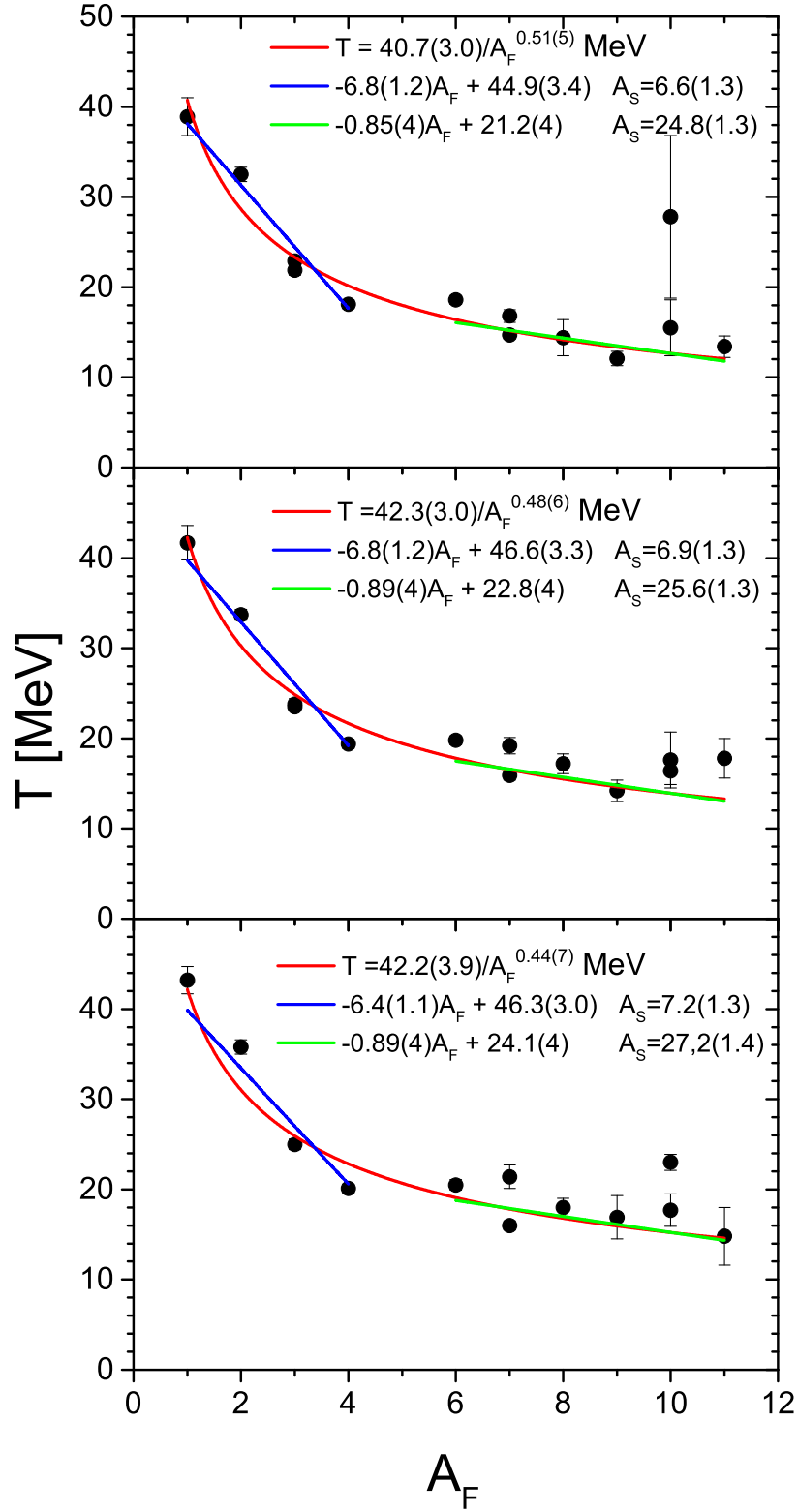


Figure 7.1. Ejectile mass number  $A_F$  dependence of  $T$  parameter representing the apparent temperature of the source which emits the particles in proton - Ni collisions at proton beam energy 1.2 GeV (upper panel), 1.9 GeV (middle panel) and 2.5 GeV (lower panel). The blue straight line is fitted for LCP whereas the green line for IMF ( $5 < A < 12$ ). The red line represents predictions of the formula 7.5 with parameters fitted for whole range of  $A_F$  values (it will be discussed further below).

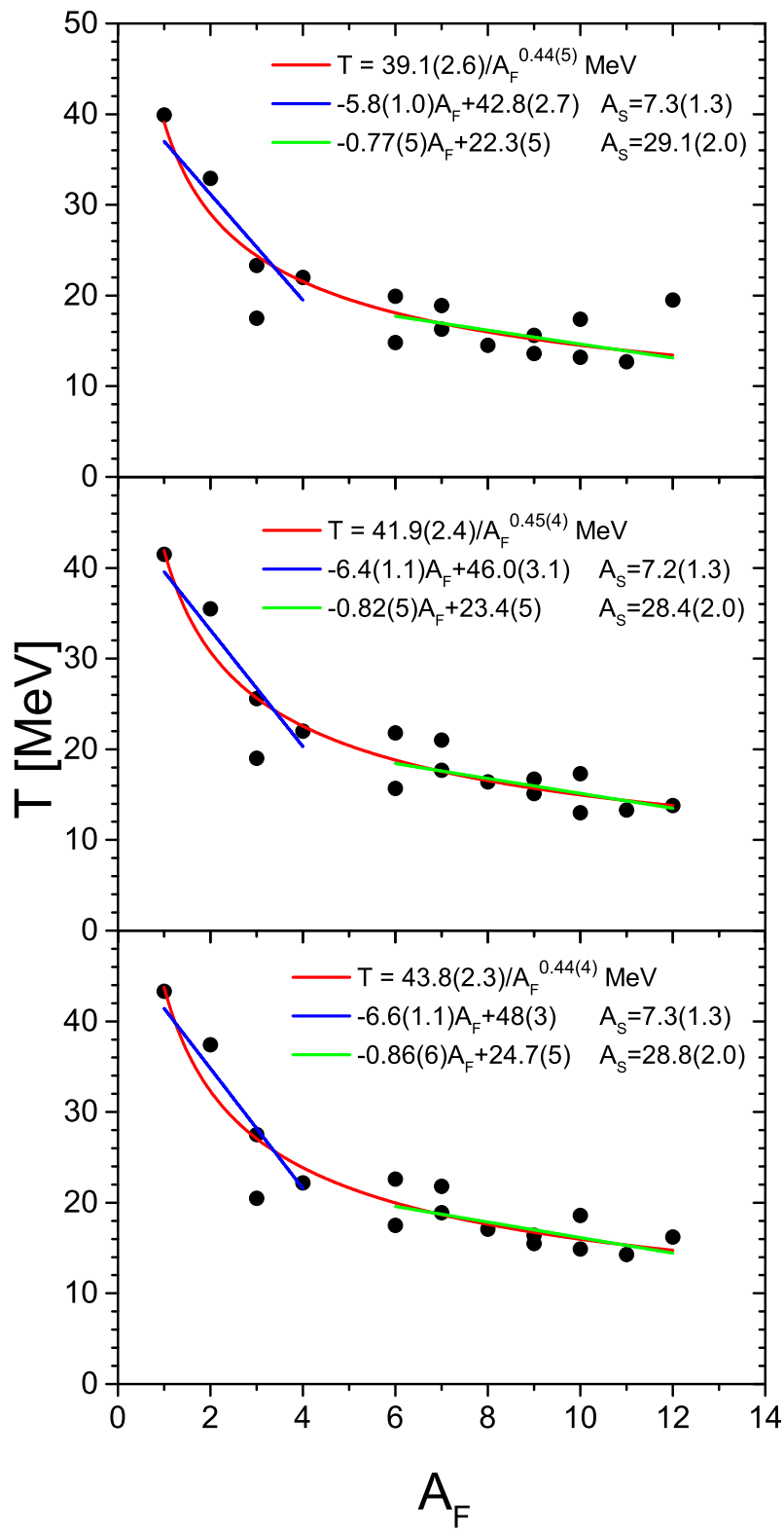


Figure 7.2. The same as for fig. 7.1 but for the silver target.

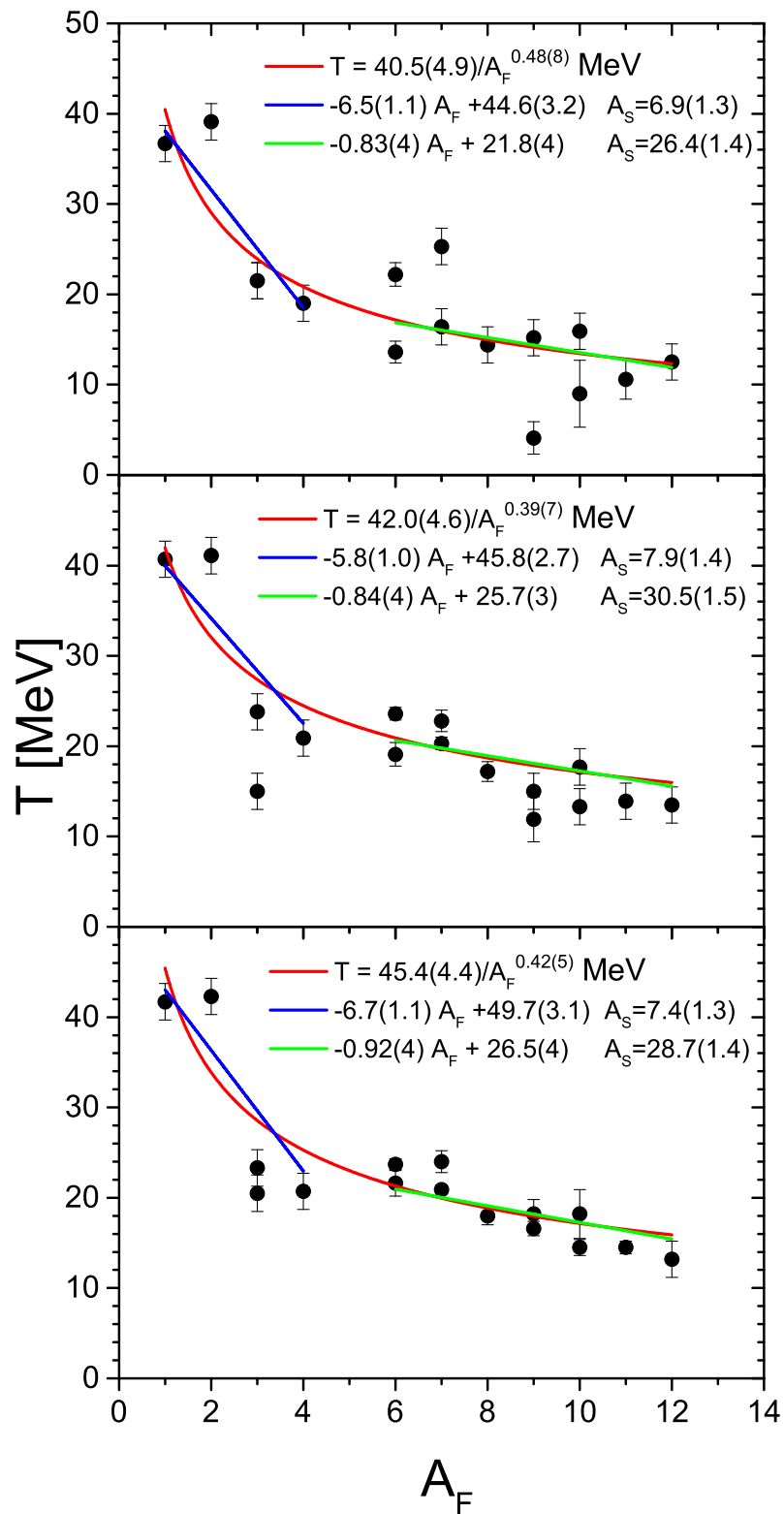


Figure 7.3. The same as for fig. 7.1 but for the gold target.

It is obvious that IMF cannot be emitted from very light sources which are built of only several nucleons. This explains why the sources responsible for the emission of IMF must be on average heavier than those participating in the emission of LCP. It is, however, not clear whether it is necessary to distinct only two groups of the sources with masses around  $A_S \sim 7$  and  $A_S \sim 28$ . Much more natural might be to postulate continuous distribution of the source masses with smoothly varying average source mass for given ejectile. Then the linear approximation to the dependence of the apparent temperature  $T$  on the ejectile mass should be replaced by some smooth function which would be adequate for full range of ejectile masses. In the present study the following parametrization of the apparent temperature  $T$  dependence on the ejectile mass  $A_F$  was used:

$$T = \frac{\alpha_T}{(A_F)^{\delta_T}} \quad (7.5)$$

where  $\alpha_T$  and  $\delta_T$  are free parameters.

The red line shown in figures 7.1, 7.2 and 7.3 represents temperature dependence on the ejectile mass corresponding to the parametrization 7.5. As can be seen in these figures the reproduction of the temperature values is very good for all targets and beam energies. Moreover, the values of the fitted parameters are very similar in all cases (cf. table 7.7).

Table 7.7. Values of the parameters,  $\alpha_T$  and  $\delta_T$ , of the formula 7.5, which represents the dependence of the source apparent temperature  $T$  on the mass  $A_F$  of emitted particles, fitted to whole range of  $A_F$  values. The numbers in last two columns depict the values of the parameters averaged over beam energies.

Target	$E_p$ GeV	$\alpha_T$	$\delta_T$	$\langle \alpha_T \rangle_{E_p}$	$\langle \delta_T \rangle_{E_p}$
Ni	1.2	40.7(3.0)	0.51(5)	42.1(1.9)	0.477(35)
	1.9	43.3(3.0)	0.48(6)		
	2.5	42.2(3.9)	0.44(7)		
Ag	1.2	39.1(2.6)	0.43(5)	41.6(1.4)	0.440(25)
	1.9	41.9(2.4)	0.45(4)		
	2.5	43.8(2.3)	0.44(4)		
Au	1.2	40.5(4.9)	0.48(8)	42.6(2.7)	0.430(39)
	1.9	42.0(4.6)	0.39(7)		
	2.5	45.4(4.4)	0.42(5)		

As can be seen the scatter of parameter values is very small for different energies and different targets. Thus it is reasonable to evaluate a general average (over targets and beam energies). The following values of these parameters have been found:

$$\langle \alpha_T \rangle = 42.1(1.2) \quad \langle \delta_T \rangle = 0.449(19) \quad (7.6)$$

The above values may be used to estimate the average temperature  $\tau_S(A_F)$  and mass number  $A_S(A_F)$  of the source associated with ejectiles with mass number  $A_F$  in the following way: If one assumes that the tangent  $T(A_F) = aA_F + b$  to the  $T(A_F)$  dependence 7.5 at given  $A_F$  (cf. Appendix B) is identical with the line 7.2 which

is due to the energy and momentum conservation during the emission of particles with mass  $A_F$  from an average source then:

$$A_S(A_F) = -\frac{b(A_F)}{a(A_F)} = -\frac{\alpha_T(\delta_T + 1)(A_F)^{-\delta_T}}{-\alpha_T\delta_T(A_F)^{-\delta_T-1}} = \frac{\delta_T + 1}{\delta_T}A_F \quad (7.7)$$

$$\tau_S(A_F) = b(A_F) = \frac{\alpha_T(\delta_T + 1)}{(A_F)^{\delta_T}} \quad (7.8)$$

what gives following approximate values:

$$A_S(A_F) \approx 3.2 \cdot A_F \quad (7.9)$$

$$\tau_S(A_F) \approx \frac{61.0}{(A_F)^{0.45}} \quad (7.10)$$

In the table below (7.8) the estimated mass and temperature of the average source obtained as arithmetic means of the values obtained from formulae 7.4 and 7.3 over LCP ( $A_F=1-4$ ) or over IMF ( $A_F=6-12$ ) are compared with those obtained as arithmetic means calculated over LCP or over IMF of values from equations 7.9 and 7.10, respectively.

Table 7.8. Comparison of source properties, mass and temperature, obtained in two different methods, described in details in text.

Light charged particles				Intermediate mass fragments			
$A_S$		$\tau_S$		$A_S$		$\tau_S$	
eq. 7.4	eq. 7.9	eq. 7.3	eq. 7.10	eq. 7.4	eq. 7.9	eq. 7.3	eq. 7.10
7.0(4)	8.0	46.0(1.0)	43.9	27.5(4)	28.8	23.8(1)	23.1

As can be seen both methods of estimation of mass  $A_S$  and  $\tau_S$  give almost the same results, however only the method based on averaging the values from eqs. 7.9 and 7.10 offers a possibility to extrapolate the estimation to heavier ejectiles.

### 7.2.2. Velocity parameter $\beta$

Velocity of the source -  $\beta$  is the next parameter of the phenomenological model of two moving sources. The ejectile mass dependence of this parameter shows also a regularity similar to that of the temperature parameter. Therefore the power law formula (equation 7.11) was used to describe the velocity dependence on the ejectile mass:

$$\beta = \frac{\alpha_\beta}{(A_F)^{\delta_\beta}} \quad (7.11)$$

The analysis of the present data for p+Ag collisions at 1.2, 1.9, and 2.5 GeV proton beam energies leads to the conclusion that indeed the mass dependence of the  $\beta$  parameter is well reproduced by this formula. Moreover it was found that values of  $\alpha_\beta$  and  $\delta_\beta$  parameters are almost the same for all studied energies as well as they agree well with values obtained from analysis of p+Ni and p+Au data published by A. Budzanowski et al. [8, 66]. This is illustrated by figures 7.4, 7.5, and 7.6 where the solid (red) line depicts values from the formula 7.11 and it is confirmed by content of the table 7.9. The averaged over energies values of the  $\alpha_\beta$

and  $\delta_\beta$  parameters for Ag target are almost the same in the limits of the uncertainties as those for the Ni and Au target.

Table 7.9. Parameters of the formula 7.11. The particles cover LCP and IMF with mass number up to  $A=12$ . The references indicate papers in which the phenomenological analysis of corresponding data is presented.

Nucleus	$E_p/\text{GeV}$	$\alpha_\beta$	$\delta_\beta$	$\langle \alpha_\beta \rangle$	$\langle \delta_\beta \rangle$	Reference
Ni	1.2	0.15(1)	0.84(7)	0.159(5)	0.89(5)	A. Budzanowski et al. [8]
	1.9	0.158(9)	0.92(8)			
	2.5	0.170(8)	1.01(7)			
Ag	1.2	0.135(8)	0.79(6)	0.144(7)	0.83(3)	current thesis
	1.9	0.147(7)	0.88(5)			
	2.5	0.142(7)	0.88(5)			
Au	1.2	0.16(2)	0.67(9)	0.166(9)	0.78(5)	A. Budzanowski et al. [66]
	1.9	0.18(2)	0.81(9)			
	2.5	0.16(1)	0.84(8)			
average				<b>0.156(4)</b>	<b>0.83(3)</b>	

It is interesting to note that the exponent of the denominator in equation 7.11, i.e. the  $\delta_\beta$  is close to unity;  $\delta_\beta \approx 0.83(3)$ . This may suggest that the following formula holds for all ejectiles in the limits of an accuracy of the present analysis.

$$\alpha_\beta \equiv \text{const} \approx \beta(A_F) \cdot A_F \quad (7.12)$$

The symbol  $A_F$  in the above formula represents mass number of the ejectile. Then the  $\alpha_\beta$  from the above equation might be interpreted as the average momentum of the ejectile equal to the average momentum transferred by the proton from the beam to the emitting source. To find whether this formula describes well the dependence of source velocity  $\beta$  on the ejectile mass  $A_F$  the fits of all data presented in figs. 7.4, 7.5, and 7.6 were repeated using formula 7.12. The obtained fits are presented in these figures as dashed (blue) lines. It is clear that the agreement of predictions of the single-parameter formula 7.12 with data is almost as good as the agreement of two-parameter formula 7.11. The obtained values of the  $\alpha_\beta$  parameter are listed in table 7.10.

It is evident from the table 7.10 that in the limits of parameter uncertainties the  $\alpha_\beta$  parameter value is independent of the beam energy for all targets. Furthermore, the variation of the parameters from target to target is also very small; it covers the range from  $\sim 0.153$  to  $\sim 0.188$  what corresponds (multiplying  $A_F$  by the mass unit) to the momentum range from  $\sim 142$  MeV/c to  $\sim 175$  MeV/c.

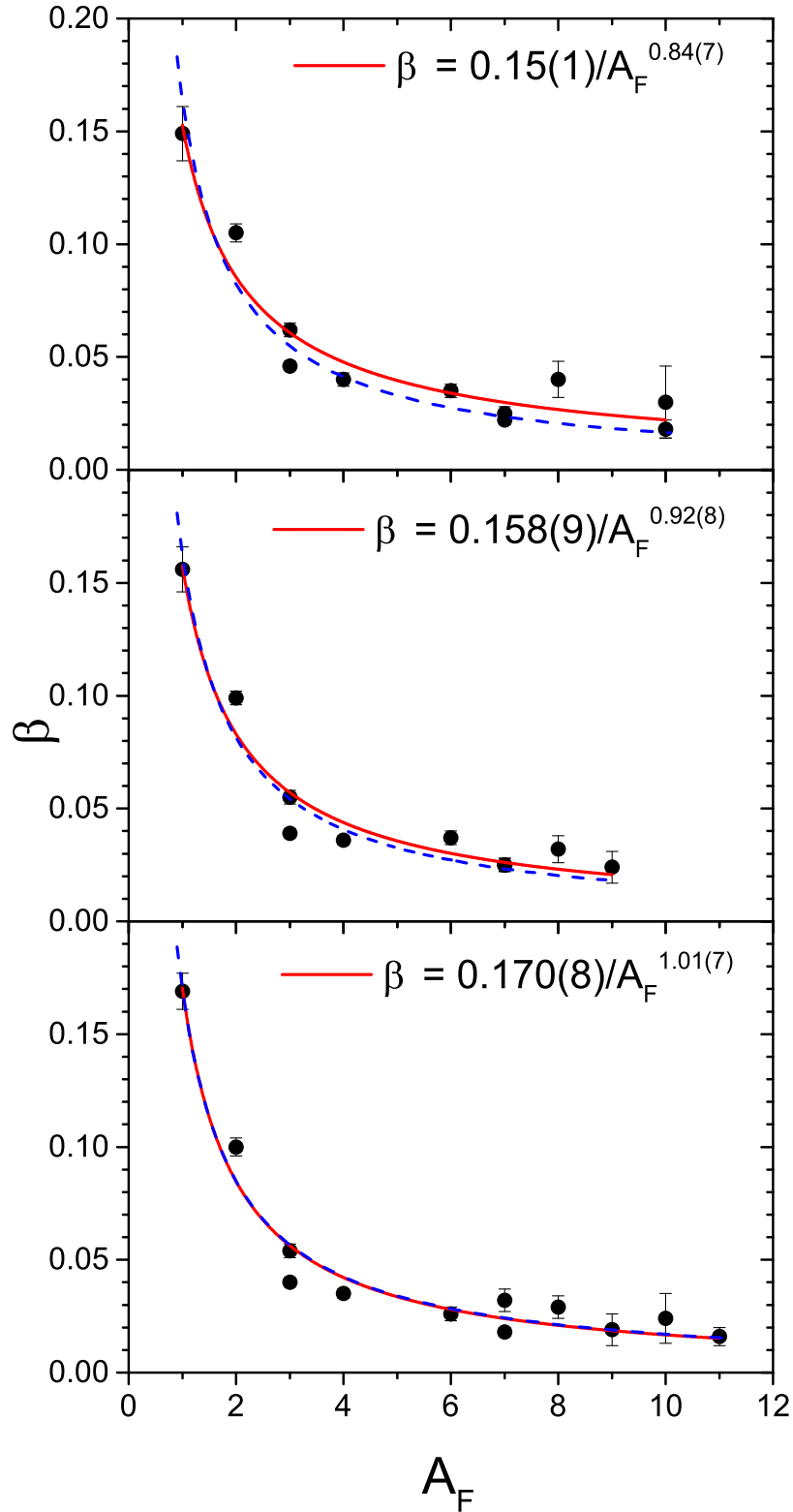


Figure 7.4. Ejectile mass number  $A_F$  dependence of  $\beta$  parameter representing the velocity of the moving source (in units of the speed of light) which emits the particles in proton - Ni collisions at proton beam energy 1.2 GeV (upper panel), 1.9 GeV (middle panel) and 2.5 GeV (lower panel). The solid (red) lines are representing fits of the formula 7.11 to the values of the  $\beta$  parameter whereas the dashed (blue) lines depict the fits of the formula 7.12.

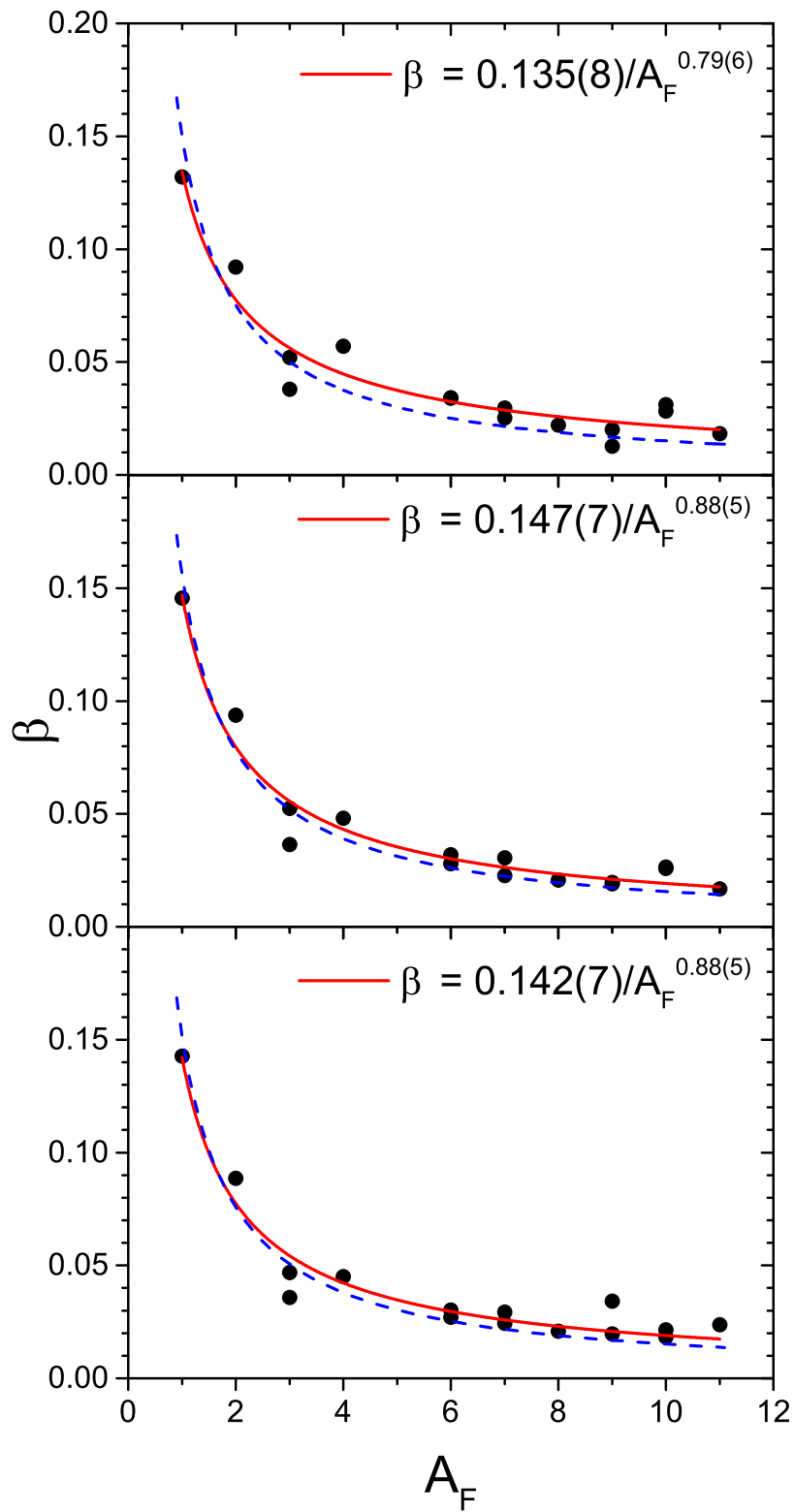


Figure 7.5. The same as in fig. 7.4, but for Ag target.

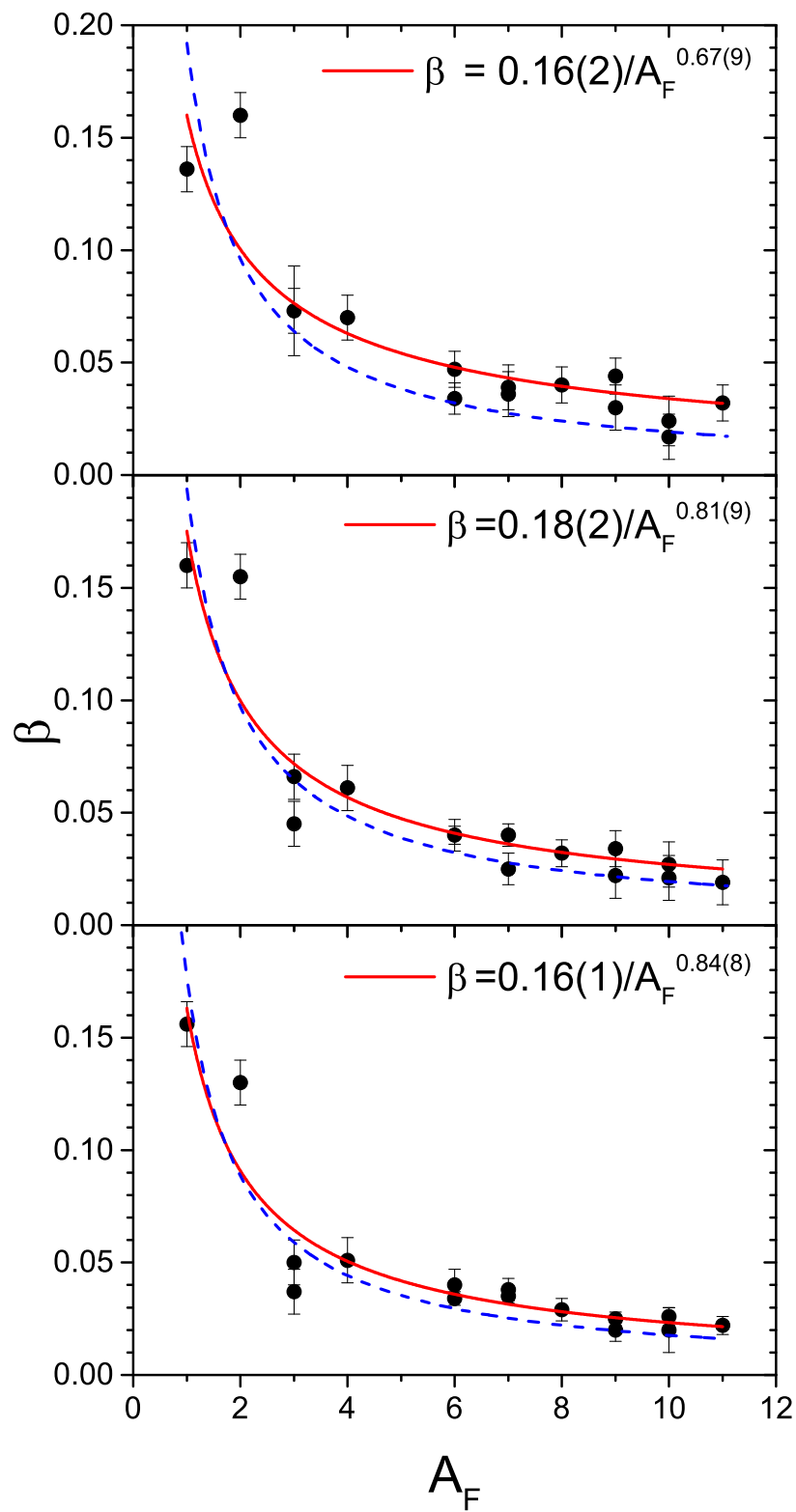


Figure 7.6. The same as in fig. 7.4, but for Au target.

Table 7.10. Parameter  $\alpha_\beta$  of the formula 7.12.

Target	$E_p/\text{GeV}$	$\alpha_\beta$	$\langle\alpha_\beta\rangle$
Ni	1.2	0.1647(96)	0.1658(47)
	1.9	0.1629(78)	
	2.5	0.1698(66)	
Ag	1.2	0.1503(89)	0.1527(43)
	1.9	0.1561(66)	
	2.5	0.1517(67)	
Au	1.2	0.192(20)	0.1877(92)
	1.9	0.194(15)	
	2.5	0.177(12)	
average			0.1687(38)

### 7.2.3. Absolute yield parameter $\sigma$

The last of the parameters entering the phenomenological model of two moving sources is the yield of the emitting sources -  $\sigma$ . It is known [41, 69, 70] that the typical ejectile mass dependence of the yields follow the „power-law“:

$$\sigma = \frac{\alpha_\sigma}{(A_F)^{\delta_\sigma}} \quad (7.13)$$

Therefore in the present investigations the „power-law“ was used to describe the observed mass dependence of the yields of both sources. The results of the parametrization are shown as red lines in figures 7.7, 7.8, and 7.9 for protons of three energies 1.2, 1.9, and 2.5 GeV bombarding Ni, Ag, and Au targets, respectively. Parameter values from the fits are listed in table 7.11 and shown as red dots in fig. 7.10. As can be seen the  $\alpha_\sigma$  values are different for different energies and targets whereas scatter for values of the  $\delta_\sigma$  parameter is much smaller. As it was found by A. D. Panagiotou et al. [41] the values of the exponent vary from 1.7 to 4.1, for wide range of target (Kr, Xe, Ag, Au, U) and beam energies from 180 MeV up to 350 GeV. It has been suggested by J. E. Finn et al. [71], and R. E. L. Green et al. [13], that the dependence of the exponent parameter on projectile beam energy should be nonmonotonic with a minimum at the energy at which liquid-gas phase transition appears. At this energy the exponent parameter should be inside the range  $2 \leq \delta_\alpha \leq 3$  [13]. Current results of  $\delta_\sigma$  averaged over three targets (Ni, Ag, and Au) are presented as red dots in figure 7.10 in order to compare with those discussed in the section 2 (cf. fig. 2.6). It may be concluded that suggested changes in the reaction mechanism are not presented up to proton beam energy 2.5 GeV i.e. there is no clear evidence for the postulated liquid-gas phase transition.

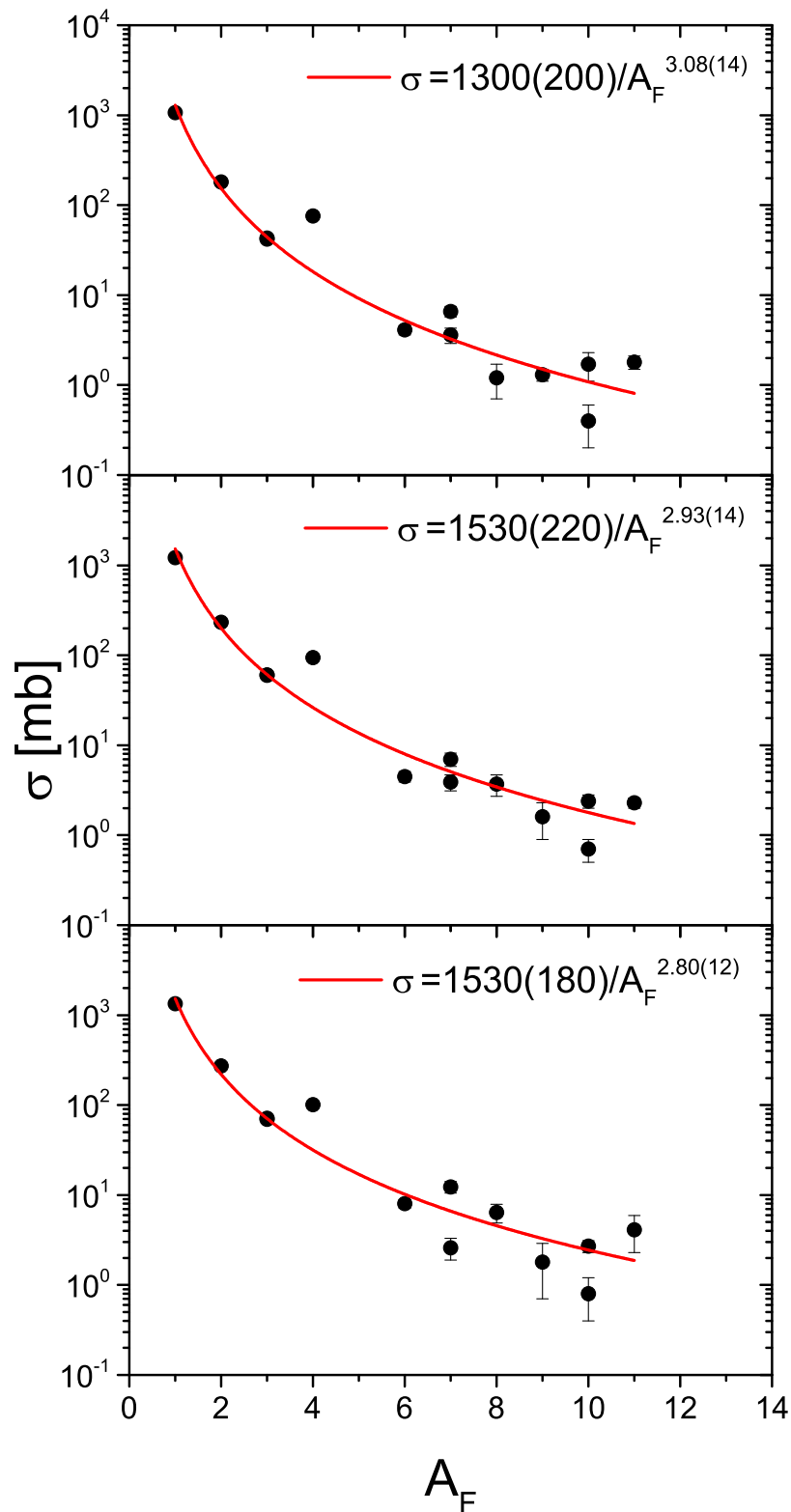


Figure 7.7. Ejectile mass number  $A_F$  dependence of  $\sigma$  parameter representing the cross section for emission from the source the particles in proton - Ni collisions at proton beam energy 1.2 GeV (upper panel), 1.9 GeV (middle panel) and 2.5 GeV (lower panel). Red lines are fitted to points according to formula 7.13.

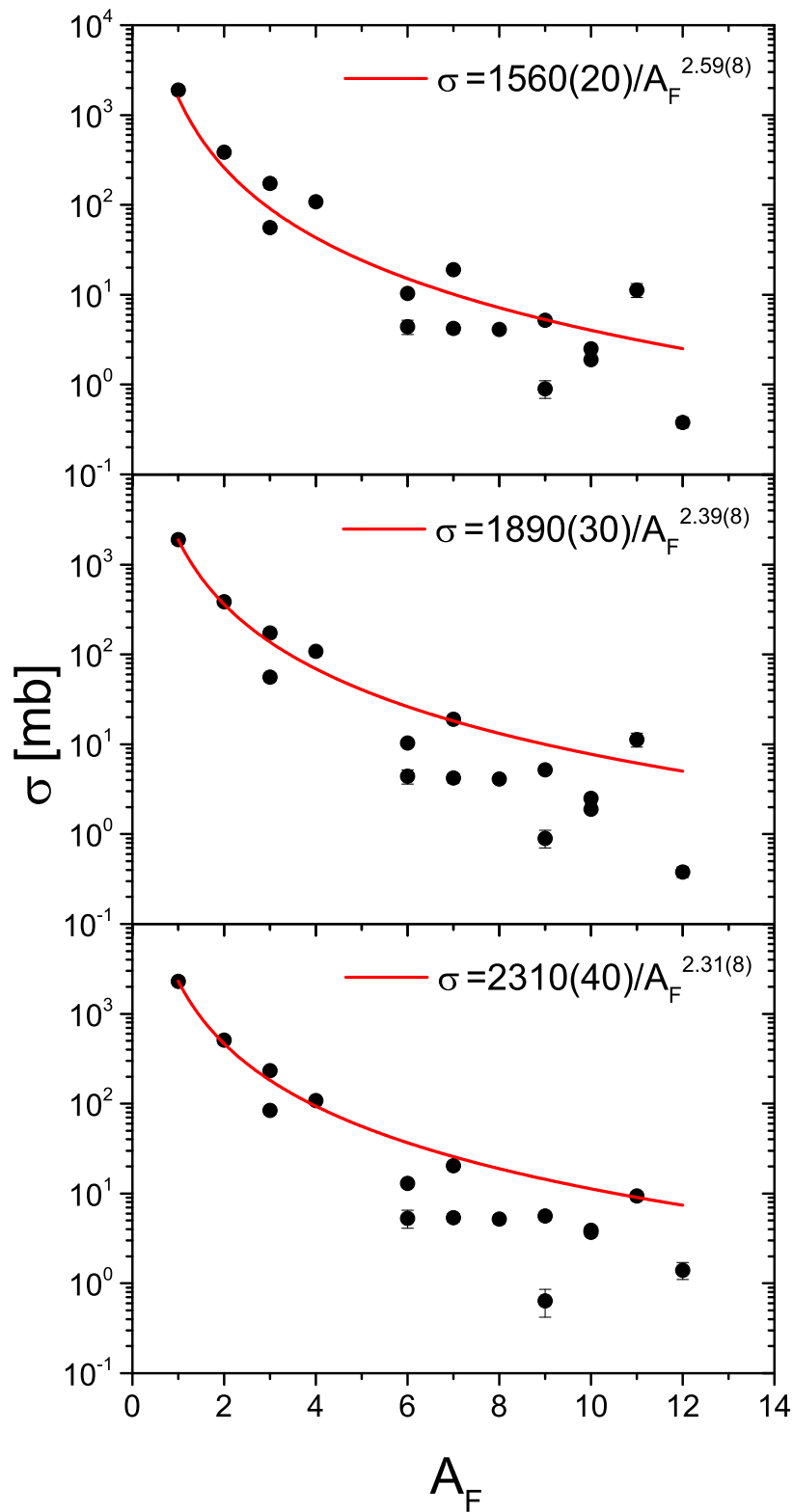


Figure 7.8. The same as in fig. 7.7, but for silver target.

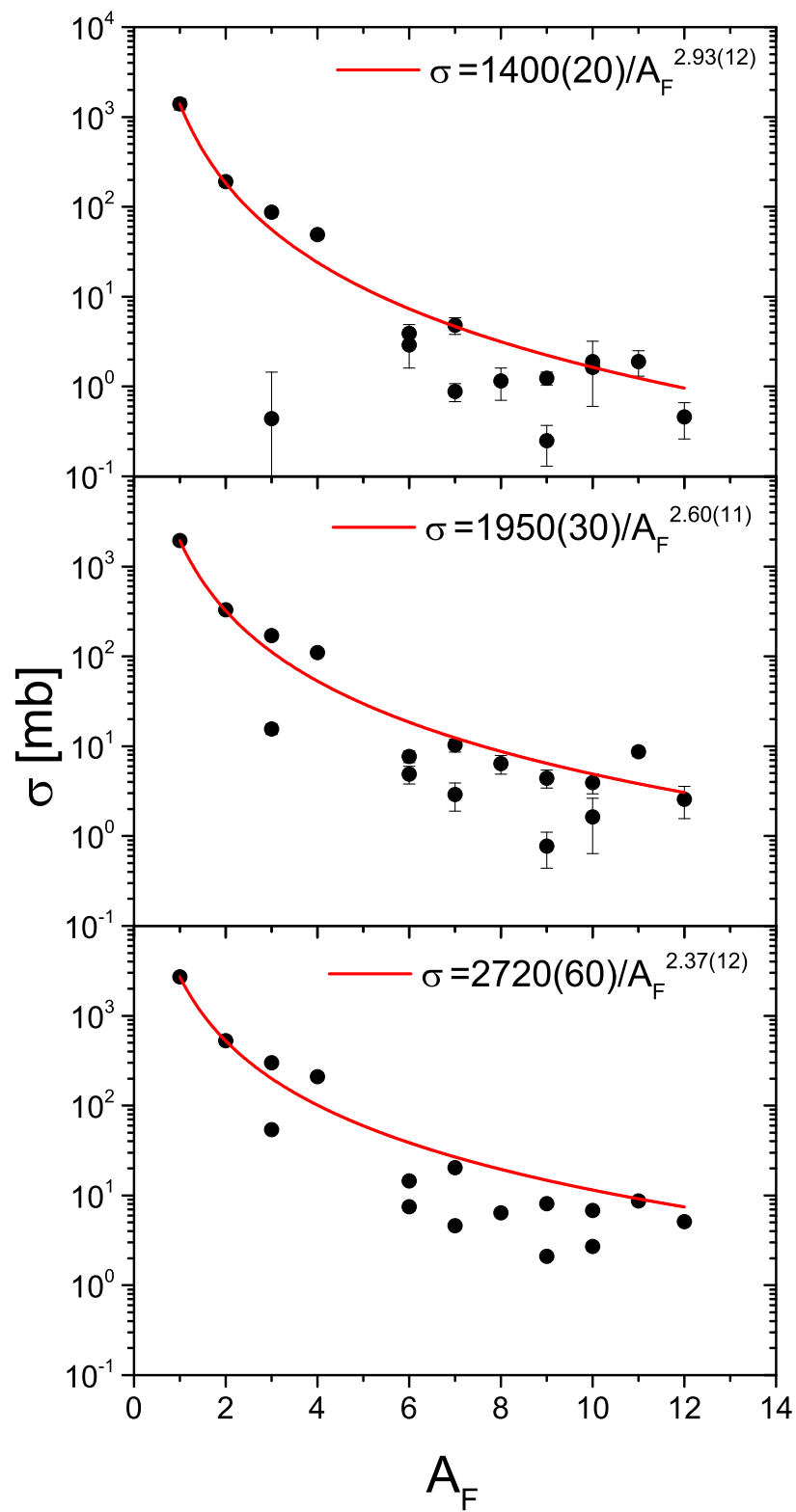


Figure 7.9. The same as in fig. 7.7, but for gold target.

Table 7.11. Parameters of the formula 7.13 which represents the dependence of the cross section on the mass of emitted particles. The references indicate papers in which the phenomenological analysis of corresponding data is presented.

Nucleus	$E_p/\text{GeV}$	$\alpha_\sigma/\text{mb}$	$\delta_\sigma$	Reference
Ni	1.2	1300(200)	3.08(14)	A. Budzanowski et al. [8]
	1.9	1530(220)	2.93(14)	
	2.5	1530(180)	2.80(12)	
Ag	1.2	1560(20)	2.59(8)	current thesis
	1.9	1890(30)	2.39(8)	
	2.5	2310(40)	2.31(8)	
Au	1.2	1400(20)	2.93(12)	A. Budzanowski et al. [66]
	1.9	1950(30)	2.60(11)	
	2.5	2720(60)	2.37(12)	

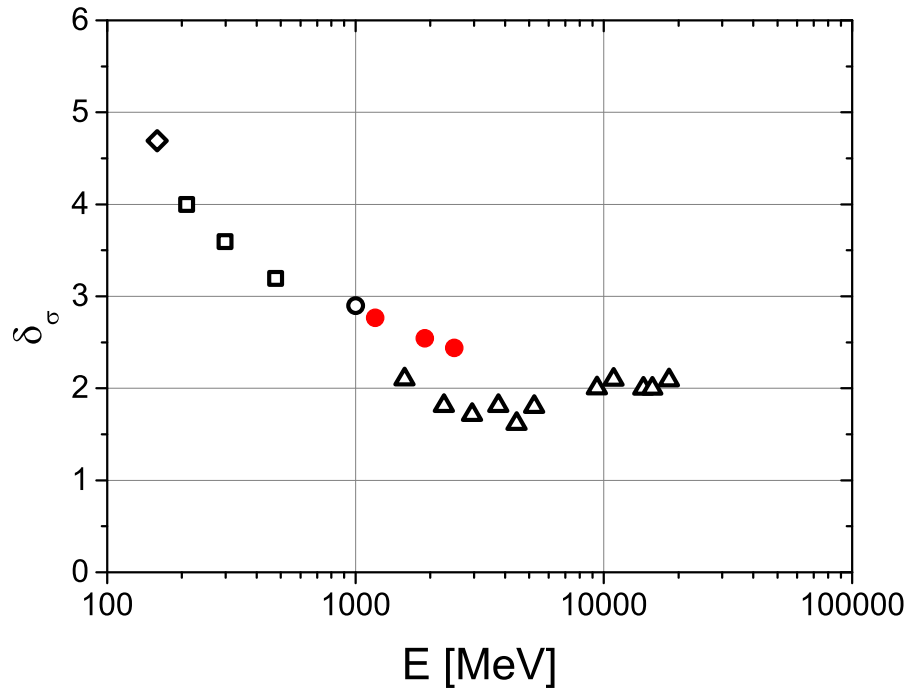


Figure 7.10. „Power-law” parameter  $\delta_\sigma$  as a function of proton beam energy. Red dots present values obtained in current analysis, averaged over the beam energy.

Open symbols depict the same data as in fig. 2.6 in section 2 of present thesis.

## Chapter 8

# Summary and conclusions

In the present thesis the experimental and model investigations of the reactions in the p+Ag collisions were performed for proton beam energy of 1.2, 1.9, and 2.5 GeV. The aim of this work was to obtain new, high statistic experimental data which would allow to study the reaction mechanism in p+Ag nuclear system and to compare it with that previously investigated for p+Al [48], p+Ni [8, 65], and p+Au [8, 66] nuclear systems at the same energies.

Double differential cross sections  $\frac{d^2\sigma}{dEd\Omega}$  were measured at seven scattering angles: 15.6°, 20°, 35°, 50°, 65°, 80°, and 100° (in the LAB system) for isotopically identified hydrogen ( $^1\text{H}$ ,  $^2\text{H}$ ,  $^3\text{H}$ ), helium ( $^3\text{He}$ ,  $^4\text{He}$ ,  $^6\text{He}$ ), lithium ( $^6\text{Li}$ ,  $^7\text{Li}$ ,  $^8\text{Li}$ ,  $^9\text{Li}$ ), beryllium ( $^7\text{Be}$ ,  $^9\text{Be}$ ,  $^{10}\text{Be}$ ) and boron ( $^9\text{B}$ ,  $^{10}\text{B}$ ,  $^{11}\text{B}$ ) ejectiles. Additionally data for C, N, and O elements (without isotopic identification) were obtained. The cross sections determined in the present work were compared with those measured by Herbach et al. [32] for 1.2 GeV proton beam impinging on Ag target. The comparison was performed for the hydrogen, lithium and beryllium data summed over isotopes and integrated over angles of the present  $\frac{d^2\sigma}{dEd\Omega}$  cross sections because the Herbach data were published as the angle integrated spectra  $d\sigma/dE$  summed over isotopes or as the angle and energy integrated total production cross sections  $\sigma$  for individual isotopes and therefore presenting the very same observables accessible in the current thesis. It was checked that the present cross sections agree very well with all cross sections measured by Herbach et al. [32]. It is worth emphasizing that the data measured in the present work form the most extensive, in terms of statistics, set of the cross sections published in the literature for Ag target at the range of 1 - 3 GeV of proton beam energies.

The present data have the same character at all three energies, i.e., the shape of the spectra and their angular dependence is almost the same. They differ mainly in the absolute magnitude - the cross sections increase with the beam energy. It is possible to distinguish two components of the spectra for both, LCP and IMF: (i) the isotropic component for ejectile energies smaller than  $\sim 30$  MeV, and (ii) the forward peaked component for ejectiles with larger energies. It is important to note, that the same character of spectra was observed for Al [48], Ni [8, 65], and Au [8, 66] targets in the same beam energy range. Such behavior of the data was interpreted as a manifestation of two mechanisms of the reaction. The anisotropic, high energy contribution was attributed to the fast, pre-equilibrium stage of the reaction whereas the isotropic one to the de-excitation of the equilibrated target remnant after the first stage of the process.

The data measured in the present experiment have been confronted with results

of microscopic model which assumes that the fast stage of the reaction occurs as an intranuclear cascade of the nucleon-nucleon and nucleon-pion collisions leaving an excited, equilibrated remnant of the target which afterward may more slowly evaporate particles or is subject of multifragmentation.

The first step of the process was described by the INCL4.3 [5] computer program which allows for emission of light complex particles besides the nucleons and pions. The high energy part of present experimental spectra of LCP was reasonably well reproduced by the intranuclear cascade model, however, the disagreement was always visible for spectra measured at small scattering angles in the energy range of ejectiles between  $\sim 50$  MeV and  $\sim 150$  MeV. This underestimation of the experimental data is strongest for protons and other hydrogen isotopes and decreases for heavier particles. It was observed that; (i) the coalescence of nucleons from the cascade into light complex particles is crucial for proper description of the high energy part of the spectra of complex LCP, (ii) lack of similar mechanism in the INCL4.3 model for IMF leads to the underestimation of the high energy part of the IMF spectra. In recent years a new version of the INCL model was developed (INCL4.6 [6]) which allows for coalescence of nucleons also in IMF (with mass number  $A < 9$ ). However, it was found [7] that this model produces IMF spectra for p+Ag collisions at 0.48 GeV proton beam energy with too small slope of the high energy tail and therefore it overestimates significantly the high energy part of the IMF spectra. This information as well as the intention to compare the present results with those of the investigations published for Ni [8,65] and Au targets [8,66] which were performed using the INCL4.3 model was the reason to apply this older version of the intranuclear cascade in the present work.

The second stage of the reaction was described by two models which differ in the assumptions concerning the mechanism of the de-excitation of the target remnant. The GEM2 computer program of Furihata [54, 55] assumes that the excited residuum of the target evaporates particles whereas the SMM model of Botvina et al. [56, 57, 63] allows for competition of the evaporation and the multifragmentation processes. Both these models produce the cross sections which are concentrated at lowest energies visible in the spectra, i.e. for energies smaller than  $\sim 30$  MeV. It was found that the predictions of the SMM model reproduce significantly better the IMF data whereas those of the GEM2 are slightly better for LCP. Both these models are not able to reproduce the experimental spectra for the energies in the range from  $\sim 50$  MeV to  $\sim 150$  MeV for LCP and lightest IMF (Li and B), especially at small scattering angles.

The systematic disagreement of the experimental spectra and predictions of the microscopic models described to above suggested that an additional mechanism should be taken into consideration. This was realized phenomenologically by introducing the source moving along the direction of the beam, isotropically emitting the particles. The velocity of the source, its temperature as well as the yield of emitted particles were treated as free parameters. In the case of LCP a single source was added, whereas for IMF two sources were taken into account. First of them imitated predictions of the SMM and/or GEM2 as it was done in refs [66] (for Au) and [8] (for Ni), whereas the second corresponded to the analogous fast source as that used for LCP.

It was found that the parameters of the fast source for all investigated particles

from protons up to boron isotopes vary very smoothly when treated as functions of ejectile mass. This ejectile mass  $A_F$  dependence was described by two parameter power function:

$$T = \frac{\alpha_T}{(A_F)^{\delta_T}}, \quad \beta = \frac{\alpha_\beta}{(A_F)^{\delta_\beta}}, \quad \sigma = \frac{\alpha_\sigma}{(A_F)^{\delta_\sigma}}$$

where the  $\alpha$  and  $\delta$  parameters are of course different for  $T$ ,  $\beta$  and  $\sigma$ . Values of these parameters almost do not change with the beam energy (with exception of those for the yield parameter  $\sigma$ ).

The parameters of the fast source obtained from the present phenomenological analysis were compared to the parameters of the corresponding source introduced in the literature for Ni [8,65], and Au [8,66] targets in the same beam energy range. It was found that the ejectile mass dependence of the source velocity  $\beta$  and its temperature  $T$  can be very well reproduced by the same power function as used in the present investigation. Moreover, it was found that the parameters of the power function practically do not change with the mass of the target nucleus from Ni up to Au and with the proton beam energy.

The mass dependence of the temperature parameter allowed to estimate an average mass of the source emitting LCP as well as that emitting IMF. It was found by two different methods that the source emitting LCP is built of 7 - 8 nucleons for all studied targets and beam energies. The source of IMF is heavier - with average mass of about 28 nucleons. No significant variation of these source masses was observed for all studied targets and beam energies.

The mass dependence of the velocity  $\beta$  of the source moving along the beam direction was also found to be very smooth. It was observed that the simple formula  $\beta = \text{const}/A_F$  (where  $A_F$  stands for mass number of the ejectile) well reproduces the velocity dependence. The constant factor in this formula may be interpreted as the average momentum along the beam transferred to the source by the impinging proton. It was found that this momentum is slightly different for individual targets (from  $\sim 140$  MeV/c to  $\sim 180$  MeV/c) but is independent of the beam energy inside the error limits.

The ejectile mass dependence of the absolute yield parameter of the source  $\sigma$  could be also well described by the power function  $\sigma = \frac{\alpha_\sigma}{(A_F)^{\delta_\sigma}}$ . The  $\alpha_\sigma$  parameter increases with energy for all targets with exception of Ni, where the same value of this parameter was found for 1.9 and 2.5 GeV proton beam energy. This might indicate the beginning of saturation (leveling) of the energy dependence of the production cross section  $\sigma$  for Ni in the neighborhood of 1.5-1.9 GeV whereas for heavier targets this asymptotic region is still not achieved. The  $\delta_\sigma$  parameter decreases with the beam energy for all studied targets. This seems to agree with observation published in the literature for the studied range of the beam energies (cf. eg. [17]).

In summary, the present investigations of double differential cross sections  $\frac{d^2\sigma}{dEd\Omega}$  give evidence for non-equilibrium process proceeding in proton-nucleus collisions with the emission of light charged particles (LCP) and intermediate mass fragments (IMF) which is not reproduced by the microscopic models used at present in the literature. Similar effects were observed in proton emission channel from p+Al, p+Cu, and p+Pb collisions in studies of Shibata et al. [72] and En'yo et al. [73] in the proton beam energy range from 0.73 GeV to 3.17 GeV. Such a phenomenon was

also reported for IMF channels by Green et al. [13] for p+ Ag collisions at 0.48 GeV and Porile et al. [30] for 1.9 GeV to 5.3 GeV proton induced reactions on Xe target.

It was shown that this process may be phenomenologically described as a formation and decay of the source moving along the beam direction. Properties of the source almost do not change in the proton beam energy range studied in the present work, i.e., from 1.2 GeV to 2.5 GeV. Furthermore they are almost the same as properties of the source found in p+Ni [8, 65] and in p+Au [8, 66] collisions in the same energy range. Therefore the presence of a source emitting LCP and IMF with the *specific properties* described to above is well established for a broad range of targets and beam energies from 1.2 to 2.5 GeV.

All the microscopic models which aspire to realistic description of the reaction mechanism should take it into consideration.

## Appendix A

# Two moving source model

In this appendix details of the two moving source model will be presented. An idea to describe experimental data in such a way was taken from original paper of G. D. Westfall et al. [38]. This model assumes that the particles are emitted from two sources moving along the direction of the proton beam. The angular distribution of emitted particles is isotropic in the rest frame of each source, and the distribution of the kinetic energy  $E^*$  available in the two-body decay of the emitting source has a Maxwellian shape with slope characterized by the temperature parameter  $\tau$ :

$$\frac{d^2\sigma}{dE^*d\Omega^*} = \frac{\sigma}{2(\pi\tau)^{3/2}} \sqrt{E^*} \exp\left[-\frac{E^*}{\tau}\right]. \quad (\text{A.1})$$

The normalization of (A.1) assures that the parameter  $\sigma$  is equal to total cross section, i.e., cross section obtained from integration over energies and angles.

Due to the momentum and energy conservation laws, the kinetic energy  $E'$  of an emitted fragment, differs from the total kinetic energy  $E^*$  available in the source rest frame:

$$E^* = \nu E', \quad (\text{A.2})$$

where  $\nu$  is a recoil correction expressed by mass of the source  $A_S$ , and mass of the detected fragment  $A_F$ , as follows:

$$\nu = \frac{A_S}{A_S - A_F}. \quad (\text{A.3})$$

Using formula (A.2) it is possible to rewrite equation (A.1) in the following way:

$$\frac{d^2\sigma}{dE'd\Omega'} = \frac{\sigma}{2(\pi T)^{3/2}} \sqrt{E'} \exp\left[-\frac{E'}{T}\right], \quad (\text{A.4})$$

after introducing a new variable  $T$ , defined as:

$$T \equiv \frac{\tau}{\nu}. \quad (\text{A.5})$$

This temperature parameter  $T$  corresponds to the kinetic energy of the ejectile. The ejectiles emitted in the single step from the equilibrated excited nucleus have the spectra with exponential high energy tails. The slope of such an exponential function is connected to the temperature  $T$  of the emitting source  $f(E) \sim \exp(-E/T)$ . In the proton induced reactions on nuclei, e.g., G. D. Westfall et al. [38], the particle energy spectra in the reference frame of the excited nucleus are usually described by the Maxwell distribution given by the eq. A.4.

It has to be taken into consideration that the charged particles emitted from the charged source must overcome the Coulomb barrier. The simple estimate of the height of the Coulomb barrier  $B$  may be performed treating the charged particles as two touching spheres:

$$B = \frac{Z_F(Z_S - Z_F)e^2}{1.44 [A_F^{1/3} + (A_S - A_F)^{1/3}]} MeV, \quad (A.6)$$

where subscript F represents the fragment emitted from the source, and subscript S denotes the source.

There are two simple ways of taking into account the Coulomb barrier. The first of them consists in shifting energy argument of Maxwell function (A.4) by the value of the barrier. This procedure is equivalent to sharp cutoff and therefore additional averaging over the height of the barrier should be introduced [38]. In the second method, the Maxwell distribution may be multiplied by smoothly varying with energy, probability function to overcome the barrier. In this thesis probability P was parameterized as:

$$P = \frac{1}{1 + \exp \left[ -\frac{E - kB}{d} \right]}, \quad (A.7)$$

where parameter  $k$  gives the height of the Coulomb barrier in units of  $B$ , parameter  $d$  describes curvature of the Coulomb barrier. In the calculations the ratio  $kB/d$  was kept constant.

Finally, after introduction P function, we obtain the following formula:

$$\frac{d^2\sigma}{dE'd\Omega'} = \frac{\sigma}{4\pi T^{3/2} I(kB, d, T)} \frac{\sqrt{E'} \exp \left[ -\frac{E'}{T} \right]}{1 + \exp \left[ \frac{kB - E'}{d} \right]} \quad (A.8)$$

where:

$$I(kB, d, T) = \int_0^\infty \frac{\sqrt{x} e^{-x}}{1 + \exp \left[ \frac{kB - Tx}{d} \right]} dx. \quad (A.9)$$

The integral  $I(kB, d, T)$  used for normalization of (A.8), preserve previous interpretation of  $\sigma$  parameter.

To compare model predictions with experimental data it is necessary to transform equation (A.8) from the rest frame of the emitting source to the laboratory system. It can be shown that the transformation formula should be as follows:

$$\frac{d^2\sigma}{dEd\Omega} = \frac{p}{p'} \frac{d^2\sigma}{dE'd\Omega'} \approx \sqrt{\frac{E}{E'}} \frac{d^2\sigma}{dE'd\Omega'} \quad (A.10)$$

where variables with prim correspond to the rest frame of the emitting source, and variables without prim describe the laboratory system. The approximation in the last formula is valid in non relativistic limit which is usually well obeyed in the studied reactions. The non relativistic relationship between kinetic energy  $E'$  of

emitted particle in the rest frame of the source and kinetic energy  $E$ , and angle  $\theta_{lab}$  in the laboratory system is given by:

$$E' = E + \frac{m\beta^2}{2} - \sqrt{2mE} \beta \cos\theta_{lab}. \quad (\text{A.11})$$



## Appendix B

# Determination of the mass $A_{source}$ and the temperature $\tau_{source}$ from the tangent to the $T(A)$ function

A tangent to the function  $y=f(x)$  at point  $(x_0, y_0)$ , i.e. a straight line that touches a curve  $y=f(x)$  at that point without intersecting it is described by the following formula:

$$y = \frac{df(x = x_0)}{dx} \cdot (x - x_0) + y_0$$

i.e.

$$y = a \cdot x + b \quad (\text{B.1})$$

$$a = \frac{df}{dx}(x = x_0) \quad (\text{B.2})$$

$$b = y_0 - \frac{df}{dx}(x = x_0) \cdot x_0 \quad (\text{B.3})$$

For  $f(x) = \alpha x^{-\delta}$  the tangent  $y = ax + b$  has the following parameters  $a$  and  $b$ :

$$a = -\alpha\delta \cdot x_0^{-\delta-1} \quad (\text{B.4})$$

$$b = \alpha(\delta + 1)x_0^{-\delta} \quad (\text{B.5})$$

The mass of the source found from the tangent at  $A_0$  of the function  $T = \alpha/A^\delta$  is equal to

$$A_{source} = -\frac{b}{a} = \frac{\delta + 1}{\delta} \cdot A_0 \quad (\text{B.6})$$

and the temperature  $\tau_{source}$  of the source:

$$\tau_{source} = b = \alpha(\delta + 1)A_0^{-\delta} \quad (\text{B.7})$$



## Appendix C

# List of the papers on $p+\text{Ag}$ reactions at GeV proton beam energies

Table C.1 contains a review on experiments in which reactions induced by protons on the silver or similar targets were investigated.

Table C.1. Review of experiments performed for reaction induced by proton on silver or similar target.

Authors & Reference no.	Energy of protons	Observables and reaction products
A. Abduzhamilov et al. [15]	800 GeV	The angular dependence, multiplicity and pseudorapidity distribution without identification of products.
E. W. Baker et al. [74]	1 GeV 2 GeV 3 GeV	The energy dependence of number of $^4\text{He}$ tracks.
A. Bujak et al. [33]	300 GeV	Total cross section in function of fragment mass for wide range of registered product mass, from $A=6$ to $A=106$ .
G. D. Cole et al. [75]	400 GeV 18.5 GeV ( $^{12}\text{C}$ )	Mean range and forward-to-backward ratio for many products from $^{24}\text{Na}$ to $^{52}\text{Mn}$ .
J. B. Cumming et al. [76]	2.9 GeV	The recoil products registered at $90^\circ$ (Sr, Cu, Sc, K, Na) Relative intensity in function of energy of products.
G. English et al. [34]	300 GeV	Measurement of $\sigma$ - total production cross section for 72 nuclides from $^7\text{Be}$ to $^{106}\text{Ag}$ .
G. English et al. [40]	11.5 GeV	Measurement of $\sigma$ - total production cross section for 72 nuclides from $^7\text{Be}$ to $^{106}\text{Ag}$ .
R. E. L. Green et al. [10]	0.21 GeV 0.3 GeV 0.48 GeV	Double differential cross sections $\frac{d^2\sigma}{dE d\Omega}$ of $^3\text{He}$ , $^4\text{He}$ at several angles.
R. E. L. Green et al. [11]	0.21 GeV 0.3 GeV 0.48 GeV	Double differential cross sections $\frac{d^2\sigma}{dE d\Omega}$ of isotopically identified $^6,7,8\text{Li}$ ; $^7,9,10\text{Be}$ ; and of elementally identified products from B to Na.
R. E. L. Green et al. [12]	0.518 GeV 0.237 GeV 0.445 GeV	Analyzing power $A_y$ for $^3\text{He}$ , $^4\text{He}$ at several angles
R. E. L. Green et al. [13]	0.48 GeV	Double differential cross sections $\frac{d^2\sigma}{dE d\Omega}$ measured for 46 isotopes from Li to Mg at several angles.

Authors & Reference no.	Energy of protons	Observables and reaction products
R. E. L. Green et al. [14]	0.3 GeV 0.19 GeV	Double differential cross sections $\frac{d^2\sigma}{dE d\Omega}$ measured for: p, d, t, $^3\text{He}$ , $^4\text{He}$ , $^6\text{Li}$ , $^7\text{Be}$ at several angles.
C.-M. Herbach et al. [32]	1.2 GeV	Registered products: p, d, t, $^3\text{He}$ , $^4\text{He}$ , $^6\text{Li}$ , $^7\text{Be}$ , $^8\text{Li}$ , $^9\text{Li}$ , $^{10}\text{Be}$ total cross sections, energy spectra, and angular distributions.
A. S. Hirsch [36]	80 GeV/c 350 GeV/c	registered products for: $3 \leq Z \leq 13$ measured $\sigma(E, \theta)$ .
J. Hudis et al. [35]	3 GeV and 29 GeV	Yields of Ne, Ar, Kr and Xe fragments.
J. Hudis et al. [77]	0.6 GeV 1 GeV 2 GeV 3 GeV 13 GeV 29 GeV 300 GeV	Fission products, $\sigma(E)$ .
J. Hudis [78]	1 GeV 2 GeV 3 GeV	Yields of $^{24}\text{Ne}$ and $^{24}\text{Na}$ .
E. K. Hyde et al. [4]	5.5 GeV	Double differential cross sections $\frac{d^2\sigma}{dE d\Omega}$ measured at several angles for p, d, t, $^3\text{He}$ , $^4\text{He}$ , $^6\text{He}$ , $^6\text{-}^9\text{Li}$ , $^7\text{Be}$ , $^9,^{10}\text{Be}$ $^{8,10-13}\text{B}$ , $^{10-14}\text{C}$ , $^{14,15}\text{N}$ , C, N, O, F, Ne, Na, Mg, Al, Si.
S. Katcoff [79]	2.2 GeV	Measured number of tracks in function of kinetic energy of $^8\text{Li}$ for $55^\circ$ i $125^\circ$ angles.
S. Katcoff et al. [80]	1 GeV 2 GeV 2.2 GeV 3 GeV	Number of tracks in function of beam energy. $^8\text{Li}$ for angles: $35^\circ$ , $45^\circ$ , $90^\circ$ , $125^\circ$ , $135^\circ$ .

Authors & Reference no.	Energy of protons	Observables and reaction products
S. Katcoff et al. [39]	3 GeV 29 GeV	Total cross section of 60 products, distinguished by mass and charge: from $^{22}\text{Na}$ to $^{106}\text{Ag}$ .
R. G. Korteling et al. [28]	5 GeV	$\frac{d^2\sigma}{dE d\Omega}$ measurements for $^{3,4,6}\text{He}$ , $^{6,7,8}\text{Li}$ , $^{7,9,10}\text{Be}$ , $^{11}\text{B}$ , and for elementally identified products with $Z$ up to 16.
R. G. Korteling et al. [16]	0.3 GeV	$\frac{d^2\sigma}{dE d\Omega}$ measured for products with $Z=1, 2$ .
A. A. Kotov et al. [42]	1 GeV	Measurements of total cross sections for fragments with $3 \leq Z \leq 15$ for silver target also Al, Ni, Au targets were used.
M. Lagarde-Simonoff et al. [81]	0.6 GeV, 10.5 GeV, 21 GeV	Measured total cross section, $\sigma$ , of $^{83,84,86}\text{Rb}$ .
X. Ledoux et al. [22]	for p beam: 0.475 GeV	Multiplicity of fission fragments, neutrons, and products with $Z=1$ and $Z>3$ , double differential cross sections $\frac{d^2\sigma}{dE d\Omega}$ for: $Z=2, Z=3$ .
M. Lefort et al. [82]	for p and $^3\text{He}$ beams: 2 GeV	The angular and energy distributions of d, t, $^3\text{He}$ , $^4\text{He}$ .
R. Michel et al. [25]	0.157 MeV	Total cross sections for p-induced reaction on twenty targets.
J. Murata [23]	8 GeV 12 GeV	Measurements of $\frac{d^2\sigma}{dE d\Omega}$ of elementally identified fragments for $3 \leq Z \leq 30$ .
P. Napolitani et al. [49]	1 GeV	Production cross section and energy spectra in inverse kinematic with Xe beam. Reaction products from Li to Ba.
B. S. Nilsen et al. [83]	1.452 GeV/A 1.212 GeV/A 1.001 GeV/A 0.504 GeV/A	Total and partial charge-changing cross sections measured for p-induced reaction on Kr and Ag targets.
N. T. Porile et al. [27]	300 GeV for proton beam 25.2 GeV for $^{12}\text{C}$ beam	Cross sections for the production of $\sim 100$ fragments for $40 \leq A \leq 106$ .
S. Shibata et al. [84]	12 GeV	The formation cross sections of $^9\text{Be}$ , $^{10}\text{Be}$ , $^{26}\text{Al}$ and $^{27}\text{Al}$ .
K. H. Tanaka et al. [20]	12 GeV	The energy spectra of IMFs: C, N, O, F, Ne, Na, Mg, Al, Si, P measured inclusively at several angles.
V. E. Viola et al. [85]		Fragment multiplicities and energy spectra for $Z < 20$ , at angles $18^\circ, 28^\circ, 42^\circ, 60^\circ, 78^\circ, 102^\circ, 119^\circ, 137^\circ$ and $156^\circ$ for $Z=1$ .
S. J. Yennello et al. [19]	0.9 GeV 3.6 GeV	Fragment energy spectra and angular distributions dependent on event multiplicity for fragments $3 \leq Z \leq 12$ .

## Appendix D

# Description of format of attached experimental data

The data collected during measurements of the PISA collaboration are attached to this thesis in electronic version on CD. It is necessary to write information about format of this data and its directory structure on CD.

### D.1. The structure of files and directories

The main directory contains 3 folders, named:

PISA  
INCL4.3+COAL  
OTHER

The most important is PISA directory. It contains PISA's data from reaction p+Ag at three different proton energies: 1.2 GeV, 1.9 GeV and 2.5 GeV. In subfolders one can find two different versions of data, binned by 1 MeV or 3 MeV. For purposes of this dissertation 3 MeV-binned data were used. Two subdirectories:

1MEV\_BIN  
3MEV\_BIN

contains identical structure of name folders (and files inside this three directories):

1200MEV  
1900MEV  
2500MEV.

The proton beam energies are put in directory names. Data for particular product of reactions are placed in separate files in this directories. For each proton energy and for each fragment emitted exists only one file. The structure of such files is common for every file in directories on CD, so it will be explained below in details (see D.2). The name of file contains element's symbol and its mass number. If mass number is not specified in the file name, the data were obtained without isotope identification. Files with mass number in their names contain data collected only for that isotope. Examples:

be.dat – contain data for Be element,  
be9.dat – contain data for specified isotope of Be:  ${}^9\text{Be}$ .

The directories INCL4.3+COAL contains results of INCL model calculation for different proton energies. This calculations are described in details in section 5.1. Format of files is identical like in previously discussed folder PISA. The directory

OTHER contains experimental data taken from literature:

190MEV – [14] - R. E. L. Green et al. Phys. Rev. C35 (1987) 1341  
 300MEV – [14] - R. E. L. Green et al. Phys. Rev. C35 (1987) 1341  
 480MEV – [13] - R. E. L. Green et al. Phys. Rev. C29 (1984) 1806

Format of this data files and directories structure is the same.

## D.2. File format

The begin of each file looks similar like in the following example:

```
7 number of angles in LAB. Ag+p->4He. Tp=2 GeV. PISA 2005 normalized
15.6 20.0 35.0 50.0 65.0 80.0 100.0 values of the angles (degrees)
85 theta= 15.6 deg
23.5 3.15008 0.0183726
26.5 2.29961 0.0159149
29.5 1.72714 0.0233613
32.5 1.41335 0.0331723
.
.
.
4 theta=20 deg
92.5 0.000646208 0.000172966
95.5 0.000369638 0.000130822
.
.
```

The first two lines contain some additional information, one can see for how many angles data were collected for this product, in this case: 7. There is also equation of the reaction and proton beam energy, in this example:  $\text{Ag}+\text{p}\rightarrow 4\text{He}$ .  $T_p=2.5$  GeV. Information on experiment which collected this data, or information about INCL model is also given. In second line values of angles are placed and after this line experimental data are listed. Data for each angle starts with line containing number of data points for this angle and repeated value of angle. In our example one can see that for angle 15.6 deg there are 85 points of data. In fourth line data start for the first angle. It contains three columns. First column - value of energy in MeV, second - value of cross section in  $\text{mb}/(\text{MeV}\cdot\text{sr})$ , and the last one contains statistical error of cross section in the same units. After 85 lines one can see introduction line for next angle, in the above example: 4 theta=20 deg. This is repeated for all angles in the file.

## Appendix E

# Experimental data

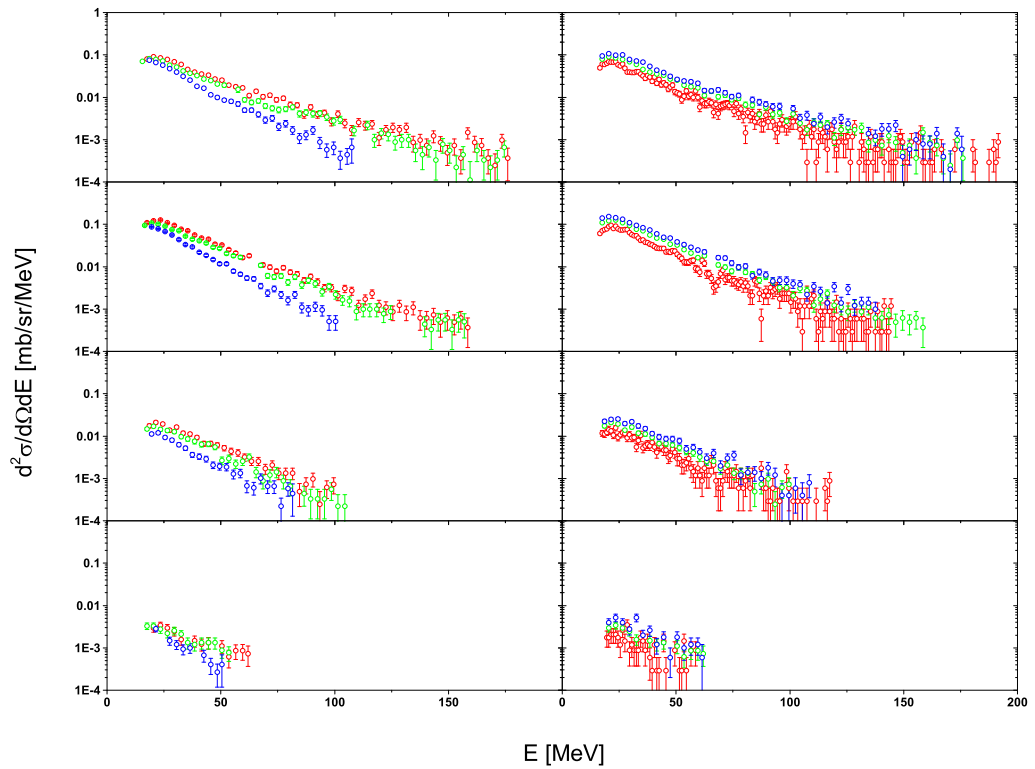


Figure E.1. Figure presents experimental data collected for  ${}^6\text{Li}$  on the upper panels, and  ${}^7\text{Li}$ ,  ${}^8\text{Li}$  and  ${}^9\text{Li}$ , on the other panels respectively. On the left fourth panels the angular dependence is shown for proton beam energy 1900 MeV. Red dots represents data collected for angle  $35^\circ$ , green one for  $50^\circ$  and blue one for  $100^\circ$ . The right panels show the energy dependence of measured data at angle  $35^\circ$  for three PISA's energies. Red points depict data collected for proton beam energy 1200 MeV, green one for 1900 MeV and blue one for 2500 MeV.

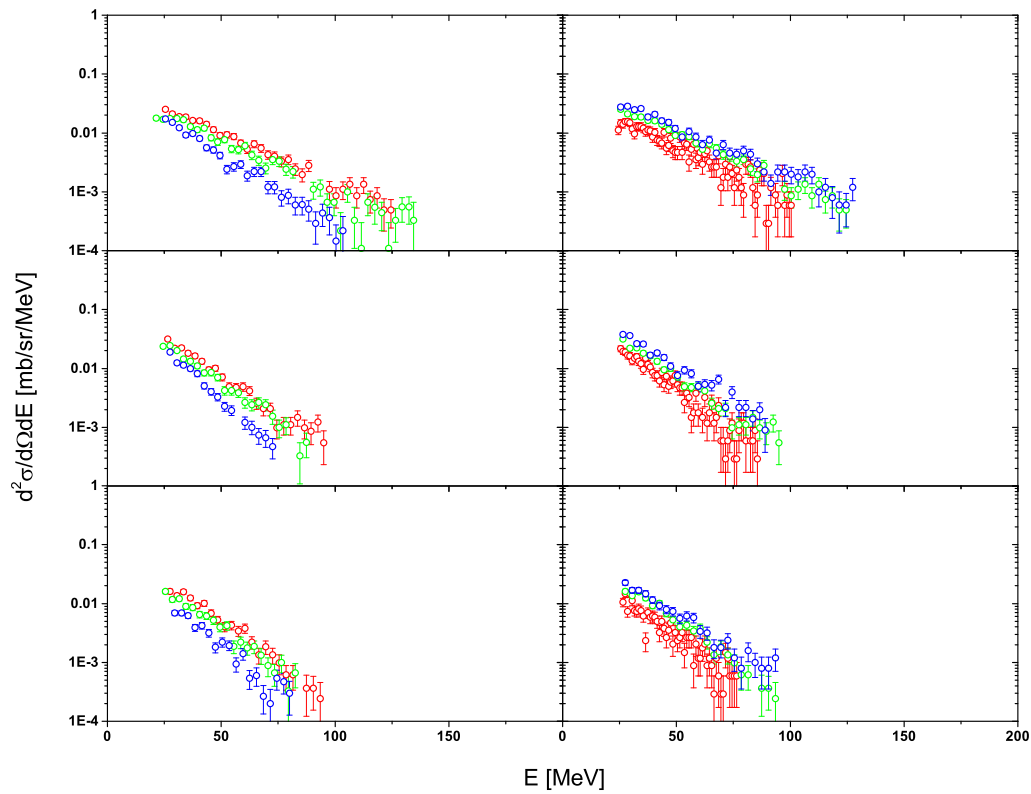


Figure E.2. Upper panels of the figure display data collected for  ${}^7\text{Be}$  whereas the data for  ${}^9\text{Be}$  and  ${}^{10}\text{Be}$  are shown in the middle and bottom panels, respectively. In the left three panels the angular dependence is shown for proton beam energy 1900 MeV. Red dots represent data collected for angle  $35^\circ$ , green one for  $50^\circ$  and blue one for  $100^\circ$ . The right three panels show the energy dependence of measured data at angle  $35^\circ$  for three energies. Red points depict data collected for proton beam energy 1200 MeV, green one for 1900 MeV and blue one for 2500 MeV.

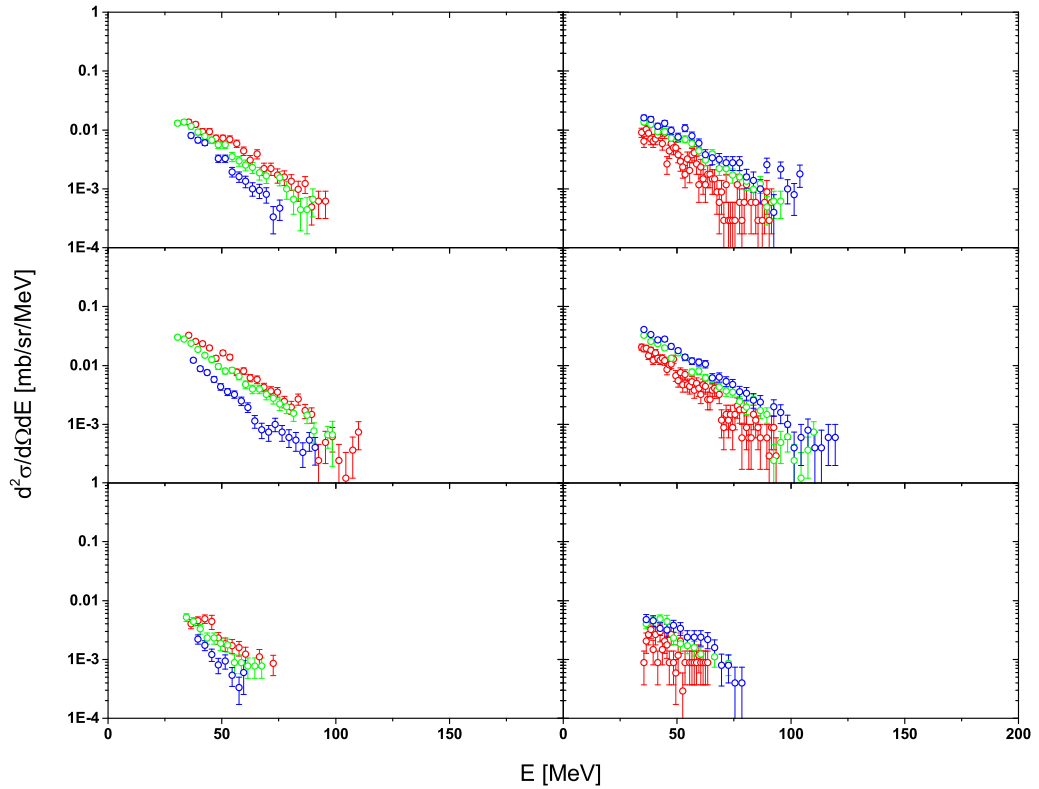


Figure E.3. Figure presents experimental data collected for  $^{10}\text{B}$ ,  $^{11}\text{B}$ , and  $^{12}\text{B}$  in the upper, middle and bottom panels, respectively. On the left three panels the angular dependence is shown for proton beam energy 1900 MeV. Red dots represent data collected for angle  $35^\circ$ , green one for  $50^\circ$  and blue one for  $100^\circ$ . The right three panels show the energy dependence of measured data at angle  $35^\circ$  for three proton beam energies. Red points depict data collected for proton beam energy 1200 MeV, green one for 1900 MeV and blue one for 2500 MeV.

Several general facts can be expressed after studying figures E.4-E.6. The most characteristic properties of the data are well visible.

*The angular dependence of the spectra.* Data registered at the small angles contain more abundant high energy tails (eg.: fig. E.4). This behavior is observed for all three energies. Additionally the high energy tails for light charged particles (fig.E.5) extend to higher energies than for intermediate mass fragments.

*The energy dependence of the spectra.* Data collected at three beam energy have almost exactly the same shape, but the cross section slightly increase with beam energy. It can be clearly seen on double differential spectra (fig. E.6).

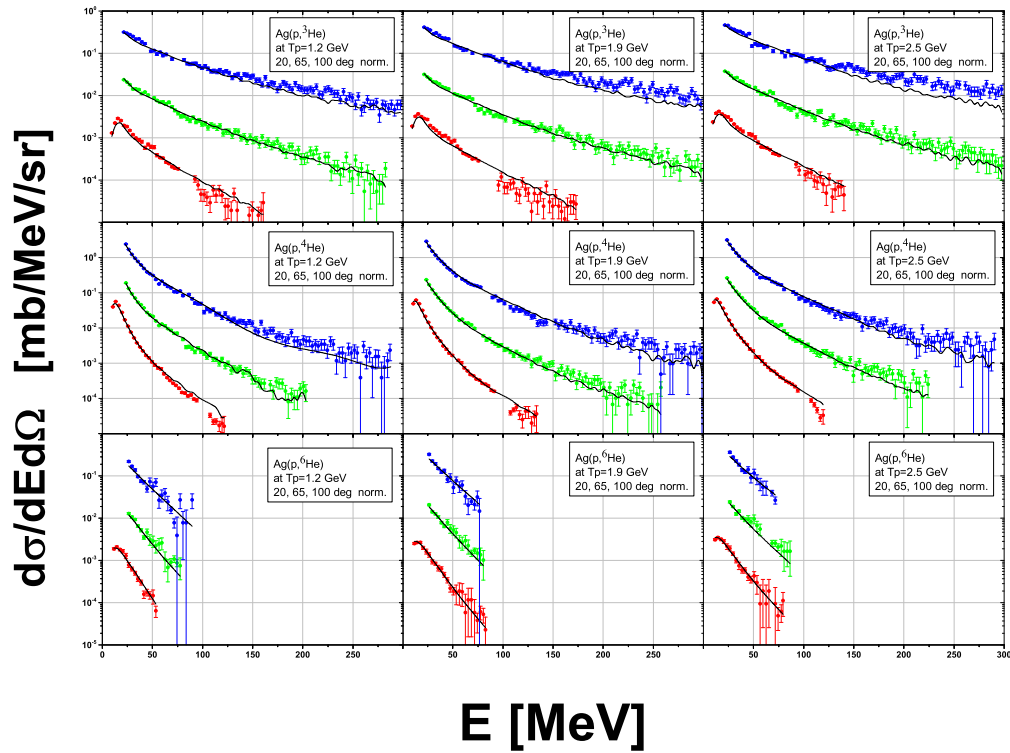


Figure E.4. This figure contains data of measured double differential cross sections of helium isotopes collected for 1200, 1900 and 2500 MeV beam energy at three angles. Data for  $65^\circ$ , green dots, were divided by factor 10, while data for  $100^\circ$ , red dots, were divided by factor 100. Data for  $20^\circ$ , blue dots, are shown without any scaling factor. Solid lines come from phenomenological analysis by two moving sources model.

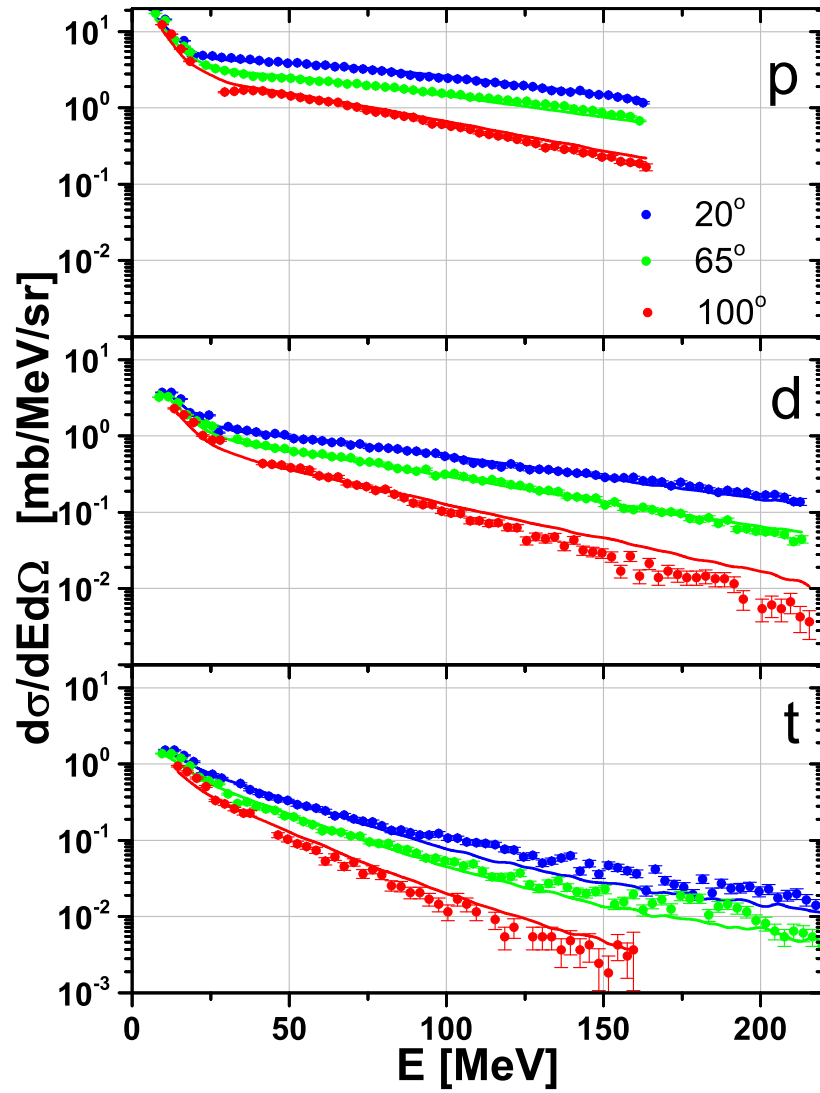


Figure E.5. Figure presents LCP measured at beam energy 1900 MeV for three chosen scattering angles. Red points represent data collected at  $100^\circ$ , green at  $60^\circ$  and blue ones at  $20^\circ$ . Solid lines come from phenomenological analysis with two moving sources.

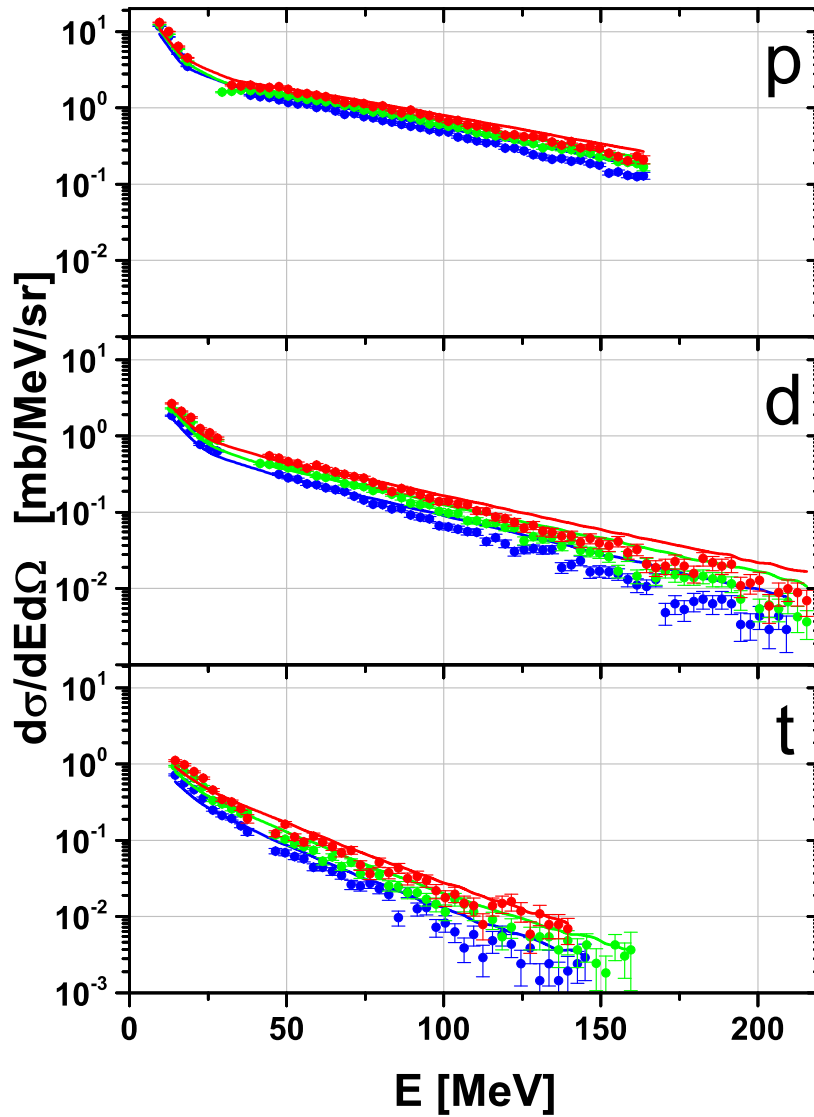


Figure E.6. Figure presents LCP measured at angle  $100^\circ$  for three energies. Red points represent data collected for beam energy 2500 MeV, green ones for 1900 MeV and blue ones for 1200 MeV. Solid lines come from phenomenological analysis with two moving sources.

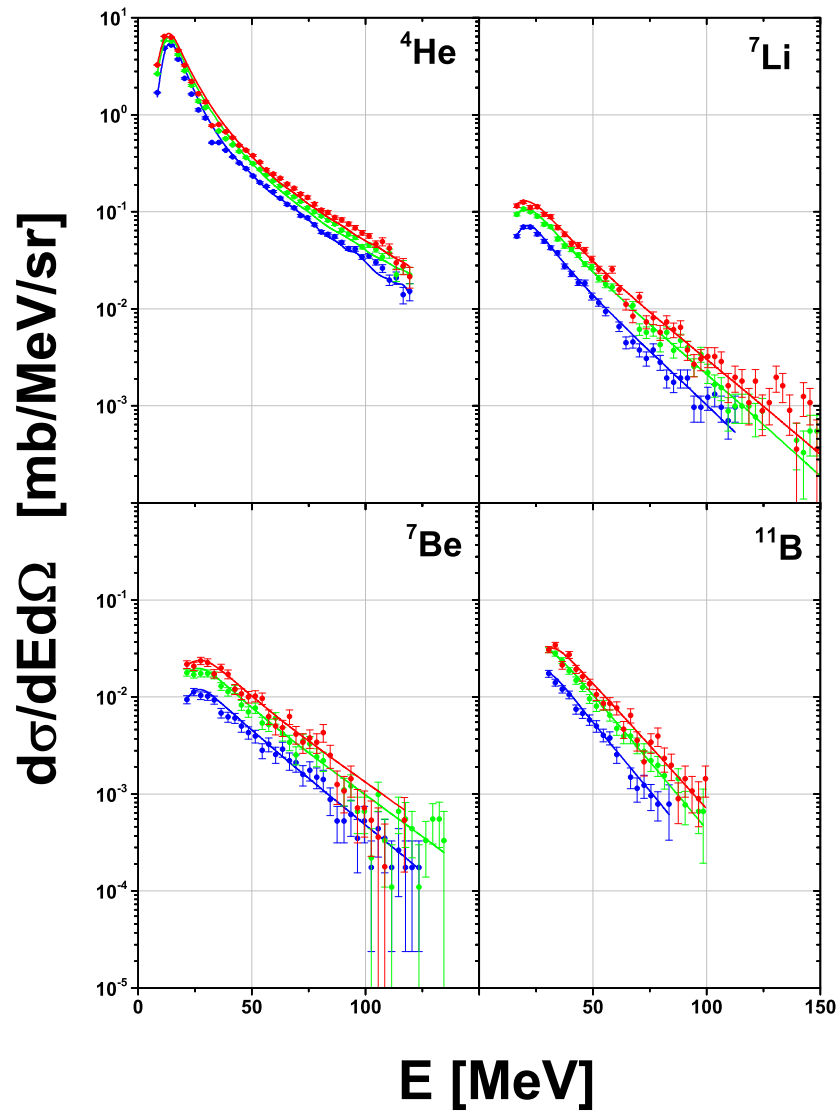


Figure E.7. Figure presents comparison of intermediate mass fragments spectra measured at  $50^\circ$  scattering angle for three different energies: 2500 MeV - red dots, 1900 MeV - green dots and 1200 MeV - blue ones. Solid lines come from phenomenological analysis with two moving sources.



# Bibliography

- [1] N. Prantzos, Li, Be, B and cosmic rays in the galaxy, in: IAP seminars, Institut d'Astrophysique de Paris, 2005.
- [2] G. T. Seaborg, Interaction of fast neutrons with lead, Ph.D. thesis, University of California, Berkeley (1937).
- [3] A. Letourneau, A. Bohm, J. Galin, B. Lott, A. Peghaire, M. Enke, C.-M. Herbach, D. Hilscher, U. Jahnke, V. Tishchenko, D. Filges, F. Goldenbaum, R. Neef, K. Nunighoff, N. Paul, G. Sterzenbach, L. Pienkowski, J. Toke, U. Schroder, Nucl. Phys. A712 (2002) 133.
- [4] E. K. Hyde, G. W. Butler, A. M. Poskanzer, Phys. Rev. C4 (1971) 1759.
- [5] A. Boudard, J. Cugnon, S. Leray, C. Volant, Nucl. Phys. A740 (2004) 195.
- [6] A. Boudard, J. Cugnon, J. C. David, S. Leray, D. Mancusi, Phys. Rev. C 87 (2013) 014606.
- [7] S. K. Sharma, Validation of spallation models, Ph.D. thesis, Jagiellonian University (2015).
- [8] A. Budzanowski, M. Fidelus, D. Filges, F. Goldenbaum, H. Hodde, L. Jarczyk, B. Kamys, M. Kistryn, S. Kistryn, S. Kliczewski, A. Kowalczyk, E. Kozik, P. Kulesza, H. Machner, A. Magiera, B. Piskor-Ignatowicz, K. Pysz, Z. Rudy, R. Siudak, M. Wojciechowski, Phys. Rev. C82 (2010) 034605.
- [9] A. M. Poskanzer, R. G. Sextro, A. M. Zebelman, H. H. Gutbrod, A. Sandoval, R. Stock, Phys. Rev. Lett. 35 (1975) 1701.
- [10] R. E. L. Green, R. G. Korteling, Phys. Rev. C18 (1978) 331.
- [11] R. E. L. Green, R. G. Korteling, Phys. Rev. C22 (1980) 1594.
- [12] R. E. L. Green, K. P. Jackson, R. G. Korteling, Phys. Rev. C25 (1982) 828.
- [13] R. E. L. Green, R. G. Korteling, Phys. Rev. C29 (1984) 1806.
- [14] R. E. L. Green, R. G. Korteling, J. M. D'Auria, K. P. Jackson, R. L. Helmer, Phys. Rev. C35 (1987) 1341.
- [15] A. Abduzhamilov, L. M. Barbier, L. P. Chernova, M. M. Chernyavsky, S. I. Gadzhieva, K. G. Gulamov, R. Holynski, W. V. Jones, N. Litvinenko, N. S. Lukicheva, D. Mirkhodzhaeva, V. S. Navotny, G. I. Orlova, N. W. Petrov, E. A. Ravina, N. S. Saidkhanov, N. A. Salmanova, L. N. Svechnikova, M. I. Tretyakova, J. P. Wefel, W. Wolter, B. Wosiek, K. Wozniak, Phys. Rev. D 39 (1989) 86.
- [16] R. G. Korteling, R. E. L. Green, J. M. D'Auria, R. L. Helmer, K. P. Jackson, S. B. Kaufman, B. D. Wilkins, Phys. Rev. C41 (1990) 2571.
- [17] S. J. Yennello, K. Kwiatkowski, S. Rose, L. W. Woo, S. H. Zhou, V. E. Viola, Phys. Rev. C41 (1990) 79.
- [18] S. J. Yennello, K. Kwiatkowski, D. E. Fields, R. Planeta, V. E. Viola, E. C. Pollacco, C. Volant, R. Dayras, R. Legrain, Y. Cassagnou, S. Harar, E. Hourani, Phys. Lett. B246 (1990) 26.
- [19] S. J. Yennello, E. C. Pollacco, K. Kwiatkowski, C. Volant, R. Dayras, Y. Cassagnou, R. Legrain, E. Norbeck, V. E. Viola, J. L. Wile, N. R. Yoder, Phys. Rev. Lett. 67 (1991) 671.

- [20] K. H. Tanaka, Y. Yamanoi, H. Ochiishi, H. Akiyoshi, S. Kouda, H. Nakamura, S. Morinobu, Y. Tanaka, K. Kimura, T. Shibata, Y. Sugaya, K. Yasuda, H. Ito, T. Murakami, Nucl. Phys. A583 (1995) 581C.
- [21] H. Ochiishi, H. Ito, K. Kimura, S. Kouda, T. Murakami, M. Shimooka, Y. Sugaya, K. H. Tanaka, S. Toyama, Y. Yamanoi, K. Yamamoto, K. Yasuda, Nucl. Instrum. Meth. A369 (1996) 269.
- [22] X. Ledoux, H. G. Bohlen, J. Cugnon, H. Fuchs, J. Galin, B. Gatty, B. Gebauer, D. Guerreau, D. Hilscher, D. Jacquet, U. Jahnke, M. Josset, S. Leray, B. Lott, B. M. Q. M. Morjean, G. Roschert, H. Rossner, A. P. (GANIL), L. Pienkowski, R. H. Siemssen, C. Stephan, Phys. Rev. C57 (1998) 2375.
- [23] J. Murata, Nucl. Phys. A654 (1999) 807c.
- [24] T. Murakami, K. H. Tanaka, Nucl. Phys. A734 (2004) E96.
- [25] R. Michel, R. Bodemann, H. Busemann, R. Daunke, M. Gloris, H. J. Lange, B. Klug, A. Krins, I. Leya, M. Lupke, S. Neumann, H. Reinhardt, M. Schnatz-Buttgen, U. Herpers, T. Schiekkel, F. Sudbrock, B. Holmqvist, H. Conde, P. Malmberg, M. Suter, B. Dittrich-Hannen, P. W. Kubik, H. A. Synal, D. Filges, Nucl. Instr. and Meth. in Phys. Res. B129 (1997) 153.
- [26] J. Benecke, T. T. Chou, C.-N. Yang, E. Yen, Phys. Rev. 188 (1969) 2159.
- [27] N. T. Porile, G. D. Cole, C. R. Rudy, Phys. Rev. C19 (1979) 2288.
- [28] R. G. Korteling, C. R. Toren, E. K. Hyde, Phys. Rev. C7 (1973) 1611.
- [29] A. Bubak, B. Kamys, M. Kistryn, B. Piskor-Ignatowicz, Nucl. Instr. and Meth. in Phys. Res. B226 (2004) 507.
- [30] N. T. Porile, A. J. Bujak, D. D. Carmony, Y. H. Chung, L. J. Gutay, A. S. Hirsch, M. Mahi, G. L. Paderewski, T. C. Sangster, R. P. Scharenberg, B. C. Stringfellow, Phys. Rev. C39 (1989) 1914.
- [31] M. E. Fisher, Physics 3 (1967) 255.
- [32] C. M. Herbach, D. Hilscher, U. Jahnke, V. G. Tishchenko, J. Galin, A. Letourneau, A. Peghaire, D. Filges, F. Goldenbaum, L. Pienkowski, W. U. Schroder, J. Toke, Nucl. Phys. A765 (2006) 426.
- [33] A. Bujak, J. E. Finn, L. J. Gutay, A. S. Hirsch, R. W. Minich, G. Paderewski, N. T. Porile, R. P. Scharenberg, B. C. Stringfellow, F. Turkot, Phys. Rev. C32 (1985) 620.
- [34] G. English, N. T. Porile, E. P. Steinberg, Phys. Rev. C10 (1974) 2268.
- [35] J. Hudi, T. Kirsten, R. W. Stoenner, O. A. Schaeffer, Phys. Rev. C1 (1970) 2019.
- [36] A. S. Hirsch, A. Bujak, J. E. Finn, L. J. Gutay, R. W. Minich, N. T. Porile, R. P. Scharenberg, B. C. Stringfellow, F. Turkot, Phys. Rev. C29 (1984) 508–525.
- [37] L. N. Andronenko, A. A. Kotov, L. A. Vaishnena, W. Neubert, H. W. Barz, J. Bondorf, R. Donangelo, H. Schulz, Phys. Lett. B174 (1986) 18.
- [38] G. D. Westfall, R. G. Sextro, A. M. Poskanzer, A. M. Zebelman, G. W. Butler, E. K. Hyde, Phys. Rev. C17 (1978) 1368.
- [39] S. Katcoff, H. R. Fickel, A. Wyttenbach, Phys. Rev. 166 (1968) 1147.
- [40] G. English, Y. W. Yu, N. T. Porile, Phys. Rev. C10 (1974) 2281.
- [41] A. D. Panagiotou, M. W. Curtin, H. Toki, D. K. Scott, P. J. Siemens, Phys. Rev. Lett. 52 (1984) 496.
- [42] A. A. Kotov, L. N. Andronenko, M. N. Andronenko, Y. I. Gusev, K. V. Lukashin, D. M. Seliverstov, I. I. Strakovsky, L. A. Vaishnena, W. Neubert, Nucl. Phys. A583 (1995) 575C.
- [43] N. T. Porile, A. T. Bujak, D. D. Carmony, Y. H. Chung, L. J. Gutay, A. S. Hirsch, M. Mahi, G. L. Paderewski, T. C. Sangster, R. P. Scharenberg, B. C. Stringfellow, Nucl. Phys. A471 (1987) 149.
- [44] W. Eyrich, Eur. Phys. J. A 31 (2007) 435.
- [45] A. Lehrach, U. Bechstedt, J. Dietrich, R. Eichhorn, R. Gebel, B. Lorentz, R. Maier,

- D. Prasuhn, H. Schneider, R. Stassen, H. Stockhorst, R. Tölle, A. Schnase, Proceedings of EPAC 2004 .
- [46] B. Piskor-Ignatowicz, Energy dependence of proton induced fragmentation of atomic nuclei, Ph.D. thesis, Jagiellonian University (2009).
- [47] A. S. Fomichev, I. David, S. M. Lukyanov, Y. E. Penionzhkevich, N. K. Skobelev, O. B. Tarasov, A. Matthies, H. G. Ortlepp, M. Lewitowicz, M. G. Saint-Laurent, J. M. Corre, Z. Dlouhy, I. Pecina, C. Borcea, Nucl. Instr. and Meth. in Phys. Res. A344 (1994) 378.
- [48] M. Fidelus, D. Filges, F. Goldenbaum, H. Hodde, A. Jany, L. Jarczyk, B. Kamys, M. Kistryn, S. Kistryn, S. Kliczewski, E. Kozik, P. Kulesa, H. Machner, A. Magiera, B. Piskor-Ignatowicz, K. Pysz, Z. Rudy, S. K. Sharma, R. Siudak, M. Wojciechowski, Phys. Rev. C89 (2014) 054617.
- [49] P. Napolitani, K. H. Schmidt, L. Tassan-Got, P. Armbruster, T. Enqvist, A. Heinz, V. Henzl, D. Henzlova, A. Kelic, R. Pleskac, M. V. Ricciardi, C. Schmitt, O. Jordanov, L. Audouin, M. Bernas, A. Lafriakh, F. Rejmund, C. Stephan, J. Benlliure, E. Casarejos, M. F. Ordonez, J. Pereira, A. Boudard, B. Fernandez, S. Leray, C. Villagrasa, C. Volant, Phys. Rev. C76 (2007) 064609.
- [50] R. Serber, Phys. Rev. 72 (1947) 1114.
- [51] J. Cugnon, T. Mizutani, J. Vandermeulen, Nucl. Phys. A 352 (1981) 505.
- [52] J. Cugnon, Nucl. Phys. A 462 (1987) 751.
- [53] A. Boudard, J. Cugnon, S. Leray, C. Volant, Phys. Rev. C66 (2002) 044615.
- [54] S. Furihata, Nucl. Instr. and Meth. in Phys. Res. B. 171 (2000) 251.
- [55] S. Furihata, T. Nakamura, J. of Nucl. Scien. and Tech. Supplement 2 (2002) 758.
- [56] J. P. Bondorf, R. Donangelo, I. N. Mishustin, C. J. Pethick, H. Schultz, K. Sneppen, Nucl. Phys. A443 (1985) 321.
- [57] J. P. Bondorf, R. Donangelo, I. N. Mishustin, H. Schultz, Nucl. Phys. A444 (1985) 460.
- [58] A. S. Botvina, A. S. Iljinov, I. N. Mishustin, Nucl. Phys. A507 (1990) 649.
- [59] V. F. Weisskopf, Phys. Rev. 53 (1937) 295.
- [60] V. F. Weisskopf, D. H. Ewing, Phys. Rev. 57 (1940) 473.
- [61] I. Dostrovsky, Z. Fraenkel, G. Friedlander, Phys. Rev. 116 (1959) 683.
- [62] A. Gilbert, A. G. W. Cameron, Can. J. Phys. 43 (1965) 1446.
- [63] A. S. Botvina, I. N. Mishustin, 1st Workshop on Accelerator Radiation Induced Activation, Paul Scherrer Institut, Switzerland 1.
- [64] E. Fermi, Prog. of Theor. Phys. 5 (1950) 570.
- [65] A. Budzanowski, M. Fidelus, D. Filges, F. Goldenbaum, H. Hodde, L. Jarczyk, B. Kamys, M. Kistryn, S. Kistryn, S. Kliczewski, A. Kowalczyk, E. Kozik, P. Kulesa, H. Machner, A. Magiera, B. Piskor-Ignatowicz, K. Pysz, Z. Rudy, R. Siudak, M. Wojciechowski, Phys. Rev. C80 (2009) 054604.
- [66] A. Budzanowski, M. Fidelus, D. Filges, F. Goldenbaum, H. Hodde, L. Jarczyk, B. Kamys, M. Kistryn, S. Kistryn, S. Kliczewski, A. Kowalczyk, E. Kozik, P. Kulesa, H. Machner, A. Magiera, B. Piskor-Ignatowicz, K. Pysz, Z. Rudy, R. Siudak, , M. Wojciechowski, Phys. Rev. C78 (2008) 024603.
- [67] M. Fidelus, Model description of proton induced fragmentation of atomic nuclei, Ph.D. thesis, Jagiellonian University (2010).
- [68] A. Kowalczyk, Validation of spallation models, Private information.
- [69] R. Minich, S. Agarwal, A. Bujak, J. Chuang, J. Finn, L. Gutay, A. Hirsch, N. Porile, R. Scharenberg, B. Stringfellow, Phys. Lett. B118 (1982) 458.
- [70] J. Richert, P. Wagner, Phys. Rep. 350 (2001) 1.
- [71] J. E. Finn, S. Agarwal, A. Bujak, J. Chuang, L. J. Gutay, A. S. Hirsch, R. W. Minich, N. T. Porile, R. P. Scharenberg, B. C. Stringfellow, F. Turkot, Phys. Rev. Lett. 49

- (1982) 1321.
- [72] T. A. Shibata, K. Nakai, H. En'yo, S. Sasaki, M. Sekimoto, I. Arai, K. Nakayama, K. Ichimaru, H. Nakamura-Yokota, R. Chiba, Nucl. Phys. A408 (1983) 525.
- [73] H. En'yo, S. Sasaki, T. Nagae, K. Tokushuku, M. Sano, M. Sekimoto, J. Chiba, K. Ichimaru, T. Mori, T. Katsumi, H. Yokota, R. Chiba, K. Nakai, Phys. Lett. 159B (1985) 1.
- [74] E. W. Baker, S. Katcoff, C. P. Baker, Phys. Rev. 117 (1960) 1352.
- [75] G. D. Cole, N. T. Porile, Phys. Rev. C25 (1982) 244.
- [76] J. B. Cumming, S. Katcoff, N. T. Porile, S. Tanaka, A. Wyttenbach, Phys. Rev. 134 (1964) B1262.
- [77] J. Hudis, S. Katcoff, Phys. Rev. C13 (1976) 1961.
- [78] J. Hudis, Phys. Rev. 171 (1968) 1301.
- [79] S. Katcoff, Phys. Rev. 114 (1959) 905.
- [80] S. Katcoff, E. W. Baker, N. T. Porile, Phys. Rev. 140 (1965) B1549.
- [81] M. Lagarde-Simonoff, G. N. Simonoff, Phys. Rev. C20 (1979) 1498.
- [82] M. Lefort, J. P. Cohen, H. Dubost, X. Tarrago, Phys. Rev. 139 (1965) B1500.
- [83] B. S. Nilsen, C. J. Waddington, J. Klarmann, J. R. Cummings, T. L. Garrard, Phys. Rev. C52 (1995) 3277.
- [84] S. Shibata, M. Imamura, K. Kobayashi, H. Nagai, K. Sakamoto, M. Furukawa, I. Fujiwara, Phys. Rev. C48 (1993) 2617.
- [85] V. E. Viola, K. Kwiatkowski, L. Beaulieu, D. S. Bracken, H. Breuer, J. Brzychczyk, R. T. de Souza, D. S. Ginger, W. C. Hsi, R. G. Korteling, T. Lefort, W. G. Lynch, K. B. Morley, R. Legrain, L. Pienkowski, E. C. Pollacco, E. Renshaw, A. Ruangma, M. B. Tsang, C. Volant, G. Wang, S. J. Yennello, N. R. Yoder, Phys. Rep. 434 (2006) 1.